

UC Santa Cruz

UC Santa Cruz Electronic Theses and Dissertations

Title

The Coupling of Climate and Carbon Cycle during the Late Paleocene and Early Eocene on Long and Short Timescales

Permalink

<https://escholarship.org/uc/item/6c21k9jd>

Author

Harper, Dustin T

Publication Date

2018

Copyright Information

This work is made available under the terms of a Creative Commons Attribution License, available at <https://creativecommons.org/licenses/by/4.0/>

Peer reviewed|Thesis/dissertation

UNIVERSITY OF CALIFORNIA
SANTA CRUZ

**THE COUPLING OF CLIMATE AND CARBON CYCLE DURING THE
LATE PALEOCENE AND EARLY EOCENE ON LONG AND SHORT
TIMESCALES**

A dissertation submitted in partial satisfaction
of the requirements for the degree of

DOCTOR OF PHILOSOPHY

in

EARTH SCIENCES

by

Dustin T. Harper

December 2018

The Dissertation of Dustin T. Harper is
approved:

Professor James C. Zachos, chair

Professor Matthew E. Clapham

Professor Paul L. Koch

Professor A. Christina Ravelo

Lori Kletzer
Vice Provost and Dean of Graduate Studies

Copyright © by
Dustin T. Harper
2018

Table of Contents

List of Figures	v
Abstract	vii
Acknowledgments	ix
Dedication	xi
1. Introduction	1
2. Subtropical Sea Surface Warming and Increased Salinity During Eocene Thermal Maximum 2	9
2.1. Introduction	9
2.2. Methods	12
2.3. Results	18
2.4. Discussion	18
2.5. Conclusions	24
3. Surface Ocean Acidification During Eocene Thermal Maximum 2: Implications for Carbon Release	25
3.1. Introduction	25
3.2. Methods	29
3.3. Results	35
3.4. Discussion	41
3.5. Conclusions	53
4. Long-term Trends and Orbital Variability in Climate, the Carbon Cycle and Marine Chemistry During the Late Paleocene and Early Eocene	55

4.1. Introduction	55
4.2. Methods	61
4.3. Results	65
4.4. Discussion	66
4.5. Conclusions	83
5. Concluding remarks	85
6. References	87

List of Figures

Figure 2.1. Stable carbon isotope compilation for H1 (ETM-2) and H2 events	11
Figure 2.2. LOSCAR ETM-2 simulation output	14
Figure 2.3. Compiled ETM-2 geochemical data from Sites 1209 and 1265	17
Figure 2.4. SST and SSS ETM-2 anomalies for the Pacific and Atlantic	19
Figure 2.5. pH sensitivity tests for SST and SSS anomalies	21
Figure 2.6. Recalculated SST and SSS PETM anomalies for the Pacific	23
Figure 3.1. Site map with 54 Ma tectonic configuration	28
Figure 3.2. SEM of ETM-2 <i>Acarinina soldadoensis</i> from Site 1210	30
Figure 3.3. SEM of ETM-2 <i>Acarinina soldadoensis</i> from Site 1265	31
Figure 3.4. Stable carbon isotope data for EMT-2 in LPEE context	37
Figure 3.5. Foraminiferal geochemical data for the PETM including pH, SST, and DIC calculations	43
Figure 3.6. Foraminiferal geochemical data for ETM-2 including pH, SST, and DIC calculations	45
Figure 3.7. LOSCAR ETM-2 large carbon release simulation output	48
Figure 3.8. Data-model comparison for ETM-2	50
Figure 4.1. LPEE stable carbon isotope compilation	56
Figure 4.2. Stable oxygen isotope data (bulk and benthic) during the LPEE	58
Figure 4.3. Stable oxygen isotope data (planktic) during the LPEE	66
Figure 4.4. Planktic Mg/Ca during the LPEE	67

Figure 4.5. Planktic B/Ca and $\delta^{11}\text{B}$ during the LPEE	69
Figure 4.6. Benthic B/Ca during the LPEE	72
Figure 4.7. Reconstructed Pacific sea surface pH during the LPEE	75
Figure 4.8. Planktic Mg/Ca-based SST anomalies during the LPEE	76
Figure 4.9. Planktic Mg/Ca _{sw} anomalies during the LPEE	78
Figure 4.10. Simulated LPEE pH output of Komar et al., 2013	82

Abstract

The Coupling of Climate and Carbon Cycle during the Late Paleocene and Early Eocene on Long and Short Timescales

Dustin T. Harper

The late Paleocene and early Eocene (LPEE; ca. 59 to 52 Ma) was an interval of warming superposed on the abrupt carbon release events (or hyperthermals) of the early Eocene. The LPEE provides an opportunity to test the coupling of carbon release (and associated long- and short-term warming), to other climate-carbon cycle feedbacks (e.g., ocean acidification and shifts in the hydrologic cycle). Much work has focused on determining the sensitivities of sea surface pH, climate and the hydrologic cycle to carbon release during the largest hyperthermal of the Cenozoic, the Paleocene-Eocene Thermal Maximum (PETM; ca. 56 Ma). However, Eocene Thermal Maximum 2 (ETM-2; ca. 54 Ma) provides a secondary calibration point on assessing the sensitivity of carbon cycle-climate feedbacks to carbon release. Additionally, it has been hypothesized that the long-term carbon storage and release mechanisms (e.g., marine clathrates and organic carbon) are linked to the hyperthermal events, however, constraints on long-term changes in carbonate chemistry are lacking for the interval.

This thesis aims to characterize the nature of changes in the climate and carbon cycle associated with the onset of the LPEE warming, and subsequent

cyclicality up to ETM-2 with the overarching goal of testing hypotheses for the origin of both the LPEE and ETM-2. To this end, a multiproxy approach utilizing boron-based ($\delta^{11}\text{B}$ and B/Ca) and paleothermometry proxies (Mg/Ca and $\delta^{18}\text{O}$) is applied to determine the magnitude of shifts in climate, marine carbonate chemistry, and, on shorter timescales, the hydrologic cycle using materials collected from ODP Sites 1209, 1210, 1262 and 1265 (Legs 198 and 208; subtropical Pacific and Atlantic, respectively). Further, I present the first LOSCAR carbon cycle/climate numerical simulations to model the release of carbon to the atmosphere during ETM-2, constrained by the CCD, $\delta^{13}\text{C}$, and proxy-based observations of changes in temperature and pH. Additionally, changes in long-term Pacific sea surface pH are used to assess the validity of previously published carbon cycle simulations of the LPEE.

Acknowledgments

I would first like to thank my advisor, James Zachos, for guiding me in the right direction when I struggled, providing collaborative discussions, and introducing me to the Paleoclimatology and Paleoceanography community. Thank you also to my dissertation committee, Matthew Clapham, Paul Koch and Christina Ravelo for constructive feedback throughout the research process. This thesis was a collaborative effort and I am grateful for the hard work and feedback of my coauthors and collaborators. I am especially indebted to Bärbel Hönisch, who helped me with stable boron isotope measurements and interpretations, and Richard Zeebe, who provided carbon cycle simulations and lively discussions. I would also like to thank all of my other co-authors and collaborators on these projects: Laura Haynes, Sandy Kirtland-Turner, Luc Lourens, Ursula Röhl, Cindy Schrader, Ellen Thomas, and Thomas Westerhold. Additionally, this work would not have been possible without the samples and funding provided by IODP and the National Science Foundation.

Thank you to all my fellow IODP Expedition 371 shipboard scientists and crew for their guidance and friendship, especially Thomas Westerhold and the co-chiefs Jerry Dickens and Rupert Sutherland who trusted me enough to bring me aboard, despite my inexperience. I could not have generated the data for this thesis without the patience and help of Rob Franks in the Marine Analytical Lab, and Dyke Andreasen and Colin Carney in the Stable Isotope Lab. Additionally, I appreciate the help of Brandon Cheney and Myriam Telus in the SEM lab. Thank you to Oliver Azevedo, Tali Babila, Eddie Ballaron, Kyle Broach, Reid Clark, Cheyne Hirota, Don

Penman, Will Rush, Wayne Strojic, Sarah White, Demir Worthington, Fei Wu and all of my Earth and Planetary Sciences cohort for invaluable help and discussions regarding research, analytical chemistry, graduate school and life.

Last, thank you to my family and friends for all of their continuing love and support, especially Elizabeth for her patience and encouragement.

This thesis is dedicated to my dog, Dasha, for helping preserve my sanity by encouraging daily walks through the redwoods.

1. Introduction

1.1. Late Paleocene early Eocene climate and carbon cycle

The late Paleocene and early Eocene (LPEE; ca. 58 to 52 Ma) was a dynamic warming interval during the early Cenozoic, when Earth was largely ice-free (e.g., Zachos et al., 2008) and atmospheric CO₂ was likely higher than pre-industrial levels (e.g., Royer, 2014). Beginning at the Paleocene Carbon Isotope Maximum (PCIM) and culminating during the Early Eocene Climatic Optimum (Zachos et al., 2001), the long-term LPEE warming is superposed on eccentricity-paced (i.e., 400 kyr) orbital cyclicity in, and abrupt perturbations to (i.e., hyperthermals associated with the release of ¹³C-depleted carbon to the atmosphere), climate and the carbon cycle, as evidenced by stable oxygen and carbon isotopes (e.g., Littler et al., 2014; Lourens et al., 2005; Westerhold et al., 2011; Zachos et al., 2001). Two long-term warming mechanisms have been proposed: volcanic CO₂ emissions from North Atlantic Igneous Province (NAIP) volcanism (e.g., Storey et al., 2007) and/or a decrease in the net burial flux of organic carbon (e.g., Hilting et al., 2008; Kurtz et al., 2003). For the latter mechanism, it has been hypothesized that the long-term storage and release of carbon during the late Paleocene is linked to the abrupt release of carbon during the hyperthermal events (Dickens, 2003; Dickens, 2011; Hilting et al., 2008; Komar et al., 2013). Despite the significance of the LPEE in terms of carbon cycle and climate coupling over long and short timescales, records of ocean pH, and in turn, estimates

of atmospheric CO₂, which could be used to test numerical simulations, are lacking for key intervals.

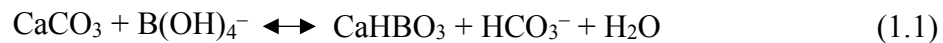
The hyperthermals of the early Eocene are varied in rate and magnitude of atmospheric carbon release and subsequent climatic response, each providing their own unique case study into the coupling of climate and the carbon cycle. These paleoclimate case studies can be assessed in terms of the magnitude and timing of temperature change, ocean acidification, and shifts in the hydrologic cycle, providing calibration points on the sensitivity of each feedback to carbon release. Much of the previous work on hyperthermal events has focused on the Paleocene-Eocene Thermal Maximum (PETM; ca. 56 Ma), and includes constraining the magnitude of warming (4 to 8 °C; Dunkley Jones et al., 2013), ocean acidification (~0.3 pH units; Babila et al., 2018; Gutjahr et al., 2017; Penman et al., 2014) and shifts in the hydrologic cycle (e.g., Schmitz and Pujalte, 2007; Zachos et al., 2003). Additional observational data from a less-extreme hyperthermal event, such as Eocene Thermal Maximum 2 (ETM-2; ca. 54.1 Ma), will allow for tests on the sensitivity of climate, marine carbonate chemistry, and the hydrologic cycle to more subdued carbon release.

There is uncertainty regarding the timing of carbon release for the PETM (Cui et al., 2011; Kirtland Turner and Ridgwell, 2016; McInerney and Wing, 2011; Röhl et al., 2007), in part due to the abrupt nature of carbon release and subsequent seafloor dissolution, which compromised many pelagic carbonate records of the onset of the event via chemical erosion (Zachos et al., 2005). ETM-2 pelagic carbonate records are largely complete due to smaller-scale seafloor dissolution (Lourens et al., 2005;

Stap et al., 2009) in response to a less massive release of carbon to the atmosphere (i.e., less extreme carbonate compensation depth (CCD) shoaling). Additionally, the onset is slower than that of the PETM (compare the ~6 kyr PETM onset of Kirtland Turner and Ridgwell (2016) with the ~25 kyr ETM-2 onset of Stap et al. (2009)). This slower onset provides higher depth resolution during the initial decline in carbon isotopes, which allows for more reliable age constraints (e.g., Stap et al., 2009). Thereby, ETM-2 provides an excellent opportunity to test the timing of carbon cycle-climate feedbacks (both negative and positive) using geochemical data and numerical simulations.

1.2. Boron-based foraminifera proxies

Driven by the need to reconstruct atmospheric CO₂, boron-based foraminiferal proxies ($\delta^{11}\text{B}$ and B/Ca) have been developed and used to constrain pH of the ocean in the past (Allen and Hönisch, 2012; Anagnostou et al., 2016; Foster, 2008; Penman et al., 2014). Boron speciates in seawater as boric acid, B(OH)₃, or borate ion, B(OH)₄⁻, and as pH increases, the concentration of aqueous borate ion increases. Additionally, $\delta^{11}\text{B}_{\text{borate}}$ is offset from $\delta^{11}\text{B}_{\text{boric acid}}$ by a constant -20‰, and as pH increases $\delta^{11}\text{B}_{\text{borate}}$ follows, due to the relative change in abundance, and equilibrium isotopic fractionation, of the two chemical species. Borate is thought to be primarily incorporated into carbonates following Hemming and Hansen (1992):



As mentioned above, the concentration of borate is related to pH, thus, the total boron concentration (relative to test calcium) is related to pH. Furthermore, the $\delta^{11}\text{B}$ of

foraminiferal calcite can be used to estimate past $\delta^{11}\text{B}_{\text{borate}}$ and, in turn, marine pH at the depth at which a particular species inhabits during test secretion (Allen and Hönisch, 2012; Allen et al., 2011; Hönisch and Hemming, 2004; Yu and Elderfield, 2007):

$$\text{pH} = \text{pK}_{\text{B}}^* - \log\left(-(\delta^{11}\text{B}_{\text{sw}} - \delta^{11}\text{B}_{\text{borate}}) / (\delta^{11}\text{B}_{\text{sw}} - \alpha(\delta^{11}\text{B}_{\text{borate}}) - \varepsilon)\right) \quad (1.2)$$

Estimates of isotopic fractionation of the two species of boron in seawater (α and ε), the boron isotopic composition of seawater ($\delta^{11}\text{B}_{\text{sw}}$), the stoichiometric equilibrium constant for boric acid (pK_{B}^* ; depends on pressure, temperature, and salinity), and the species specific relationship of $\delta^{11}\text{B}_{\text{foram}}$ versus $\delta^{11}\text{B}_{\text{borate}}$ (e.g., Hönisch et al., 2019) are all required in order to compute pH from $\delta^{11}\text{B}_{\text{foram}}$ using Equation (1.2). In this thesis, pH is calculated from $\delta^{11}\text{B}_{\text{foram}}$ following Hönisch et al. (2019) and using the chemical routines of Zeebe and Wolf-Gladrow (2001).

Following Yu and Elderfield (2007), boron incorporation into calcite is controlled by the partition coefficient (K_{D}), and the relative concentration of borate with respect to bicarbonate ion:

$$[\text{B}/\text{Ca}]_{\text{CaCO}_3} = K_{\text{D}} * [\text{B}(\text{OH})_4^- / \text{HCO}_3^-]_{\text{seawater}} \quad (1.3)$$

Since borate ion increases with increasing pH, bicarbonate decreases with increasing pH, and K_{D} is constant, the B/Ca ratio should also vary with pH. However, there is still some debate with regard to what carbonate system parameter B/Ca is recording (Allen and Hönisch, 2012; Babila et al., 2016; Henehan et al., 2015; Salmon et al., 2016). While the proxy should, in theory, vary with pH, studies have shown that the competition between the borate, bicarbonate and carbonate anions, which are all pH

sensitive, could lead to complications (e.g., Allen and Hönisch, 2012). In epifaunal benthic foraminifera, however, it appears that B/Ca is recording the deep-water carbonate saturation state (e.g., Yu and Elderfield, 2007; Yu et al., 2013). However, controls on B/Ca in planktic foraminifera have remained somewhat uncertain. Studies have attributed complications to seasonal light variability (Babila et al., 2014), precipitation and growth rate (e.g., Salmon et al., 2016), and phosphate concentration (Henehan et al., 2015). However, Haynes et al. (2017) address these complications and, using foraminifera culturing experiments, conclude that B/Ca in planktic foraminifera may be controlled by the concentration of marine dissolved inorganic carbon (DIC), consistent with the original proxy controls developed by Yu and Elderfield (2007) (i.e., DIC is primarily composed of marine HCO_3^- ; Equation (1.3)). However, only one modern species B/Ca versus DIC calibration, applied to Paleocene-like seawater conditions, has been generated. Therefore, once calibration sensitivities are better established, the proxy could provide useful insight into the marine carbonate system of past and it should be critically applied at the present time.

1.3. Mg/Ca and $\delta^{18}\text{O}$ in planktic foraminifera

Numerical modeling studies of the response of the hydrologic cycle to global warming suggest warming-induced drying of low- to mid-latitudes due to enhanced moisture transport poleward, which tends to increase precipitation at high-latitudes (Roberts et al., 2011; Tindall et al., 2010). This is consistent with climate theory, which indicates that greenhouse gas (GHG) induced warming enhances meridional vapor transport and thereby “intensifies” the hydrologic cycle (Carmichael et al.,

2015). It is possible to test this phenomenon by applying geochemical proxies to past warming events to constrain changes in ocean temperature and surface salinity, following Zachos et al. (2003).

Planktic foraminiferal $\delta^{18}\text{O}$ ($\delta^{18}\text{O}_{\text{planktic}}$) records temperature and the $\delta^{18}\text{O}$ of seawater, which is dependent on salinity and global ice volume. Therefore, if a second temperature proxy is applied (e.g., Mg/Ca in planktic foraminifera, or $\text{Mg}/\text{Ca}_{\text{planktic}}$), changes in past sea surface salinity (SSS) can be determined (i.e., by determining $\delta^{18}\text{O}$ of seawater) in tandem with changes in sea surface temperatures (SST). According to Kozdon et al. (2013), $\delta^{18}\text{O}_{\text{planktic}}$ may be compromised due to diagenetic alteration over longer length scales, however, over short intervals, such as hyperthermal events, temperature and salinity signals should be preserved in pelagic marine sediments (i.e., uniform diagenetic overprinting). Mg/Ca in foraminifera tends to be even less affected by alteration in pelagic marine sediments on long and short length scales (Kozdon et al., 2013).

$\text{Mg}/\text{Ca}_{\text{planktic}}$ has been widely applied to reconstruct surface ocean temperatures over long and short intervals in the Paleogene to determine past temperatures (e.g., Bohaty et al., 2012; Zachos et al., 2003) and estimate the Mg/Ca of seawater ($\text{Mg}/\text{Ca}_{\text{sw}}$) (e.g., Evans et al., 2018). On short timescales, it is possible to estimate the relative temperature change using foraminiferal Mg/Ca following the equation of Zachos et al. (2003):

$$\Delta T = (1/A) * \ln [(C/100)+1] \quad (1.4)$$

Where C is the percent change in Mg/Ca from a baseline value, and 'A' is the

exponential calibration constant, which is species specific. Most modern planktic species exhibit ‘A’ values of ~0.09 in culture calibration and core-top studies (Anand et al., 2003; Dekens et al., 2002). However, Evans et al. (2016) document a Mg/Ca_{sw} dependence in the ‘A’ constant in their culturing study. Therefore, I first calculate relative temperature changes (i.e., Chapter 2) using a large range in ‘A’ values following the likely range for early Eocene Mg/Ca_{sw} from Evans et al. (2016).

To determine absolute temperatures from Mg/Ca_{planktic} following Anand et al. (2003), more information (i.e., an additional constant, or ‘B’ value) is required:

$$\text{Mg/Ca} = B * \exp^{AT} \quad (1.5)$$

The pre-exponential constant (‘B’ value) is highly dependent on Mg/Ca_{sw} (e.g., Evans and Müller, 2012). However, recently published records of Mg/Ca_{sw} during the Eocene using a coupled Mg/Ca_{foram} and TEX₈₆ approach (i.e., Evans et al., 2018) have allowed for the estimation of absolute temperature using Mg/Ca_{planktic} during the early Eocene (i.e., Chapter 3). Additionally, Mg/Ca_{planktic} displays a linear pH dependence (Evans et al., 2016):

$$\text{Mg/Ca} = -0.70 * \text{pH} + 6.7 \quad (1.6)$$

Therefore, the Mg/Ca_{planktic} value should be pH-adjusted (using either model or proxy-based estimates of ΔpH) when calculating temperature during an ocean acidification event such as the PETM or ETM-2. Further, some caution must be taken when applying the Mg/Ca proxy over longer timescales (i.e., greater than 1 Myr), as the residence time for Ca in seawater is ~1 Myr (Broecker and Peng, 1982). On these timescales, if a secondary temperature proxy is applied, it is possible to estimate the

change in $\text{Mg}/\text{Ca}_{\text{sw}}$ by subtracting out the temperature signal from $\text{Mg}/\text{Ca}_{\text{planktic}}$ (e.g., Evans et al., 2018), similar to the coupled $\delta^{18}\text{O}_{\text{planktic}}$ and $\text{Mg}/\text{Ca}_{\text{planktic}}$ proxy approach for determining SST and SSS.

1.4. Thesis objectives

In this thesis, I aim to establish the first reliable foraminiferal proxy-based estimates for changes in sea surface temperature, salinity (Chapter 2) and pH (Chapter 3) for the second largest Eocene hyperthermal, ETM-2. Temperature and pH estimates are used to help constrain the first numerical simulations of climate/carbon cycle for the event (Chapters 2 and 3) and salinity results are compared with high-resolution global circulation model simulations of the hydrologic cycle in a warming world (Chapters 2). Additionally, long-term changes in ocean temperature, sea surface pH, and seawater elemental composition (i.e., $\text{Mg}/\text{Ca}_{\text{sw}}$) are documented during the LPEE to test theories of carbon release and warming over the interval (Chapter 4).

2. Subtropical Sea Surface Warming and Increased Salinity During Eocene Thermal Maximum 2

Abstract

Eocene Thermal Maximum 2 (ETM-2; ca. 54 Ma) represents the second largest of the major Eocene hyperthermals, yet comparatively little is known about the scale and rate of climatic change for key regions. Here we provide the first detailed records of subtropical sea surface warming and salinization for ETM-2 at two subtropical locations, ODP Sites 1209 (North Pacific) and 1265 (South Atlantic). Coupled planktic foraminiferal Mg/Ca and $\delta^{18}\text{O}$ indicate 2–4 °C of rapid warming and local salinization of ~1–2 ppt at both sites. The increase in sea surface temperature is equivalent to anomalies reported from higher-latitude sites, and is consistent with theory on the expected pattern of spatial temperature response to greenhouse gas forcing in an ice-free world (i.e., no ice-albedo feedback). Similarly, the observed salinization is consistent with the hypothesis of enhanced meridional vapor transport and increased subtropical aridity in a warmer world.

2.1. Introduction

The early Eocene hyperthermals represent potential calibration points for establishing the response of global and regional warming and shifts in the hydrologic cycle to past changes in greenhouse gas (GHG) forcing because they represent transient and extreme warming events. Indeed, the magnitude of warming (4–8 °C; e.g., Dunkley Jones et al., 2013) during the largest hyperthermal, the Paleocene

Eocene Thermal Maximum (PETM; ca. 56 Ma), and evidence for intensification of the hydrologic cycle (e.g., Schmitz and Pujalte, 2007), are roughly within projections given the estimates of GHG forcing and PETM climate sensitivity (Kiehl and Shields, 2013; PALAEOSENS, 2012).

Subsequent, but smaller hyperthermals represent additional climate sensitivity calibration points. The Eocene Thermal Maximum 2 (ETM-2; ca. 54 Ma) followed the PETM by 1.8 to 2.0 Myr, and is characterized by surface and deep ocean warming (Lourens et al., 2005; Sluijs et al., 2009; Stap et al., 2009) that is roughly half that of the PETM. The magnitude of the accompanying carbon isotope excursion (CIE; -1 to -1.5% in benthic foraminifera; e.g., Stap et al., 2010; Figure 2.1) and dissolution horizons (Lourens et al., 2005; Nicolo et al., 2007; Stap et al., 2009; Westerhold et al., 2011) indicate a global carbon cycle perturbation that is also roughly half that of the PETM, though this has yet to be adequately constrained by independent observations or modeling.

In addition to warming, the hyperthermals are also characterized by a mode shift, or intensification, of the hydrologic cycle. In the case of the PETM this includes widespread evidence of increased intensity and/or frequency of extreme precipitation events and drought in continental settings (Foreman et al., 2012; Kraus and Riggins, 2007; Schmitz and Pujalte, 2007), and changes in runoff and/or precipitation and evaporation (or P–E) in marine settings (Nicolo et al., 2007; Tipple et al., 2011; Tripathi and Elderfield, 2004; Zachos et al., 2006; Zachos et al., 2003). In particular, open-ocean P–E, as inferred from changes in sea surface salinity (Δ SSS), appears to

have

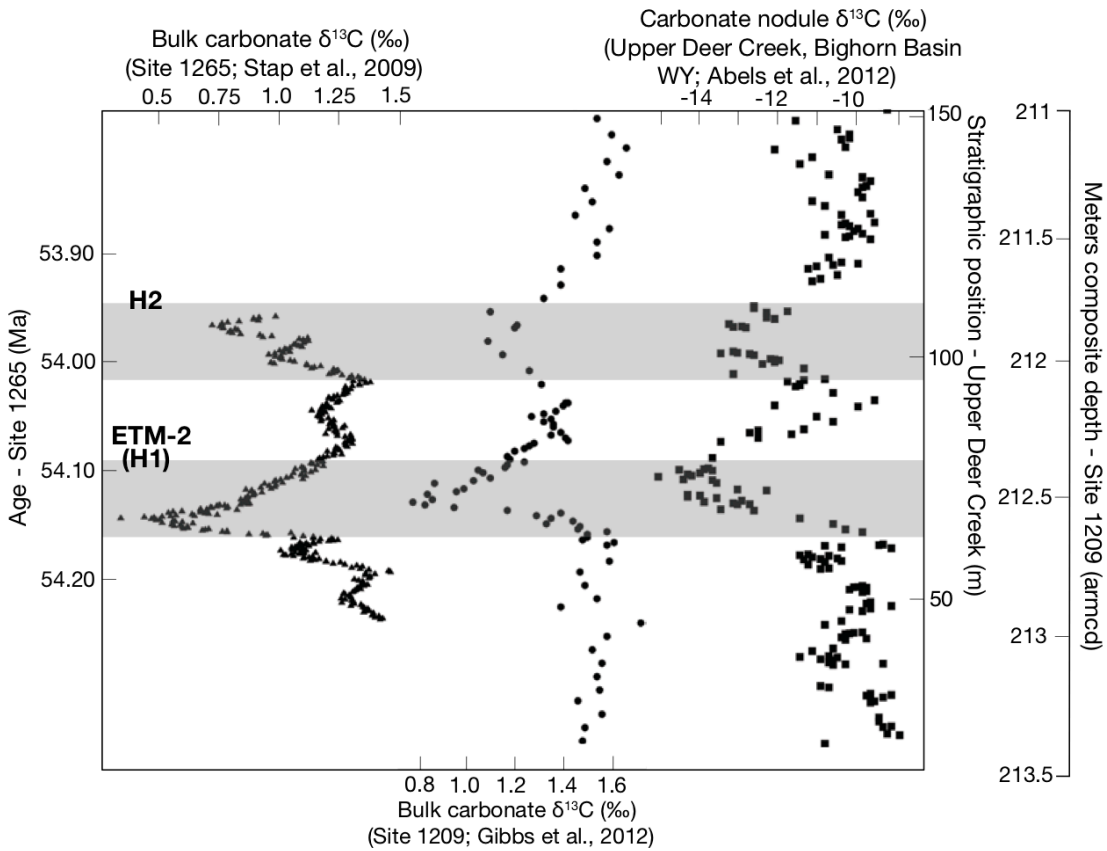


Figure 2.1. Bulk carbonate and carbonate nodule $\delta^{13}\text{C}$ from pelagic ocean sites (ODP Sites 1265 and 1209; Gibbs et al., 2012; Stap et al., 2009) and terrestrial Big Horn Basin Site (Abels et al., 2012) indicate that the perturbation to carbon cycle during ETM-2 was global. Site 1265 ages are based on the bulk carbonate Site 1263 age model of Lauretano et al. (2016).

declined in the subtropics, and increased in high latitudes. Similarly, cursory evidence for intensification of the hydrologic cycle has been documented for ETM-2 in the Arctic and North America (Abels et al., 2012; Sluijs et al., 2009), but few other locations.

Previous attempts to quantify ETM-2 warming have been limited to a few planktic $\delta^{18}\text{O}$ records which show modest (negative) anomalies (Lourens et al., 2005;

Stap et al., 2010a) possibly due to the influence of competing environmental factors, such as higher SSS and acidification (e.g., Spero et al., 1997), both of which would be consistent with a global carbon cycle perturbation. Subtropical salinization would be expected due to increased subtropical evaporation and transport of ^{18}O -depleted water vapor poleward on a global scale (e.g., Roberts et al., 2011; Tindall et al., 2010). To circumvent this, additional proxies such as Mg/Ca are required to constrain sea surface temperature (SST), which, with adjustments for pH (Evans et al., 2016), could then allow for estimation of changes in local surface seawater $\delta^{18}\text{O}$ ($\delta^{18}\text{O}_{\text{sw}}$) and thus SSS (e.g., Zachos et al., 2003).

To assess whether the magnitude of ETM-2 warming was globally uniform in the absence of an ice-albedo feedback (e.g., Kiehl and Shields, 2013), and to test if regional P–E declined in the subtropics due to increased meridional vapor transport consistent with GHG warming (Carmichael et al., 2015), coupled $\delta^{18}\text{O}$ and Mg/Ca paleothermometry in planktic foraminifera from ODP Sites 1209 and 1265 is applied to establish low- to mid-latitude SST and SSS anomalies.

2.2. Methods

2.2.1. Site Descriptions

Materials for this study were collected from sites in the North Pacific and South Atlantic (ODP Sites 1209 and 1265). Paleogeographic reconstructions place the sites at subtropical latitudes during the early Eocene (paleolatitude = $\sim 28^\circ$ N for Site 1209 and $\sim 42^\circ$ S for Site 1265; van Hinsbergen et al., 2015; Figure 2.3). Early Eocene (~ 55 Ma) paleodepth reconstructions indicate Sites 1209 and 1265 were

~1900 m and ~1850 m water depth, respectively (Takeda and Kaiho, 2007; Zachos et al., 2004).

2.2.2. Analytical methods

Acarinina soldadoensis, a planktic foraminifera species which likely hosted photosymbionts and thus resided in the photic zone (e.g., D'Hondt et al., 1994) were collected from the 250–355 μm sieve size fraction at 3–5 kyr resolution from ODP Sites 1209 and 1265, where ETM-2 is tightly constrained by carbon isotope and cycle stratigraphy (Gibbs et al., 2012; Lourens et al., 2005; Westerhold et al., 2011). Foraminifera (10–25 individuals) were crushed, homogenized, and split into two samples, one for trace elements and one for stable isotopes ($\delta^{13}\text{C}$ and $\delta^{18}\text{O}$). Trace element samples were cleaned following the oxidative reductive protocol of Barker et al. (2003), dissolved in 0.075N HNO_3 and analyzed via ICP-MS on a Thermo Element XR following the methodology of Brown et al. (2011) at UC Santa Cruz. The long-term reproducibility of consistency standard measurements indicates inter-run precision for Mg/Ca is $< 3\%$ (2 s.d.).

The sample portion used for stable isotope analyses ($\delta^{13}\text{C}$, $\delta^{18}\text{O}$, V-PDB) was not cleaned following oxidation/reduction protocol. Instead, they were sonicated for 1 minute in DI, and rinsed in methanol and DI. These samples were analyzed on a Thermo MAT 253 IR-MS coupled to a Kiel IV carbonate device at UC Santa Cruz. Based on replicate measurements of consistency standards, inter-run precision for $\delta^{13}\text{C}$ and $\delta^{18}\text{O}$ is $< 0.1\%$ (2 s.d.) and $< 0.16\%$ (2 s.d.), respectively. The bulk $\%\text{CaCO}_3$ ETM-2 record for Site 1209 was generated using a UIC Carbon Coulometer Analyzer

at UC Santa Cruz. Additionally, previously published bulk CaCO_3 ($\%$ and $\delta^{13}\text{C}$) and benthic foraminiferal $\delta^{13}\text{C}$ and $\delta^{18}\text{O}$ for Site 1265 (Stap et al., 2010a; Stap et al., 2010b; Stap et al., 2009) and bulk $\delta^{13}\text{C}$ and benthic foraminiferal $\delta^{13}\text{C}$ and $\delta^{18}\text{O}$ for Site 1209 (Gibbs et al., 2012; McCarren, 2009) were compiled.

2.2.3. LOSCAR carbon cycle and climate simulation of ETM-2

We applied the LOSCAR (Long-term Ocean-atmosphere-Sediment Carbon cycle Reservoir Model v2.0.4; Zeebe, 2012) climate/carbon-cycle model to simulate the ETM-2 carbon emission scenario given observations of CCD, planktic $\delta^{13}\text{C}$ and

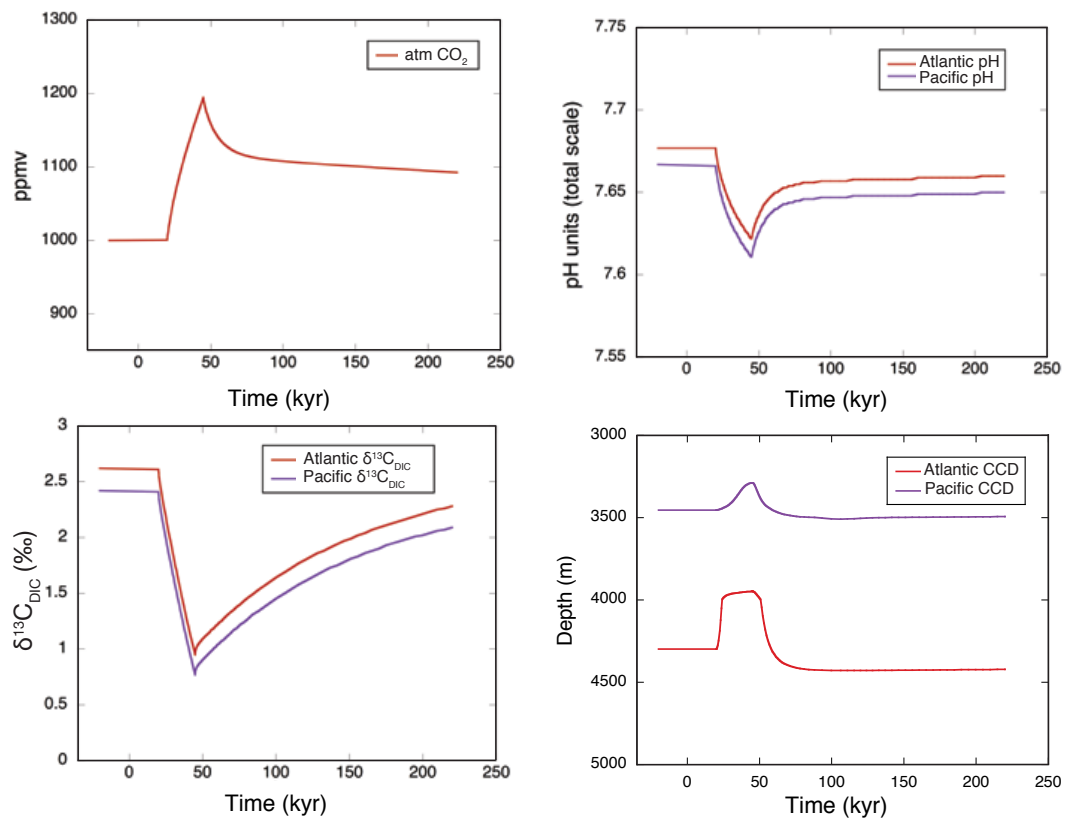


Figure 2.2. LOSCAR carbon emission scenario for ETM-2: 1300 Pg of carbon is released to atmosphere at time = 0 kyr with $\delta^{13}\text{C} = -40\%$. pH simulations for the emission scenario are used to pH-adjust planktic Mg/Ca and $\delta^{18}\text{O}$.

Δ SST (see Figure 2.2), with the goal of generating Δ pH estimates across the event so that pH-adjustments may be applied to planktic $\delta^{18}\text{O}$ and Mg/Ca. This model has been used extensively in previous research to simulate PETM and modern emission scenarios (Zachos et al., 2008; Zeebe, 2013; Zeebe et al., 2016; Zeebe and Zachos, 2013; Zeebe et al., 2009). The same boundary conditions (i.e., early Eocene ocean geometry and climate response functions based on early Eocene climate sensitivity) used in recent PETM simulations (Zeebe et al., 2016) are applied. The carbon emission scenario was then simulated by releasing 1300 Pg C over 25 kyr, at time = 0 kyr (consistent with the astronomically-paced onset described in Lourens et al. (2005)), using an intermediate $\delta^{13}\text{C}$ of -40‰ , with the aim of matching simulations to observations of the magnitude of the CIE and CCD changes (Figure 2.2). The ETM-2 simulation indicates a pH decrease of ~ 0.05 .

2.2.4. Calculating SST and SSS anomalies

From the coupled planktic Mg/Ca and $\delta^{18}\text{O}$ data (Figure 2.3), SST and SSS anomalies were computed (Figure 2.4) following the method of Zachos et al. (2003), but accounting for additional recently discovered proxy sensitivities. Specifically, the exponential constant of the Mg/Ca proxy calibration ('A' value; see Equation (1.4)) is potentially sensitive to seawater Mg/Ca ($\text{Mg}/\text{Ca}_{\text{sw}}$) (Evans et al., 2016). To account for this sensitivity, a range of constants are applied ('A' values from 0.05 to 0.09) that encompass the error in Mg/Ca-temperature regression fits for potential $\text{Mg}/\text{Ca}_{\text{sw}}$ values of the early Eocene (see Evans et al., 2016) and which contribute to the uncertainty in Δ SST (i.e., $\pm 1\text{ }^\circ\text{C}$). Anomaly envelopes do not incorporate any

changes in $\text{Mg}/\text{Ca}_{\text{sw}}$ across the hyperthermal, which is appropriate given the residence times of Mg and Ca in seawater (~ 13 Myr and ~ 1 Myr, respectively; Broecker and Peng, 1982) and the time interval of the anomaly envelope (~ 200 kyr). Furthermore, Evans et al. (2016) observed a pH effect on Mg/Ca which they quantified using a logistic fit to trends in field and laboratory data, though they could not statistically rule out a linear fit. Using a $\delta^{11}\text{B}$ -based estimate of ΔpH (Penman et al., 2014) for the PETM, Evans et al. (2016) applied a pH correction to planktic $\delta^{18}\text{O}$ and Mg/Ca data of Zachos et al. (2003) to highlight the significance of this effect. Because ΔpH has not yet been established for ETM-2, a ΔpH of -0.05 pH units was applied, estimated using LOSCAR carbon-cycle simulation of the event, as constrained by observations of the magnitude of the CIE, ΔSST , and changes in the CCD (see above). When both the logistic and linear pH-adjustment are applied, the pH effect on calculated Mg/Ca- ΔSST is less than -0.1 °C (Figure 2.5). Scaling the Site 1209 $\delta^{11}\text{B}$ -based PETM ΔpH (Penman et al., 2014) to ETM-2 using the planktic CIE recorded for each event leads to a larger ΔpH (-0.11 pH units), though the added effect on the results is minimal (< 0.1 °C decrease in ΔSST and < 0.2 ppt decrease in ΔSSS ; Figure 2.5).

Planktic $\delta^{18}\text{O}$ values were also adjusted with LOSCAR-based ΔpH (-0.05 pH units) following the *G. bulloides* relationship initially ascribed to a $[\text{CO}_3^{2-}]$ effect on $\delta^{18}\text{O}$ by Spero et al. (1997) (i.e., -2.51‰ per pH unit), before estimating and removing the Mg/Ca-based temperature influence to determine $\delta^{18}\text{O}_{\text{sw}}$ following the $\delta^{18}\text{O}$ -temperature relationship of Zachos et al. (2003) (i.e., 0.213‰ per °C). The

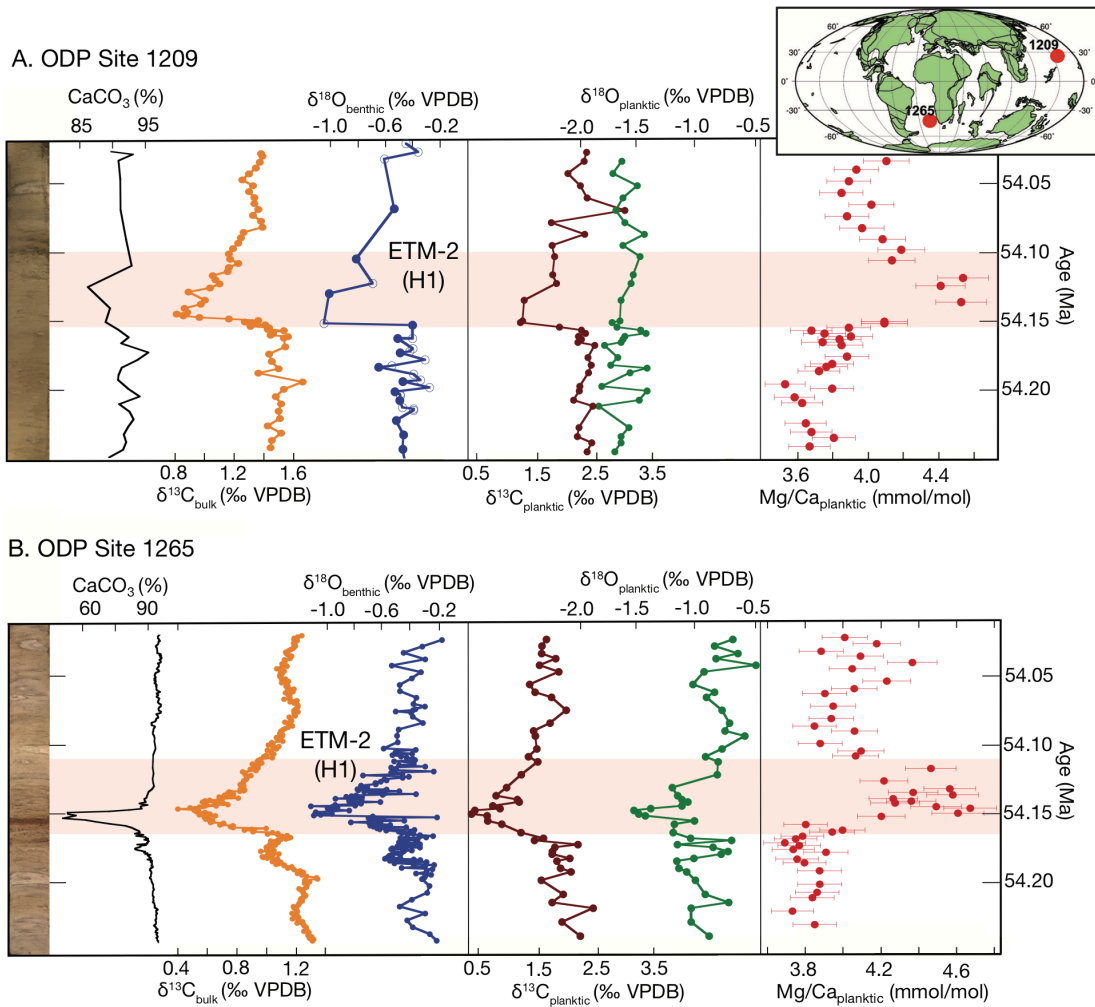


Figure 2.3. Panel A contains bulk CaCO₃ concentration (black line, this study) and $\delta^{13}\text{C}$ (orange markers, Gibbs et al., 2012), benthic (*N. truempyi*; blue markers) $\delta^{18}\text{O}$ (McCarren, 2009; this study = open markers), planktic (*A. soldadoensis*) $\delta^{13}\text{C}$ (burgundy markers), $\delta^{18}\text{O}$ (green markers) and Mg/Ca (red markers) (this study) for ODP Site 1209 (~28 °N paleolatitude; van Hinsbergen et al., 2015). Panel B contains bulk CaCO₃ concentration (black line) and $\delta^{13}\text{C}$ (orange markers, Stap et al., 2009), benthic (*N. truempyi*, blue markers) $\delta^{18}\text{O}$ (Stap et al., 2010b), planktic (*A. soldadoensis*) $\delta^{13}\text{C}$ (burgundy markers), $\delta^{18}\text{O}$ (green markers) and Mg/Ca (red markers) (this study) for ODP Site 1265 (42 °S paleolatitude). Data are plotted versus absolute age using the age model of Lauretano et al. (2016). The age model for Site 1209 was generated by tying the bulk $\delta^{13}\text{C}$ record at Site 1209 to bulk $\delta^{13}\text{C}$ at Site 1265. The site map displays the continental configuration at 54.0 Ma and indicates the paleo-locations of Sites 1209 and 1265. The pink shaded bar highlights ETM-2 (H1).

residual shifts in $\delta^{18}\text{O}_{\text{sw}}$ are then converted to ΔSSS using 0.25–0.50‰ per ppt from Zachos et al. (2003). This approach assumes 1) complete absence of ice sheets to influence $\delta^{18}\text{O}_{\text{sw}}$, and 2) the state of foraminifera preservation is uniform on short length scales, where lithology (i.e., % CaCO_3) is relatively invariant (Figure 2.3).

2.3. Results

At both sites, Mg/Ca increases by ~25% during the CIE (Figure 2.3). Given the long residence times of Mg and Ca in seawater (> 1 Myr), $\text{Mg}/\text{Ca}_{\text{sw}}$ should have remained constant over the duration of the study interval (~200 kyr); thus, the Mg/Ca anomalies must reflect ΔSST . During the CIE of ETM-2, planktic $\delta^{18}\text{O}$ decreases by < 0.5‰ during the CIE at South Atlantic Site 1265, but at Pacific Site 1209 show little to no decrease beyond background variability. In contrast, benthic $\delta^{18}\text{O}$ data show a similar 0.6 to 0.7‰ decrease at both locations (Figure 2.3; Stap et al., 2010b), suggesting similar warming of the deep-sea. Surface ocean CIEs of ~–1.5‰ are recorded in mixed-layer planktic foraminifera at both sites (Figure 2.3). % CaCO_3 decreases by ~40% at Site 1265 (Stap et al., 2009) and by ~5% at Site 1209 (this study) during the CIE (Figure 2.3).

2.4. Discussion

2.4.1. ΔSST and ΔSSS from the subtropics during ETM-2

We focus on establishing anomalies instead of absolute SST and SSS, as recrystallization of planktic foraminifera in carbonate rich pelagic oozes can shift $\delta^{18}\text{O}$ substantially (Dutton et al., 2005; Edgar et al., 2015). Any overprint of $\delta^{18}\text{O}$, however, should be uniform over the short length scales studied here, and features

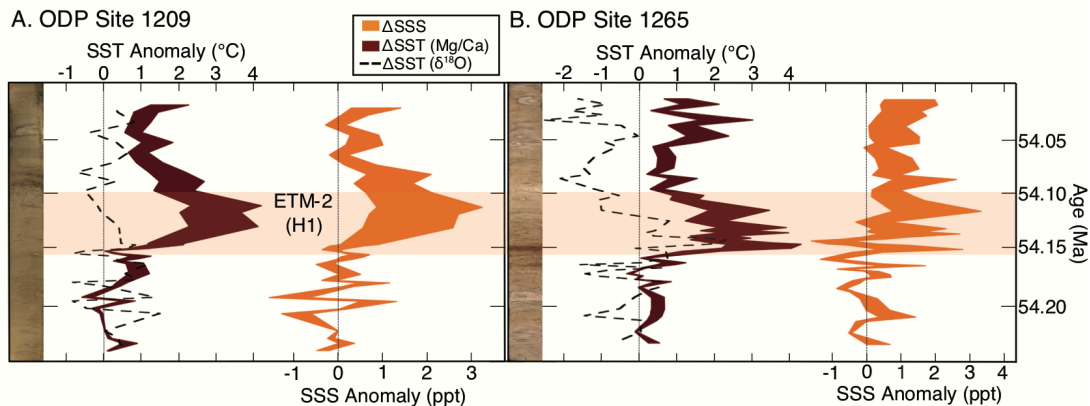


Figure 2.4. SST and SSS anomalies from ODP Sites 1209 (panel A) and 1265 (panel B). $\delta^{18}\text{O}$ -based SST anomaly is pH-adjusted. Mg/Ca-based SST and temperature-adjusted $\delta^{18}\text{O}_{\text{residual}}$ -based SSS anomalies are generated following the methodology outlined in the main text.

such as anomalies (and cycles) are typically preserved (Kozdon et al., 2013). In contrast, Mg/Ca seems to be minimally affected by recrystallization in relatively closed systems such as the low porosity pelagic muds at Sites 1209 and 1265 (Edgar et al., 2015; Kozdon et al., 2013). Dissolution on the other hand tends to decrease Mg/Ca and increase $\delta^{18}\text{O}$ in foraminiferal calcite (Dekens et al., 2002). Combining the dissolution-sensitivity of the modern foraminifera *G. ruber* (Dekens et al., 2002) with the simulated CCD response for ETM-2 (Figure 2.2), translates to a potential Mg/Ca-decrease due to dissolution of 1–3% and 2–6% in the Pacific and Atlantic, respectively. In terms of SST, this would dampen ETM-2 warming by $< 0.5\text{ }^{\circ}\text{C}$ in the Pacific, and $< 1\text{ }^{\circ}\text{C}$ in the Atlantic. In contrast, $\delta^{18}\text{O}$ dissolution sensitivity might suggest a potential increase in foraminiferal $\delta^{18}\text{O}$ of $< 0.04\text{ }_{\text{‰}}$ and $< 0.08\text{ }_{\text{‰}}$ for the Pacific and Atlantic, respectively. This magnitude of $\delta^{18}\text{O}$ enrichment would tend to amplify the calculated ΔSSS by only $< 0.25\text{ ppt}$, for both sites. However, estimates of

the effect of dissolution on the results are likely extremes, as the depth-dependent dissolution effect likely overcompensates for actual dissolution (Hönisch et al., 2013). Further, the muted $\delta^{18}\text{O}$ -temperature signal is observed at both sites, which experience variable decreases in $\% \text{CaCO}_3$.

In general, Mg/Ca suggest a similar degree of warming in the subtropical Pacific and South Atlantic during ETM-2. The $\delta^{18}\text{O}$ anomalies, in contrast, are small and unequal indicating local salinity-related anomalies in $\delta^{18}\text{O}_{\text{sw}}$. The total rise in SST amounts to 2–4 °C during ETM-2 (Figure 2.4) and residual shifts in $\delta^{18}\text{O}_{\text{sw}}$ indicate an increase in SSS of $+2 \pm 1$ ppt at Site 1209 and $+1 \pm 1$ at 1265 (Figure 2.4), suggesting increased subtropical aridity coincident with the warming.

2.4.2. Proxy-model comparison

The 2–4 °C warming in subtropical latitudes established herein is similar in magnitude to bottom water warming recorded by deep-sea benthic $\delta^{18}\text{O}$ (~ 3 °C; Stap et al., 2010b), where negligible changes in pH and salinity are predicted, and, by inference, areas of bottom water formation in the Southern Ocean and the Arctic (3–5 °C Δ SST; Sluijs et al., 2009). The spatial pattern of warming for ETM-2 is similar (albeit smaller in magnitude) to the pattern recorded by Mg/Ca- and GDGT-based temperature estimates during the PETM (e.g., Dunkley Jones et al., 2013) and expected pattern of warming in a largely ice-free world that lacks ice-albedo feedbacks (Kiehl and Shields, 2013).

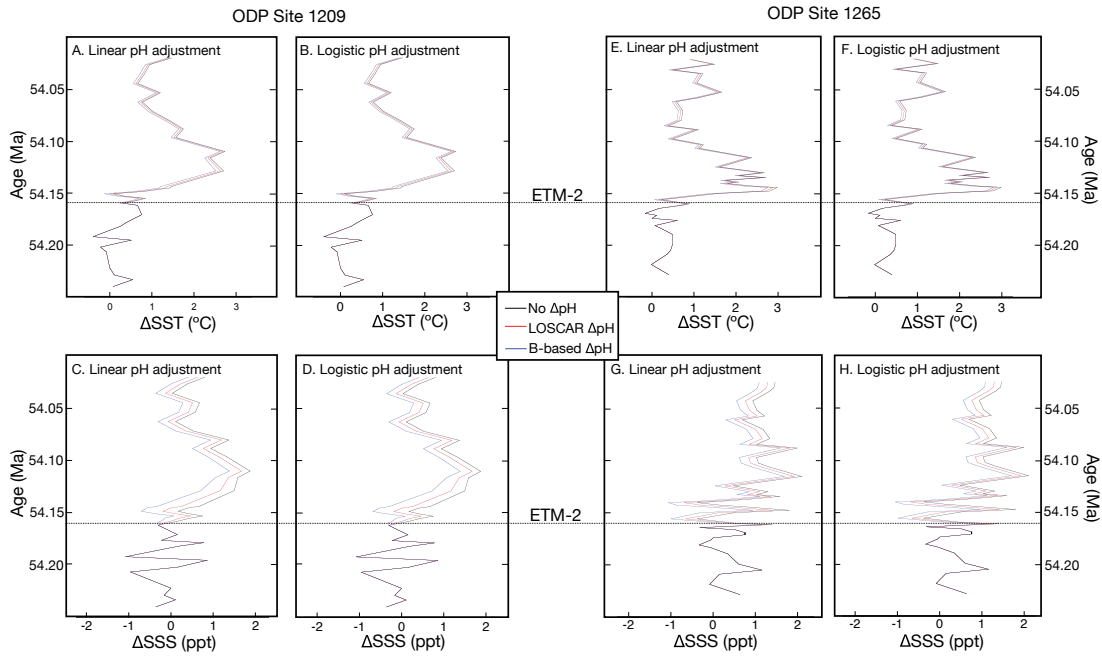


Figure 2.5. Sensitivity test showing the potential influence of pH adjustment on SST and SSS records at Sites 1209 and 1265 using 3 different pH change scenarios. The black line represents constant pH. The red line represents a pH change of -0.05 pH units derived from LOSCAR simulations and used in this study. We show both the linear and logistic pH adjustments of Evans et al. (2016). Intermediate values for the Mg/Ca temperature calibration sensitivity (ϵ value of 0.075) and intermediate $\delta^{18}\text{O}$ -salinity sensitivity (0.33‰ per salinity unit) are applied instead of the ranges used previously to clearly display the change in the ΔSST and ΔSSS records for each ΔpH scenario.

The finding of increased subtropical salinity during ETM-2 supports theoretical considerations of Eocene greenhouse warming effects on atmospheric vapor transport, ocean salinity and $\delta^{18}\text{O}_{\text{sw}}$. Simulations with isotope-enabled climate models (Roberts et al., 2011; Tindall et al., 2010) suggest relatively enhanced evaporation in the subtropics and net transport of ^{18}O -depleted moisture poleward, raising both the salinity and $\delta^{18}\text{O}_{\text{sw}}$ of subtropical surface waters. In one simulation involving the GISS ModelE-R (Roberts et al., 2011), P-E decreases in the subtropical

latitude bands from 15° S to 45° S, and from 10° N to 40° N, resulting in 0.5–2.0 ppt local increases in SSS, with the largest increases occurring in the subtropical Pacific and the North Atlantic and smallest increases in the equatorial Pacific. Similarly, the HadCM3 model was used to simulate differences between preindustrial and Eocene $\delta^{18}\text{O}_{\text{sw}}$ producing broadly similar results as GISS, with some local differences in the Indian and North Atlantic Ocean basins (Tindall et al., 2010). Interestingly, near Site 1265, simulated changes in P–E appear to be small, and thus, the site would record a reduced $\delta^{18}\text{O}_{\text{sw}}$ anomaly, consistent with our findings. While orbital forcing and ocean circulation might have contributed, the close covariation of SSS and SST with the CIE during the transient Eocene hyperthermals supports a first order feature of climate theory, that GHG warming drives increased meridional moisture transport, i.e., intensification of the hydrologic cycle (Carmichael et al., 2015).

2.4.3. Comparison with the PETM

The estimate of surface salinization recorded during ETM-2 at Site 1209 is similar in magnitude to the original estimate of a 2–3 ppt increase for the PETM (Zachos et al., 2003). This original estimate was neither adjusted for pH nor for other effects on either $\delta^{18}\text{O}$ and Mg/Ca. In order to compare the salinity anomalies for the PETM and ETM-2, PETM ΔSST and ΔSSS are recalculated using planktic Mg/Ca and $\delta^{18}\text{O}$ data from Zachos et al. (2003). Applying the same range in Mg/Ca-temperature sensitivity ('A' values) as used for ETM-2 and adjusting for ΔpH using simulated LOSCAR Pacific surface PETM ΔpH (~ -0.17 units; Zeebe et al., 2009), a salinity anomaly of 3 ± 2 ppt is estimated for the PETM at Site 1209 (Figure 2.6). The

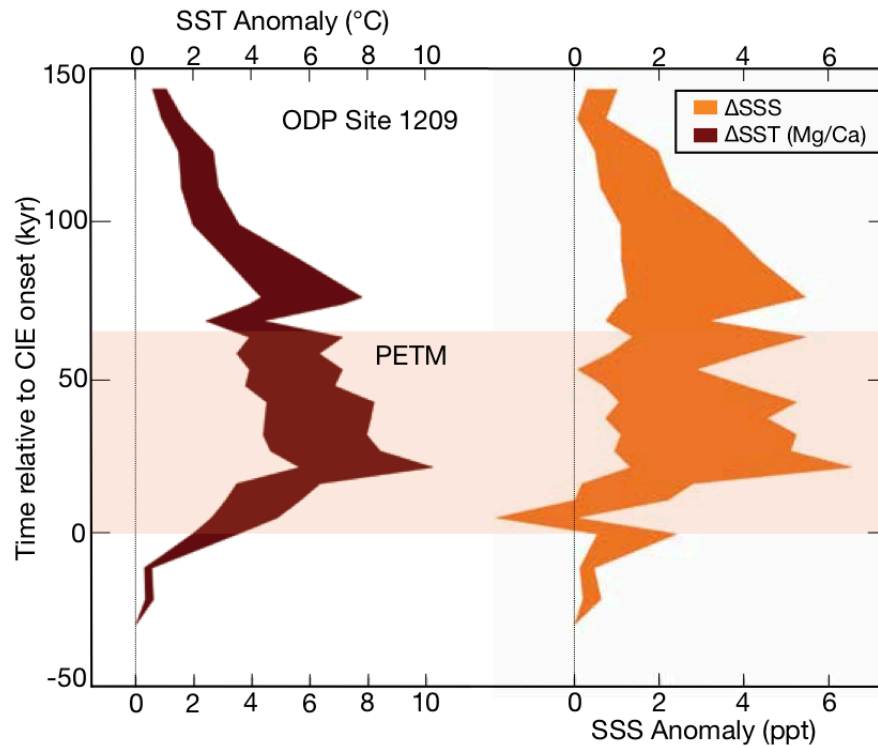


Figure 2.6. Δ SST and Δ SSS for the PETM at ODP Site 1209 using foraminiferal data (mixed-layer dweller *Acarinina soldadoensis*) from Zachos et al. (2003), which is pH-adjusted using Pacific surface Δ pH data from LOSCAR PETM simulations (Zeebe et al., 2009). SST envelopes are generated similarly to ETM-2 envelopes (Figure 2.5) using a range of Mg/Ca-temperature sensitivities ('A' values from 0.05 to 0.09) and include both linear and logistic pH-adjustments from Evans et al. (2016). Note that the larger range in both SST and SSS envelopes shown here, compared with Zachos et al. (2003), is a function of the larger range of Mg/Ca temperature sensitivities given the recommendations of Evans et al. (2016) (see main text). The range in Δ SSS incorporates a range of $\delta^{18}\text{O}$ -salinity sensitivities (the same range as the Δ SSS envelopes displayed in Figure 2.5; 0.25–0.5‰ per ppt).

LOSCAR PETM Δ pH is used rather than the $\delta^{11}\text{B}$ -based PETM Δ pH to maintain consistency when comparing the SSS anomalies for the two events. The large uncertainty in the recalculated PETM Δ SSS reflects a broad range of possible Mg/Ca-temperature sensitivities for the Eocene. When averages are compared, the PETM salinity anomaly at Site 1209 is slightly larger than the anomaly for ETM-2 (i.e., $3 \pm$

2 ppt for the PETM, and 2 ± 1 ppt for ETM-2; Figure 2.4; Figure 2.6), as one would expect, due to the relatively larger perturbations in temperature and hydrological cycle during the PETM compared to ETM-2.

2.5. Conclusions

In summary, this study documents patterns of sea surface warming and salinization of the subtropical ($\sim 28^\circ$ N) Pacific and subtropical ($\sim 42^\circ$ S) South Atlantic during ETM-2 that are consistent with theoretical predictions of the climatic response to GHG forcing, including globally uniform warming in the absence of ice-albedo feedback, a decrease in P–E, and a corresponding increase in SSS at subtropical latitudes, suggesting enhanced meridional vapor transport.

3. Surface Ocean Acidification During Eocene Thermal Maximum 2:

Implications for Carbon Release

Abstract

Eocene Thermal Maximum 2 (ETM-2) is the second largest early Eocene hyperthermal. Similar to the Paleocene-Eocene Thermal Maximum (PETM), ETM-2 is characterized by massive carbon emissions and several degrees of global warming and as such can serve as a calibration point in assessing the impacts of rapid CO₂ emissions on ocean carbonate chemistry and climate sensitivity. However, unlike for the PETM, the magnitude of the carbon cycle perturbation has yet to be tightly constrained by multiple independent proxies and models. Here we present the first records of ETM-2 surface ocean acidification, using stable boron isotopes in mixed-layer planktic foraminifera from two subtropical ODP Sites (1210 in the N. Pacific and 1265 in the S. Atlantic) and compare the results to carbon cycle box model simulations of carbon release and neutralization. Further, we generate high-resolution planktic B/Ca records to investigate possible changes in DIC and boron seawater chemistry during ETM-2 which are then compared against those established for the PETM.

3.1. Introduction

Superimposed on a ~6 Myr warming trend (ca. 58 to 52 Ma), early Eocene abrupt warming events, or hyperthermals, are associated with the release of ¹³C-depleted carbon to the ocean-atmosphere, and include the Paleocene Eocene Thermal

Maximum (PETM; ca. 56 Ma) and Eocene Thermal Maximum 2 (ETM-2; ca. 54.1 Ma). ETM-2 is roughly half the magnitude of the PETM with respect to the carbon release and climate change (Dunkley Jones et al., 2013; Harper et al., 2017; Sluijs et al., 2009; Stap et al., 2010b). Hyperthermals are characterized by rapid $\delta^{13}\text{C}$ decrease in global exogenic carbon reservoirs, or carbon isotope excursions (CIEs) (e.g., Abels et al., 2012; Kennett and Stott, 1991; Koch et al., 1992; Lourens et al., 2005), geochemical evidence of global warming (e.g., Dunkley Jones et al., 2013; Harper et al., 2017; Sluijs et al., 2009), and shifts in the global hydrologic cycle (e.g., Baczynski et al., 2017; Harper et al., 2017; Nicolo et al., 2007; Schmitz and Pujalte, 2007; Zachos et al., 2003).

Most importantly, hyperthermals are also linked to changes in ocean carbonate chemistry as evidenced by decreases in deep ocean %CaCO₃ (Colosimo et al., 2006; Stap et al., 2009; Thomas and Shackleton, 1996; Zachos et al., 2005) and, for the PETM, independent records of surface ocean pH decrease (Gutjahr et al., 2017; Penman et al., 2014). Such observations of changes ocean carbonate chemistry have been used to constrain numerical simulations of the carbon cycle and thus the flux of carbon during the PETM. Similarly, pelagic carbonate records of ETM-2 exhibit decreases in %CaCO₃, but of a smaller magnitude, suggesting proportionally reduced carbon emissions (e.g., Gibbs et al., 2012; Stap et al., 2009). However, independent constraints on the marine carbonate system are still lacking for ETM-2, limiting our ability to estimate the carbon fluxes, as well as changes in atmospheric CO₂. Addressing this deficiency would be an important step toward utilizing early

Eocene hyperthermal events to assess our understanding of the carbon cycle and associated feedbacks and climate sensitivity (e.g., Zeebe et al., 2009).

Boron isotopes of foraminifera provide a means of more directly constraining ocean pH and in turn, atmospheric CO₂ (e.g., Anagnostou et al., 2016; Bartoli et al., 2011; Chalk et al., 2017; Gutjahr et al., 2017; Hönisch et al., 2009; Penman et al., 2014). The PETM $\delta^{11}\text{B}$ data of Penman et al. (2014) and Gutjahr et al. (2017) indicate a global decrease in sea surface pH of ~ 0.3 units (e.g., Babila et al., 2018). When these records are compared to numerical simulations of sea surface acidification using carbon cycle models (e.g., Zeebe et al., 2009), they suggest that the mass of carbon released during the PETM tends towards larger estimates (i.e., $\sim 10,000$ Pg C), which may contradict observations of, for example, shifts in the CCD (e.g., Panchuk et al., 2008), although precise estimates of CCD shoaling are lacking for the PETM.

However, using the LOSCAR carbon cycle-climate model, Penman et al. (2014) noted that changes in the initial conditions of the simulations could significantly alter the model sea surface pH sensitivity to carbon release (e.g., initial pH, DIC, and CCD depth). Additionally, Gutjahr et al. (2017) found, using the cGENIE carbon cycle-climate model, that simulations driven by $\delta^{11}\text{B}$ -based pH observations generated CCD shifts more comparable to observations, largely due to differences in how the two models parameterize the CCD. While carbon cycle-climate simulations of carbon release for ETM-2 are limited, initial LOSCAR carbon cycle simulations which aim to match changes in planktic $\delta^{13}\text{C}$ (i.e., CIE of -1.5‰), temperature (i.e., an increase in sea surface temperature of 2-4 °C) and CCD observations (i.e., ~ 150 m and ~ 300 m

of CCD shoaling in the Pacific and Atlantic ocean basins, respectively) suggest a small degree of surface ocean acidification (i.e., -0.05 pH units; Harper et al., 2017). However, as with the PETM, LOSCAR simulations may underestimate the decrease in pH and carbon fluxes during ETM-2, perhaps due to model-specific parameterizations of the CCD. As such, independent constraints on pH during ETM-2 are desirable.

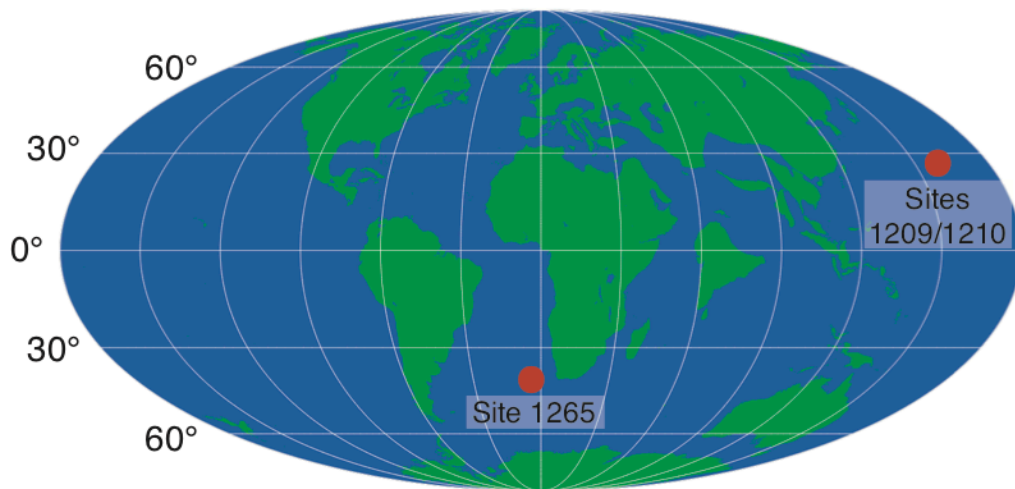


Figure 3.1. Map displaying the 54 Ma site locations (van Hinsbergen et al., 2015) and coastline reconstruction of Matthews et al. (2016).

Applying a strategy similar to that used for the PETM, we provide the first $\delta^{11}\text{B}$ -based reconstructions of ETM-2 surface ocean acidification from subtropical ODP Sites 1210 (N. Pacific) and 1265 (S. Atlantic). We compare our pH reconstructions and geochemical proxy records of climate and carbonate chemistry with carbon cycle-climate simulations to better characterize the amount and source (i.e., $\delta^{13}\text{C}$) of carbon released during ETM-2. Additionally, we compare our records of pH for ETM-2 to those established for the PETM to investigate how differences in

background conditions may have influenced the sensitivity of sea surface pH and temperature to carbon release for each event. While the boron-based proxies show large negative anomalies consistent with surface ocean acidification, we find that the magnitudes do not exactly scale with the carbon and oxygen stable isotope anomalies in comparison to the PETM. We assess how long-term changes in ocean carbonate chemistry and other factors might have influenced the B proxies.

3.2. Methods

3.2.1. Site descriptions

For this study, we targeted foraminifera-rich pelagic sections from relatively shallow water depths to minimize the impacts of carbonate dissolution. Materials were collected from the southern high of Shatsky Rise in the North Pacific (Sites 1209 and 1210) and Walvis Ridge in the South Atlantic (Site 1265) during ODP legs 198 and 208. ODP Sites 1209 (32° 39.11' N, 158° 30.36' E) and 1210 (32° 13.41' N, 158° 15.56' E) share roughly the same paleogeography during the early Eocene due to their close proximity. Paleogeographic reconstructions (paleolatitude = ~28° N; van Hinsbergen et al., 2015), place the Shatsky Rise sites in the subtropical North Pacific gyre during the early Eocene (Figure 3.1), where large-scale vertical mixing was unlikely. Early Eocene (~55 Ma) paleodepth reconstructions indicate Sites 1209 and 1210 were ~1900 m and ~2100 m water depth, respectively (Takeda and Kaiho, 2007). ODP Site 1265 (28° 50.10' S, 2° 38.35' E) was located at a paleolatitude of ~42° S (van Hinsbergen et al., 2015) (Figure 3.1) and paleodepth of ~1850 m during the early Eocene (Zachos et al., 2004). Upwelling on the scale of that observed at

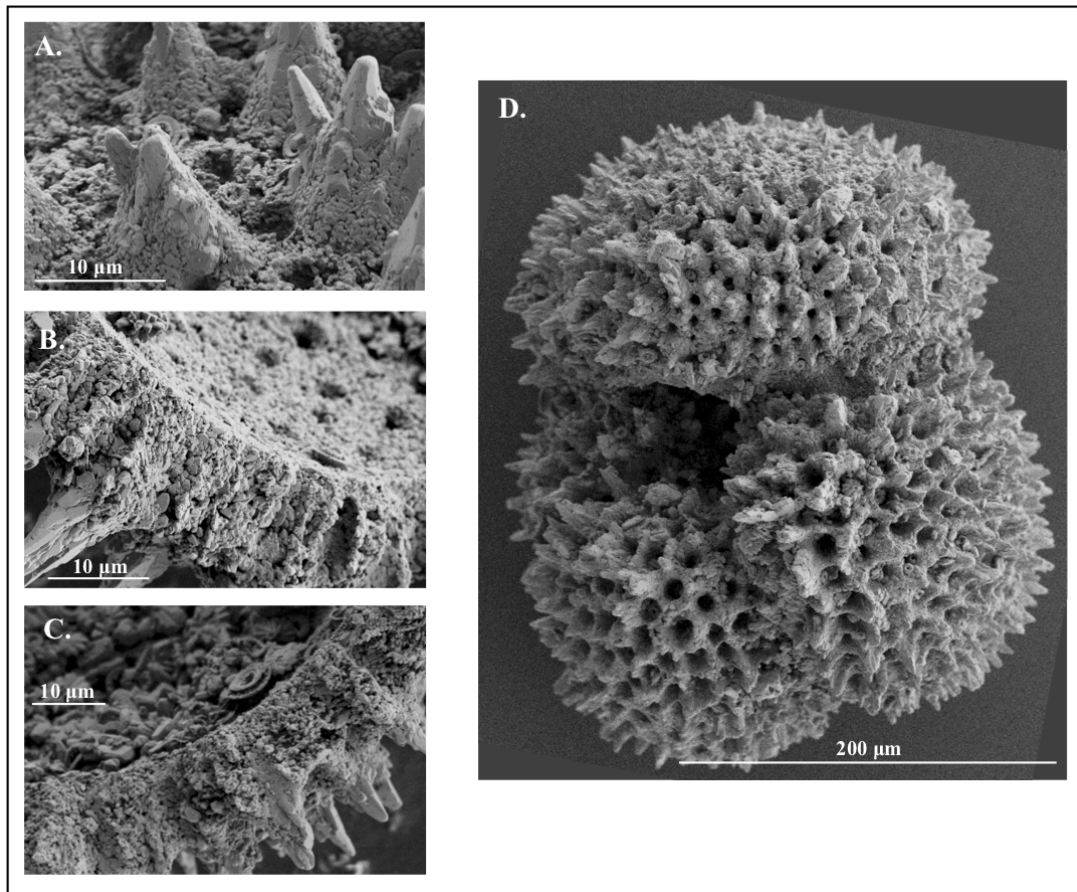


Figure 3.2. Scanning electron microscope (SEM) images of foraminifera preservation from ODP Site 1210 during Eocene Thermal Maximum 2 (EMT-2). *Acarinina soldadoensis* test walls exhibit partial recrystallization throughout EMT-2. A. Pre-CIE (ca. 54.054 Ma). B. Main body CIE (ca. 54.044 Ma). C. and D. CIE recovery (ca. 54.007 Ma).

ocean-continent boundaries was unlikely at Site 1265 due to its open ocean setting, however, a component of vertical mixing cannot be ruled out.

As with all carbonate rich pelagic sequences of this age, the planktic foraminifera shells are recrystallized, though uniformly over the length scale of EMT-2 (Figure 3.2; Figure 3.3). As such certain geochemical parameters, specifically $\delta^{18}\text{O}$, will be compromised. However, studies of similar sections indicate that the major and

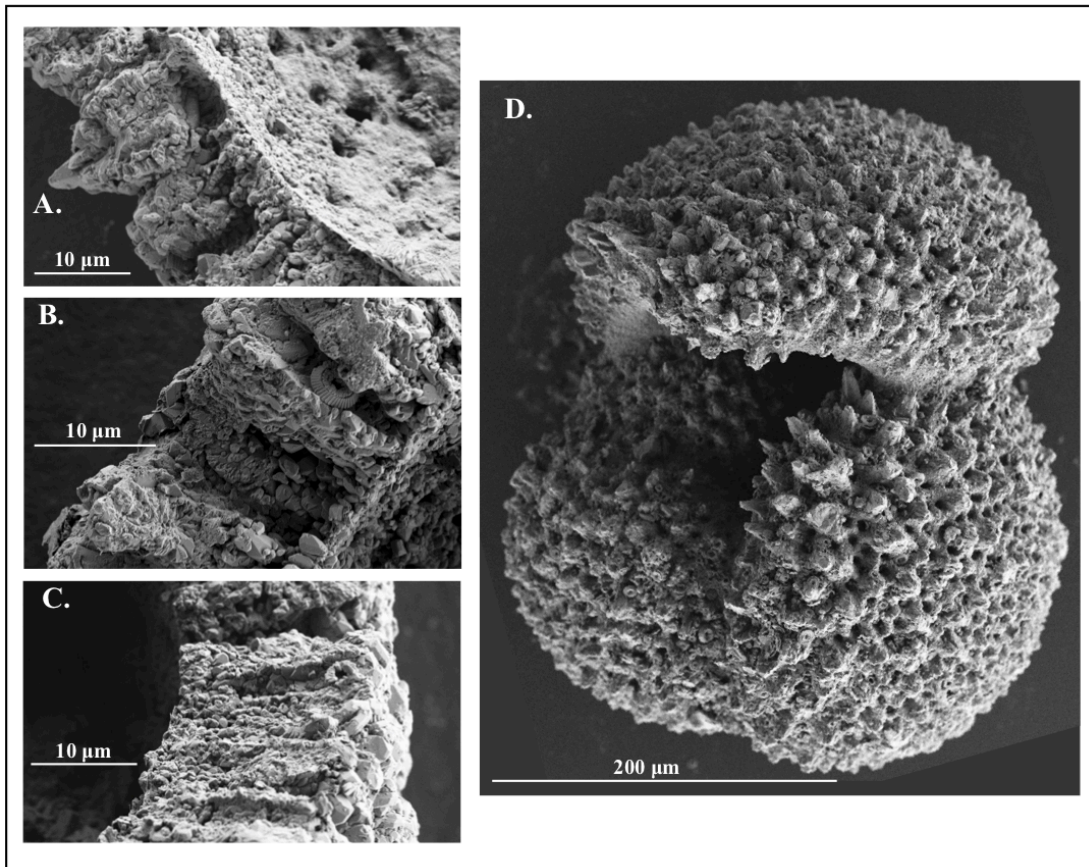


Figure 3.3. Scanning electron microscope (SEM) images of foraminifera preservation from ODP Site 1265 during Eocene Thermal Maximum 2 (EMT-2). *Acarinina soldadoensis* test walls exhibit partial recrystallization throughout EMT-2. A. Pre-CIE (ca. 54.054 Ma). B. Main body CIE (ca. 54.049 Ma). C. and D. CIE recovery (ca. 53.987 Ma).

minor trace element chemistries, specifically Mg/Ca and B/Ca, should not change significantly in these relatively closed systems (Edgar et al., 2015; Kozdon et al., 2013). Indeed, baseline and peak PETM Mg/Ca and B/Ca values from Site 1209 (i.e., Penman et al., 2014; Zachos et al., 2003) are consistent, given latitudinal differences, with values from siliciclastic sections such as Bass River, where better foraminifera preservation is observed (i.e., Babila et al., 2016).

3.2.2. Analytical methods

Bio- and magneto-stratigraphic evidence (Bralower et al., 2002) indicate core section 1210B-19H-6 contains the ETM-2 record. To verify and determine the precise section depth of the CIE, stable carbon and oxygen isotopic analysis of bulk carbonate material was performed at ~2 cm resolution via Isotope Ratio Mass Spectrometry (IRMS) using a Thermo MAT 253 coupled to a Kiel IV carbonate device at the University of California, Santa Cruz. Samples were collected at 1 to 2 cm intervals before being washed and sieved to remove material < 63 μm in preparation for foraminiferal identification. ETM-2 was previously documented at ODP Sites 1209 (e.g., Gibbs et al., 2012) and 1265 (Lourens et al., 2005). Samples from Sites 1209 and 1265 were similarly washed and sieved prior to foraminiferal identification.

Samples of 10-20 mixed-layer planktic foraminifera, *Acarinina soldadoensis*, from the 250-355 μm size fraction were lightly crushed and cleaned following the oxidative-reductive cleaning procedures of Martin and Lea (2002). Samples were then dissolved in 0.075 N Optima grade HNO_3 before being analyzed for major, minor and trace elements (e.g., B/Ca and Mg/Ca) via Inductively Coupled Plasma Mass Spectrometry (ICPMS), with a Thermo Element XR following the methodology of Brown et al. (2011). Analytical error for minor and trace element ratios (i.e., $\pm 7\%$ for B/Ca and $\pm 3\%$ for Mg/Ca; 2SD) is computed using the long-term reproducibility of in-house solution consistency standards. Splits of the same sample material were also analyzed for $\delta^{13}\text{C}$ and $\delta^{18}\text{O}$ via IRMS prior to oxidative and reductive cleaning.

Foraminiferal sample material for $\delta^{13}\text{C}/\delta^{18}\text{O}$ analysis was briefly sonicated in DI, rinsed in methanol, and dried in a 40° C vacuum oven for 6-12 hours before analysis. Analytical error for $\delta^{13}\text{C}$ and $\delta^{18}\text{O}$ (± 0.1 ‰ and ± 0.16 ‰, respectively; 2RSD) is based on the long-term reproducibility of consistency standards (i.e., Carrera Marble). Additionally, to increase data resolution and help interpret data differences between sites, we include the bulk carbonate wt. % and $\delta^{13}\text{C}$, planktic Mg/Ca, $\delta^{13}\text{C}$ and $\delta^{18}\text{O}$, and benthic $\delta^{13}\text{C}$ and $\delta^{18}\text{O}$ data from ODP Sites 1209 and 1265 of McCarren (2009), Stap et al. (2009), Stap et al. (2010b), Gibbs et al. (2012), and Harper et al. (2017).

Stable boron isotopes ($\delta^{11}\text{B}$) were measured using negative thermal ionization mass spectrometry following Hönisch et al. (2009) on samples containing 90-160 individuals of 250-355 μm *Acarinina soldadoensis* from Sites 1210 and 1265. Similar to trace element analyses, samples for $\delta^{11}\text{B}$ were crushed and cleaned for clays, organic and adsorbed contaminants following the protocol of Barker et al. (2003). Cleaned material was then dissolved in 2N Optima grade hydrochloric acid just before analysis and three to ten replicate aliquots of the sample solution containing ≥ 1 ng boron were loaded onto outgassed zone-refined rhenium filaments, along with 1 μl of boron-free seawater to enhance ionization. Analyses were done on a Thermo TRITON thermal ionization mass spectrometer in negative mode (N-TIMS) at the Lamont-Doherty Earth Observatory. Individual replicates were rejected if they fractionated excessively (i.e. > 1 ‰) over the ~40 minutes of acquisition. Data uncertainty is reported as the larger of either the 2σ standard error (SE) of acceptable replicate analyses or the 2σ SE of an equal number of repeat measurements of an in-

house standard of NIST 951 precipitated in CaCO₃ matrix (vaterite) (see Foster et al. (2013) for details). $\delta^{11}\text{B}$ data have been generated for the PETM using the planktic foraminifera, *Morozovella*, (e.g., Gutjahr et al., 2017; Penman et al., 2014). However, specimens of *Morozovella* are rare within the ETM-2 interval making a direct comparison of ETM-2 records to the PETM records impossible. To address this deficiency, we collected and analyzed *A. soldadoensis* from ODP Site 1209 samples with published *Morozovella* $\delta^{11}\text{B}$ data to constrain species offsets.

3.2.3. LOSCAR simulations

LOSCAR (Long-term Ocean-atmosphere-Sediment CARbon cycle Reservoir model; Zeebe, 2012) has been used extensively to simulate climate and the carbon cycle over long and short timescales, such as during the late Paleocene and early Eocene (e.g., Komar et al., 2013), and the PETM (e.g., Zeebe et al., 2009). Here, we conduct new LOSCAR carbon cycle-climate simulations of ETM-2 using a combination of carbon sources and timescales. We present two release scenarios consistent with the orbitally-tuned age models of Stap et al. (2009), which yields a ~25 kyr release of carbon for ETM-2, and Westerhold et al. (2017) (used in this study), which yields a ~15 kyr release of carbon. Additionally, we simulate shallow to intermediate depth remineralization of organic carbon due to the temperature rise (e.g., Matsumoto, 2007; Zeebe, 2013).

In our simulations, 1300 Pg C with $\delta^{13}\text{C}$ of -25‰ is released (to simulate the release of organic carbon as proposed by DeConto et al. (2012)) in addition to 1300 Pg C with $\delta^{13}\text{C}$ of -50‰ (i.e., representing ^{13}C -depleted sources such as biogenic

methane as proposed by Lourens et al. (2005)). In essence, 2600 Pg of carbon with $\delta^{13}\text{C}$ of -37.5‰ is released over two timescales, 25 kyr and 15 kyr, at constant rates, with the aim of matching observed rates and magnitudes of change in the CCD (e.g., Lourens et al., 2005), $\delta^{13}\text{C}$ (Stap et al., 2010b; Harper et al., 2017), and proxy-based estimates of ΔSST and ΔpH (this study). We release a larger mass of carbon (i.e., twice as much as in previous ETM-2 modeling studies; Harper et al., 2017) to generate the pH excursion we estimate from $\delta^{11}\text{B}$ (see below for details). Following release, the -25‰ carbon is removed over 75 kyr and 85 kyr, for the 25 kyr and 15 kyr release simulations, respectively, simulating the eccentricity-paced (i.e., 100 kyr) release and storage of organic carbon (e.g., DeConto et al., 2012). However, there is no forced removal of the biogenic methane carbon (i.e., 1300 Pg C with $\delta^{13}\text{C}$ of -50‰). Thus, carbon cycle recovery following the CIE is forced with 1300 Pg of organic carbon burial with the aim of matching the observed abrupt recovery following ETM-2 (e.g., Stap et al., 2009). Additional ocean-atmosphere carbon removal (i.e., carbon cycle recovery) over these timescales is driven by the silicate weathering feedback in LOSCAR.

3.3. Results

3.3.1. Geochemical proxy records

Bulk carbonate $\delta^{13}\text{C}$ data indicate that ETM-2 was fully recovered in core section 1210B-19H-6, and exhibit a -0.8‰ CIE, comparable to Sites 1209 (-0.7‰ bulk carbonate CIE; Gibbs et al., 2012) and 1265 (-0.8‰ bulk carbonate CIE; Stap et al., 2009) (Figure 3.4). Benthic $\delta^{13}\text{C}$ and $\delta^{18}\text{O}$ decreased at Site 1210 during ETM-2

by 0.9‰ and 0.6‰, respectively (Figure 3.4). Planktic $\delta^{13}\text{C}$ decreased by 1.3‰ at Site 1210, which is similar in magnitude to planktic CIEs observed at other sites (–1.1‰ at Site 1209 and –1.4‰ at Site 1265; Harper et al., 2017) (Figure 3.4). Baseline planktic Mg/Ca from Shatsky Rise locations also show slightly higher pre-ETM-2 values when compared to pre-PETM from Site 1209 (Penman et al., 2014; Zachos et al., 2003), suggesting long-term warming consistent with benthic $\delta^{18}\text{O}$ (Figure 3.5; Figure 3.6). However, the baseline Mg/Ca is higher (and anomaly larger for ETM-2) at Site 1265 compared with Sites 1209 and 1210. Site 1210 planktic Mg/Ca increases during ETM-2 from ~3.6 mmol/mol to ~4.5 mmol/mol (Figure 3.6), which is similar with respect to absolute value and magnitude increase to that observed at Site 1209, and with respect to magnitude increase to that observed at Site 1265 (Harper et al., 2017).

At all sites (1209, 1210 and 1265) both planktic B/Ca and $\delta^{11}\text{B}$ decrease during the ETM-2 CIE (Figure 3.6). Site 1209 planktic B/Ca decreases from ~60 $\mu\text{mol/mol}$ to ~40 $\mu\text{mol/mol}$ (Figure 3.6). Coarse resolution B/Ca data from Site 1210, which correspond to the samples analyzed for $\delta^{11}\text{B}$, align well with the higher resolution 1209 record (Figure 3.6). At South Atlantic Site 1265 planktic B/Ca decreases from ~44 $\mu\text{mol/mol}$ to ~30 $\mu\text{mol/mol}$ (Figure 3.6) during. Planktic $\delta^{11}\text{B}$ decreases by 1.1‰ (from 15.8‰ to 14.7‰) at Site 1210, and by 1.5‰ (from 15.5‰ to 14.0‰) at Site 1265 (Figure 3.6).

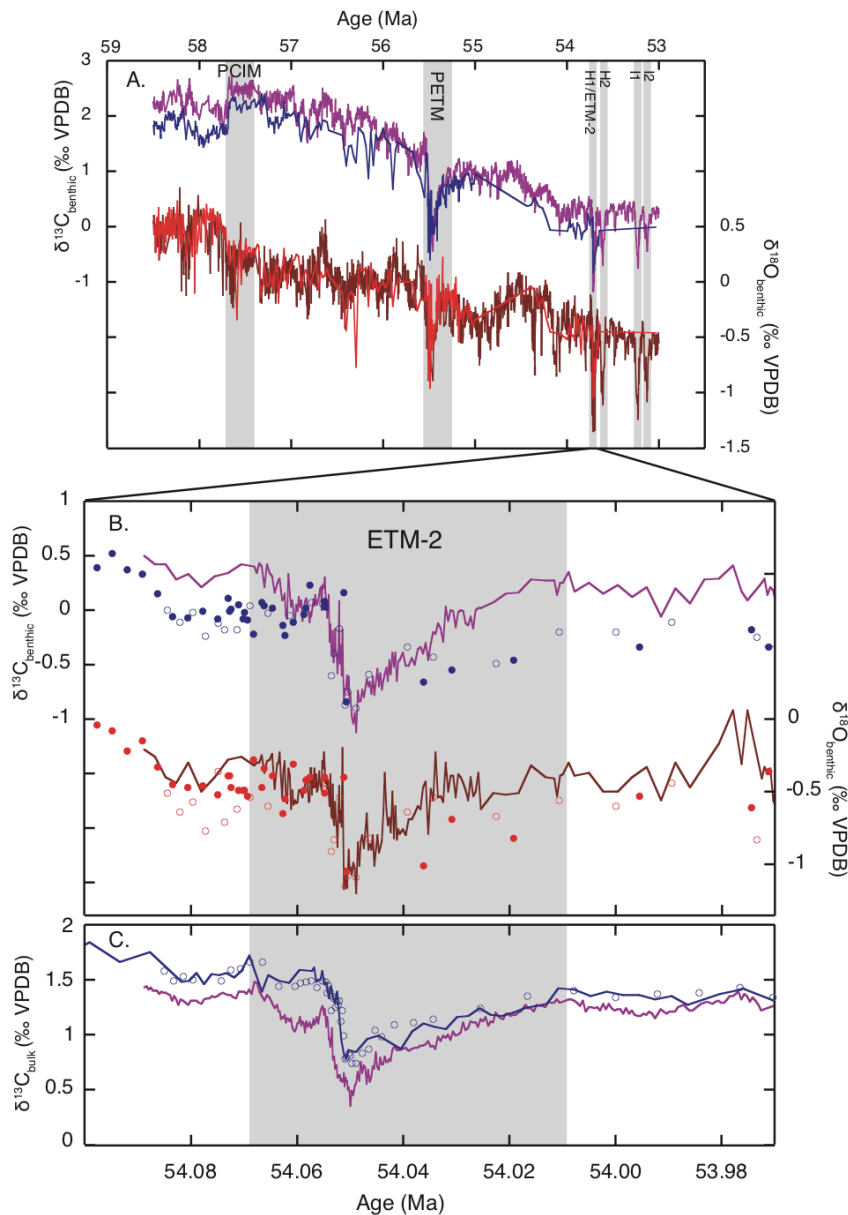


Figure 3.4. A. Late Paleocene early Eocene (LPEE) benthic $\delta^{13}\text{C}$ and $\delta^{18}\text{O}$ from ODP Sites 1209 (blue and red) and 1262 (purple and burgundy), placed on the option 1 age model of Westerhold et al. (2008) and compiled from McCarren (2009), Westerhold et al. (2011), Harper et al. (2017) Lourens et al. (2005), Zachos et al. (2005), Zachos et al. (2010), and Littler et al. (2014). B. Benthic $\delta^{13}\text{C}$ and $\delta^{18}\text{O}$ during Eocene Thermal Maximum 2 (ETM-2) from ODP Sites 1209 (closed circles; Harper et al., 2017; McCarren, 2009), 1210 (open blue and red circles; this study), and 1265 (purple and burgundy lines; Stap et al., 2010b). C. Bulk carbonate $\delta^{13}\text{C}$ during ETM-2 from Sites 1209 (blue line; Gibbs et al., 2012), 1210 (open blue circles; this study), and 1265 (purple line; Stap et al., 2009). Panels B and C are placed on the age model of Westerhold et al. (2017).

3.3.2. Reconstructing temperature for ETM-2 and the PETM

Absolute temperature records for ETM-2 are reconstructed using planktic Mg/Ca from Sites 1209 and 1265 of Harper et al. (2017) and early Eocene Mg/Ca of seawater (Mg/Ca_{sw}) estimates from Evans et al. (2018). We also include coarse resolution trace element data from Site 1210, which tends to align with observations from Site 1209, although the records slightly diverge during the recovery, which we attribute to analytical error. To calculate temperature, Mg/Ca-SST species calibration sensitivity (i.e., the pre-exponential and exponential calibration constants, or ‘B’ and ‘A’ values, respectively) consistent with Eocene seawater conditions is applied (i.e., Mg/Ca_{sw} = 2.24 mol/mol following Evans et al. (2018), ‘A’ = 0.075 following Evans et al. (2016), and ‘B’ = 0.38 following Anand et al. (2003)) with Mg/Ca_{sw} adjustments of Evans and Müller (2012). Further, planktic Mg/Ca data are adjusted for the pH-effect on Mg/Ca using site-specific $\delta^{11}\text{B}$ -based pH estimates (but excluding two $\delta^{11}\text{B}$ samples with less than 3 replicates, see open symbols in Figure 3.5b) and following the linear pH-adjustment of Evans et al. (2016). However, because $\delta^{11}\text{B}$ -based pH estimates depend partially on temperature, we iterate the temperature and pH. That is, we first compute temperature without the pH-adjustment to determine $\delta^{11}\text{B}$ -based pH. This pH estimate is then used to adjust the Mg/Ca data (i.e., we recalculate SST with the pH effect), and followed by a final pH calculation using this adjusted temperature estimate. Lastly, final reported temperatures are calculated by pH-adjusting Mg/Ca data with the final pH estimate. This strategy allows us to minimize the additional influence of temperature and pH on one another

with each iteration. pH-adjusting temperature estimates yields a decrease in relative temperature change of less than 0.5° C and 0.3° C for the PETM and ETM-2, respectively. We note that using non-pH-adjusted SSTs for calculation of pH from $\delta^{11}\text{B}$ dampens the negative pH excursion during ETM-2 by less than 0.015 pH units for Sites 1210 and 1265 (i.e., the effect is smaller than the respective ± 0.043 and ± 0.089 average propagated analytical uncertainty in relative pH estimates).

3.3.3. pH from $\delta^{11}\text{B}_{\text{foram}}$

pH is calculated from $\delta^{11}\text{B}_{\text{foram}}$ following Hönisch et al. (2019) and using routines of Zeebe and Wolf-Gladrow (2001). We include the effects of pressure (i.e., Millero, 1995) temperature and salinity on equilibrium constants, (i.e., pK_{B}^*). These calculations do not include any effect of seawater elemental composition on pK_{B}^* as this effect is generally considered to be minor with respect to the others. We use absolute temperature from pH-adjusted Mg/Ca-based SST (see above for details) and hold salinity at 35 ppt for both PETM and ETM-2 pH calculations. Note that adding 2 ppt salinization during the hyperthermals results in an amplification of acidification (i.e., ΔpH) of less than 0.015 pH units. ETM-2 and PETM $\delta^{11}\text{B}$ of seawater ($\delta^{11}\text{B}_{\text{sw}}$) estimates of Anagnostou et al. (2016) and Gutjahr et al. (2017) (i.e., 38.5‰ and 38.94‰, respectively) are used, as well as the aqueous fractionation (i.e., ϵ) of Klochko et al. (2006). To convert the *A. soldadoensis* and *M. velascoensis* $\delta^{11}\text{B}$ data to $\delta^{11}\text{B}_{\text{borate}}$ (and hence pH), we use the symbiont-bearing foraminifera multi-species $\delta^{11}\text{B}_{\text{foram}}$ versus $\delta^{11}\text{B}_{\text{borate}}$ sensitivity of Hönisch et al. (2019) (i.e. slope $m = 0.68$ for both species) and calibrate the species-specific $\delta^{11}\text{B}_{\text{foram}}$ versus $\delta^{11}\text{B}_{\text{borate}}$ intercept to

an initial PETM pH of 7.8 (i.e., intercept $c = 4.4$ for *A. soldadoensis*, and $c = 4.8$ for *M. velascoensis*). The difference in intercepts between these two species accounts for the observed $\delta^{11}\text{B}$ species offset at Site 1209 during the PETM (Figure 3.5). While both species are thought to have hosted algal photosymbionts based on $\delta^{13}\text{C}$ -size relationships, and thus likely resided in the mixed-layer photic zone (D'Hondt et al., 1994), we attribute this offset to small differences in depth habitat (i.e., 40 m for *M. velascoensis* and 70 m for *A. soldadoensis*) and therefore prescribe slightly different pressure values to pH reconstructions for each species.

pH uncertainty is calculated and displayed (Figure 3.5; Figure 3.6) according to three sets of considerations: 1) propagated analytical uncertainty from $\delta^{11}\text{B}$ measurements (2SE) as illustrated by green error bars, 2) propagated analytical uncertainty in addition to any uncertainty derived from full ranges in estimated SST, an appropriate range in sea surface salinity (i.e., 35 ± 2 ppt) given subtropical sea surface salinization documented in Harper et al. (2017), and reported uncertainty in $\delta^{11}\text{B}_{\text{sw}}$ for the PETM and ETM-2 (i.e., 38.94 ± 0.41 and 38.5 ± 0.03) following Anagnostou et al. (2016) and Gutjahr et al. (2017) (displayed as solid grey lines), and 3) including all above uncertainties, with the additional $\delta^{11}\text{B}_{\text{calcite}}$ versus $\delta^{11}\text{B}_{\text{borate}}$ calibration slope uncertainty (i.e., ± 0.04) of Hönisch et al. (2019) (displayed as dashed grey lines). We interpret the first two in the above error propagations to be representative of the uncertainty in relative pH changes during the event and the third as more representative of absolute pH uncertainty.

3.3.4. Carbon release simulations

The carbon flux scenarios of 1300 Pg C (−50‰) + 1300 Pg C (−25‰) generate warming of 1.5 °C when we apply a climate sensitivity of 3 °C per doubling of atmospheric CO₂ (Figure 3.7). Note that this requires a pre-event background atmospheric CO₂ of 1600 ppmv for the early Eocene, which is consistent with recent estimates based on stable boron isotopes (e.g., Anagnostou et al., 2016). Surface δ¹³C in the Pacific (Figure 3.7) and Atlantic decreases by −2.1‰ for both 25 kyr and 15 kyr release scenarios. The simulations generate pH excursions of −0.12 and −0.13 pH units for the 25 kyr and 15 kyr release scenarios, respectively (Figure 3.7). DIC increases in both release scenarios by ~120 μmol/kg, indicating the magnitude of the carbonate system response is fairly insensitive to the uncertainties in onset rate.

3.4. Discussion

3.4.1. Records of absolute temperature for ETM-2 and the PETM

Both subtropical ETM-2 SST records indicate similar pre-event baseline and peak-CIE temperatures of ~35° C and ~37.5° C, respectively (Figure 3.6). To obtain our absolute SST uncertainty envelop (i.e., grey lines in Figures 3.5 and 3.6), we propagate analytical uncertainty in Mg/Ca (i.e., ±3% 2SD), apply the Mg/Ca-temperature calibration uncertainty of Anand et al. (2003) in the pre-exponential constant ('B' value = 0.38 ±0.02), and prescribe a range of exponential constants ('A' values = 0.075 ±0.005) consistent with early Eocene Mg/Ca_{sw} of 2.24 mol/mol (Evans et al., 2018) following Evans et al. (2016). Additionally, we consider the full absolute uncertainty in the site-specific pH estimates (e.g., δ¹¹B_{calcite} - δ¹¹B_{borate} calibration

slope uncertainty, ± 0.04 , of Hönisch et al. (2019) is included; see below for details) when propagating error derived from pH-adjusting Mg/Ca, and include both pH-adjusted and non-adjusted Mg/Ca-based SST ranges within our uncertainty bounds.

The relative changes (i.e., $+2-3^{\circ}\text{C}$) and absolute temperature (i.e., pre-event baseline of $\sim 35^{\circ}\text{C}$) during ETM-2 documented in this study, are consistent with globally uniform warming. High latitude TEX₈₆ temperature records (e.g., Sluijs et al., 2009) and benthic records (e.g., Stap et al., 2010b) record high-latitude pre-event temperatures of $\sim 20^{\circ}\text{C}$ with $2-4^{\circ}\text{C}$ warming during the CIE. This implies that the full magnitude of the temperature signal is captured at all sites consistent with 1) the concept of weak polar amplification in response to GHG forcing in the absence of an ice-albedo feedback, and 2) the supposition that mixed-layer photosymbiont bearing foraminifera did not migrate to deeper waters. Further, this provides ancillary evidence, in addition to %CaCO₃ (e.g., Harper et al., 2017; Stap et al., 2009), that carbonate accumulation was continuous through the CIE at these sites.

To compare records of ETM-2 baseline and peak warmth to the PETM, we similarly reconstruct absolute temperature during the PETM at ODP Site 1209 using foraminiferal (*A. soldadoensis* and *M. velascoensis*) Mg/Ca of Penman et al. (2014) and Harper et al. (2017), Mg/Ca_{sw} of 2.24 mol/mol following the earliest Eocene estimates of Evans et al. (2018), and $\delta^{11}\text{B}$ -based pH of Penman et al. (2014). SST reconstructions indicate warming from an initial pre-PETM temperature of $\sim 34^{\circ}\text{C}$ to $\sim 40^{\circ}\text{C}$ during the main CIE at Site 1209 (Figure 3.5). Our calculated absolute temperature records using two species of planktic foraminifera from subtropical Site

1209 during the PETM are consistent with TEX₈₆ SST reconstructions from other locations during the hyperthermal (e.g., Frieling et al., 2018; Sluijs et al., 2007).

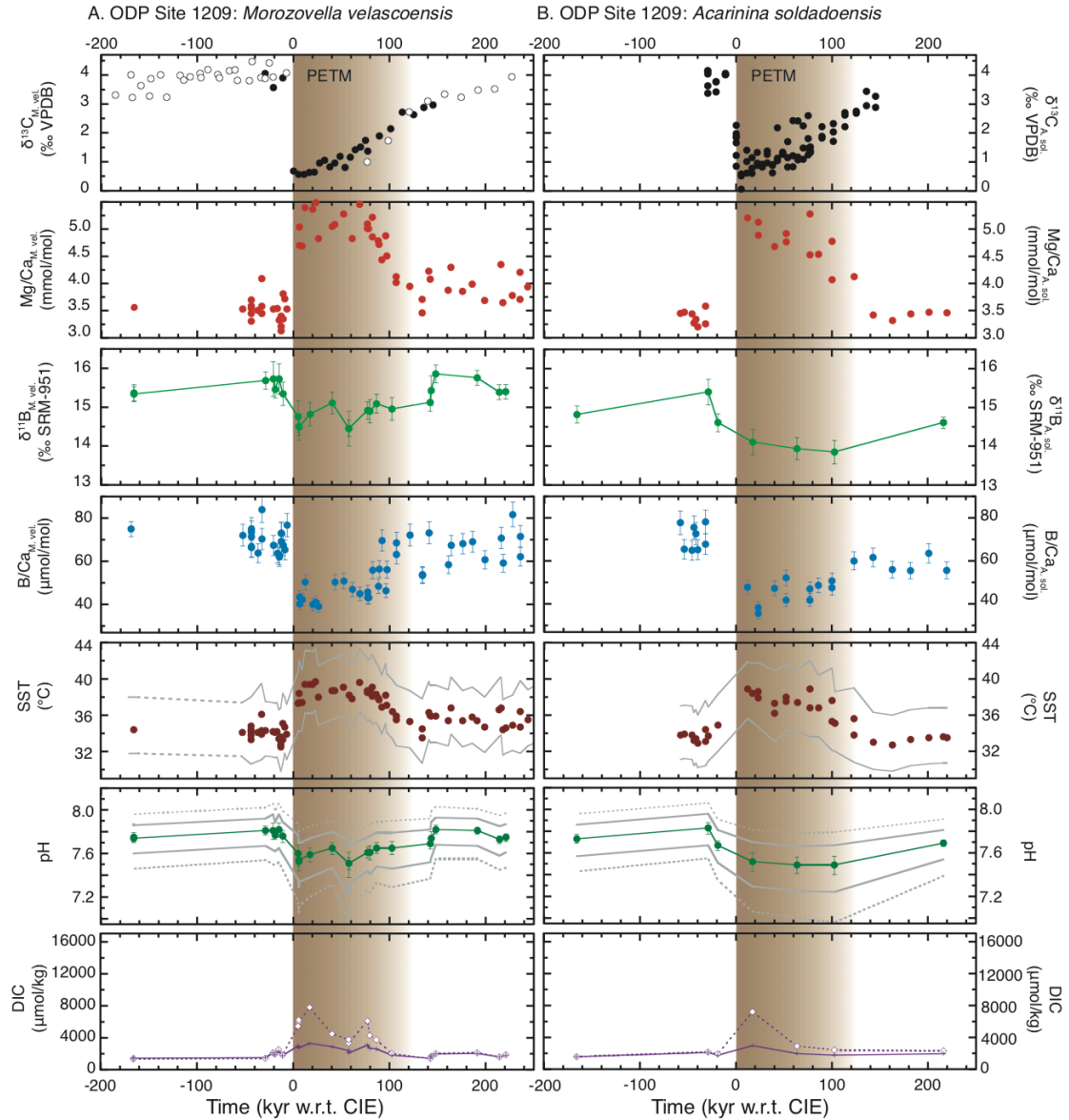


Figure 3.5. ODP Site 1209 geochemical data from planktic foraminifera *Morozovella velascoensis* (panel A; Penman et al., 2014; open circle $\delta^{13}\text{C}$ = this study) and *Acarinina soldadoensis* (panel B; Penman et al., 2014; $\delta^{11}\text{B}$ = this study) during the Paleocene-Eocene Thermal Maximum (PETM). We compute absolute sea surface temperature (SST) from Mg/Ca, pH from $\delta^{11}\text{B}$, and DIC from B/Ca and pH (see main text for details). For DIC, open diamonds = *Orbulina universa* calibration of Haynes

et al. (2017) scaled to pre-PETM DIC of 1750 $\mu\text{mol/kg}$; '+' symbols = diminished sensitivity calibration (see text for details) scaled to pre-PETM DIC of 1750 $\mu\text{mol/kg}$. For pH, relative uncertainty is plotted from both propagated $\delta^{11}\text{B}$ analytical error (green error bars), and propagated errors in measured $\delta^{11}\text{B}$, SST, sea surface salinity, and $\delta^{11}\text{B}_{\text{sw}}$ (solid grey lines); dashed grey lines include all propagated uncertainty in solid grey lines in addition to $\delta^{11}\text{B}_{\text{calcite}}$ vs. $\delta^{11}\text{B}_{\text{borate}}$ calibration uncertainty of Hönisch et al. (2019). Data are placed on the relative age model of Röhl et al. (2007).

3.4.2. Surface ocean acidification during ETM-2 and the PETM

$\delta^{11}\text{B}$ -based sea surface pH reconstructions with propagated analytical uncertainty decrease by $-0.26 +0.1/-0.05$ and $0.33 +0.12/-0.12$ pH units during ETM-2 at Sites 1210 and 1265, respectively (Figure 3.5; Figure 3.6). These estimates of ocean acidification are more conservatively revised to $-0.26 +0.15/-0.14$ and $0.33 +0.22/-0.16$ pH units for Sites 1210 and 1265, respectively, once the additional uncertainties described above are accounted for, while still excluding the $\delta^{11}\text{B}_{\text{calcite}}$ versus $\delta^{11}\text{B}_{\text{borate}}$ calibration slope uncertainty. The average pH change estimated here is similar in magnitude to that estimated for the PETM (i.e., ~ -0.33 ; Figure 3.5), despite large differences in planktic CIEs (i.e., $\sim -3.5\text{‰}$ and $\sim -1.3\text{‰}$ for the PETM and ETM-2, respectively; Figure 3.5; Figure 3.6; Harper et al., 2017; Penman et al., 2014; Stap et al., 2010a) and ΔSSTs (e.g., $\sim 5\text{ °C}$ versus $\sim 3\text{ °C}$ sea surface warming for the PETM and ETM-2, respectively; Figure 3.5; Figure 3.6; Harper et al., 2017; Sluijs et al., 2009), which suggests additional influences on pH, possibly from photosymbiont loss and/or local upwelling effects during ETM-2.

The presence of algal photosymbionts in *Morozovella* and *Acarinina* would have elevated the pH and $\delta^{13}\text{C}_{\text{DIC}}$ of the microenvironment in which foraminifer

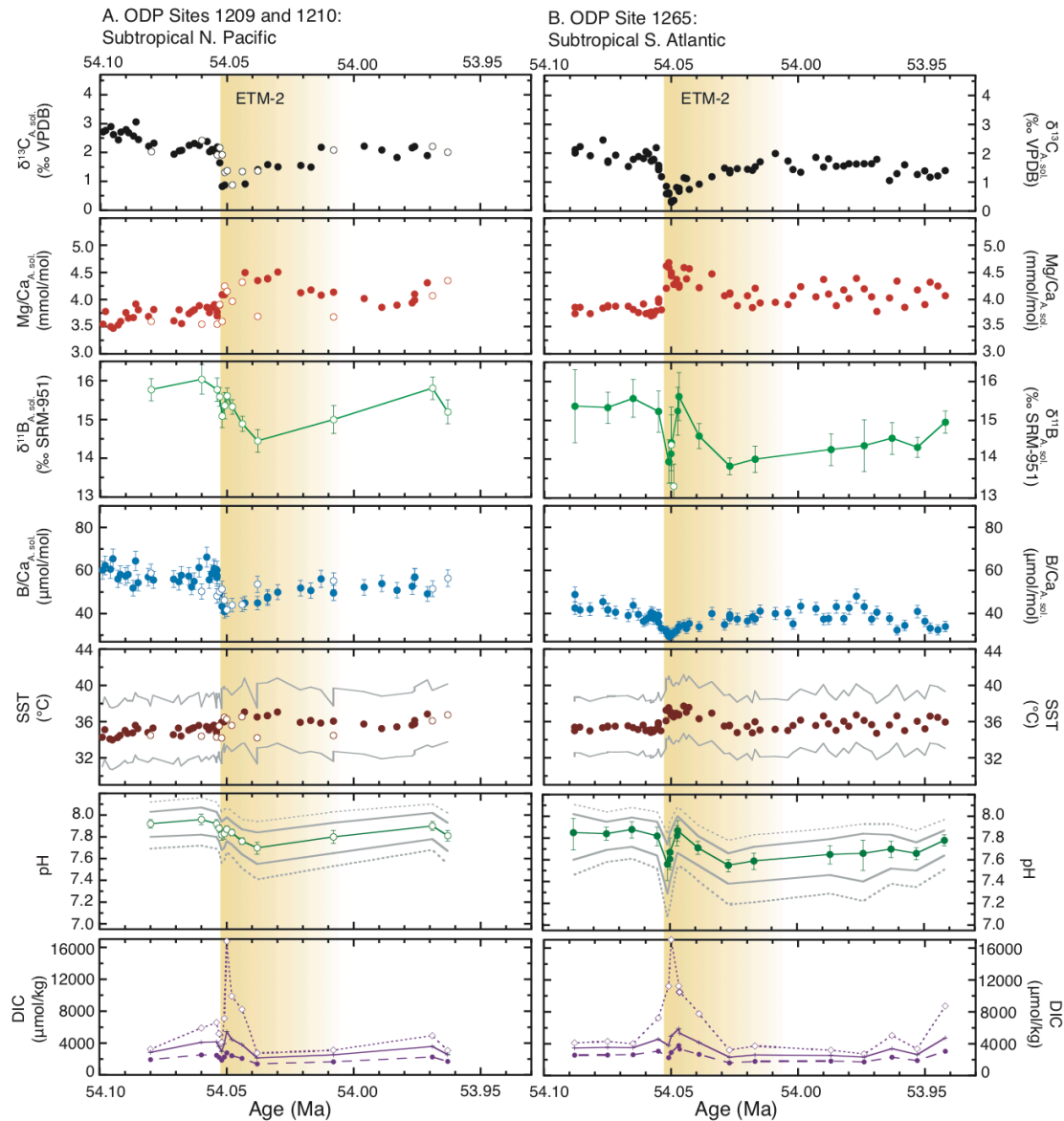


Figure 3.6. Geochemical data from planktic foraminifera *Acarinina soldadoensis* during Eocene Thermal Maximum 2 (ETM-2). Panel A shows data from ODP Sites 1209 (closed circles; this study; Harper et al., 2017) and 1210 (open circles; this study). Panel B shows data from ODP Site 1265 (this study; Harper et al., 2017). We compute absolute sea surface temperature from Mg/Ca, pH from $\delta^{11}\text{B}$, and DIC from B/Ca and pH (see main text for details). For DIC, open diamonds = *Orbulina universa* calibration of Haynes et al. (2017) scaled to pre-PETM DIC of 1750 $\mu\text{mol/kg}$; ‘+’ symbols = diminished sensitivity calibration (see text for details) scaled to pre-PETM DIC of 1750 $\mu\text{mol/kg}$; closed circles = diminished sensitivity calibration scaled to pre-ETM-2 DIC of 2200 $\mu\text{mol/kg}$. For pH, relative uncertainty is plotted from both propagated $\delta^{11}\text{B}$ analytical error (green error bars), and propagated errors in measured $\delta^{11}\text{B}$, SST, sea surface salinity, and $\delta^{11}\text{B}_{\text{sw}}$ (solid grey lines);

dashed grey lines include all propagated uncertainty in solid grey lines in addition to $\delta^{11}\text{B}_{\text{calcite}}$ vs. $\delta^{11}\text{B}_{\text{borate}}$ calibration uncertainty of Hönisch et al. (2019). Data are placed on the absolute age model of Westerhold et al. (2017).

calcify (e.g., Hönisch et al., 2003; Spero and Lea, 1996). Accordingly, any loss, or bleaching, of photosymbionts due to warming would tend to amplify negative CIEs and negative pH anomalies during ETM-2 at both sites. However, the magnitude of acidification given the planktic CIE ($\sim 1.3\%$) during ETM-2 is disproportional to that of the PETM for both Sites 1265 and 1210 (i.e., the PETM displays a similar degree of acidification, despite that the planktic CIE is more than twice as large as ETM-2). Additionally, peak-CIE SSTs for the PETM and ETM-2 at Site 1209 are $\sim 40^\circ\text{C}$ and $\sim 38^\circ\text{C}$, respectively. Therefore, while photosymbiont loss cannot be entirely ruled out as a contributor to the large acidification signal during ETM-2, it is unlikely that, based on absolute temperature reconstructions for the two hyperthermals (Figure 3.5; Figure 3.6), mixed-layer foraminifera suffered an equal or higher degree of photosymbiont loss during ETM-2 compared with the PETM. The potential effect of photosymbiont loss on planktic $\delta^{11}\text{B}$ and $\delta^{13}\text{C}$ during hyperthermal events could be investigated further by characterizing the magnitude of the CIE and $\delta^{11}\text{B}$ anomalies of foraminifera within the same species, but over a range of surface to volume ratios (i.e., size dependent or ontogenetic). The overprint of photosymbiont loss on the CIE and $\delta^{11}\text{B}$ anomalies should be proportional to the amount of photosymbiont loss they suffer with respect to the seawater surrounding the test, which will vary depending on the surface to volume ratio of the foraminifera (e.g., D'Hondt et al., 1994; Hönisch et al., 2003). Therefore, additional size-distributed

foraminiferal $\delta^{13}\text{C}$ and $\delta^{11}\text{B}$ records are required to assess the influence of photosymbiont bleaching on boron-based proxy records during ETM-2 and the PETM.

During the early Eocene, Site 1210 was located within the subtropical N. Pacific gyre (Figure 3.1), where thermal stratification is strong and little to no upwelling is expected. While Site 1265 was also located in the open ocean during the early Eocene, the location (i.e., Walvis Ridge) may have experienced seasonal shifts in local water mass conditions associated with bathymetric induced upwelling, which may have led to possible expansions and contractions of the surface waters in the S. Atlantic (e.g., Kucera et al., 1997). Alternatively, more prolonged changes in Southeast Atlantic ocean circulation associated with ETM-2 (e.g., Jennions et al., 2015), may have contributed to enhanced regional upwelling during the event. Thus, we deduce that the -0.26 pH anomaly of Site 1210 is more representative of the global ΔpH than Site 1265. This is further supported by our pH-adjusted SST estimates for Site 1265, which tend to dampen and better align with the temperature record for lower-latitude Site 1210, once we account for the larger magnitude pH change at the site.

The new LOSCAR simulations of ETM-2 generate larger magnitude negative pH excursions than those previously published (i.e., $\Delta\text{pH} = -0.05$; Harper et al., 2017 Figure 3.7). When the age model of Westerhold et al. (2017) is applied to the data, the LOSCAR output slightly better aligns with the 15 kyr release scenario, which suggests ~ -0.13 pH excursion during the main body CIE of ETM-2 in the high

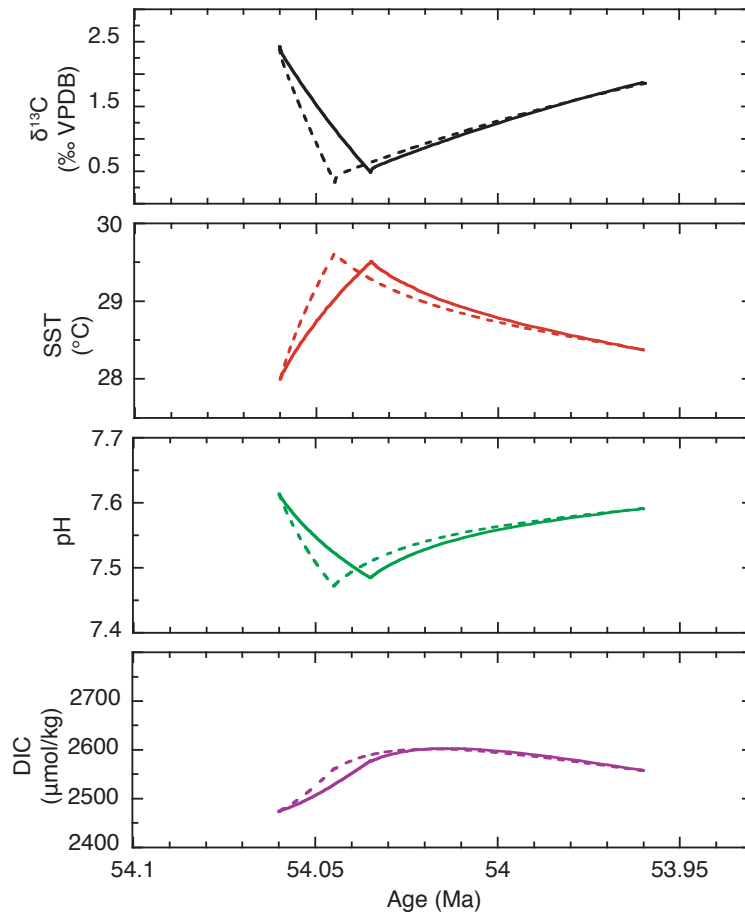


Figure 3.7. LOSCAR model output for the high latitude Pacific surface ocean for 1300 Pg organic C (-25‰) + 1300 Pg -50‰ C over 25 kyr (solid lines) and 15 kyr (dashed lines) ETM-2 simulations.

latitude surface Pacific (Figure 3.8). While this excursion is approximately half the magnitude of that estimated using $\delta^{11}\text{B}_{\text{foram}}$ from Site 1210, it does fit within the error of the estimated relative change in pH (i.e., $-0.26 +0.15/-0.14$). To generate a larger pH anomaly using LOSCAR (i.e., < -0.13), requires a mass of carbon release that would contradict observations of the magnitude of CCD shoaling (e.g., Lourens et al., 2005; Stap et al., 2009). Further, this larger mass of carbon would generate enhanced

warming, inconsistent with $\delta^{18}\text{O}_{\text{benthic}}$ and $\text{Mg}/\text{Ca}_{\text{planktic}}$ observations (even when a modest climate sensitivity of 3 °C per CO_2 doubling is applied to carbon release simulations), as well as require a more ^{13}C -enriched carbon source to fit within observations of the CIE. Such a carbon source is contradictory to the proposed orbitally-triggered mechanism for ETM-2 (i.e., DeConto et al., 2012; Lourens et al., 2005) but would support a volcanic source as hypothesized for the PETM (Svensen et al., 2004).

3.4.3. Estimating DIC from pH and $\text{B}/\text{Ca}_{\text{foram}}$

B/Ca of planktic foraminifer shells is a promising proxy of surface ocean carbonate chemistry (e.g., Allen and Hönisch, 2012; Yu and Elderfield, 2007), though the systematics are still under investigation (e.g., Babila et al., 2014; Henehan et al., 2015; Hönisch et al., 2019). Recent foraminiferal culturing studies using Paleocene-Eocene seawater chemistry (i.e., Haynes et al., 2017) demonstrate a higher sensitivity in foraminiferal B/Ca to $[\text{B}(\text{OH})_4^-]/\text{DIC}$ compared with culture calibrations with modern seawater chemistry. Further, Haynes et al. (2017) demonstrated that the primary controls on $\text{B}/\text{Ca}_{\text{foram}}$ with Eocene seawater are pH and $[\text{B}(\text{OH})_4^-]/\text{DIC}$, rather than foraminiferal growth rate (e.g., Salmon et al., 2016), light intensity (e.g., Babila et al., 2014) or other carbonate chemistry controls (e.g., Howes et al., 2017). Despite these advances, the proxy still remains only semi-quantitative as B/Ca sensitivity varies between foraminifera species grown under fixed conditions (e.g., Allen and Hönisch, 2012) and so some degree of uncertainty has to be accounted for

with application to extinct species. We can therefore only approximate the proxy-predicted DIC excursion across the PETM (Figure 3.5) and ETM-2 (Figure 3.6).

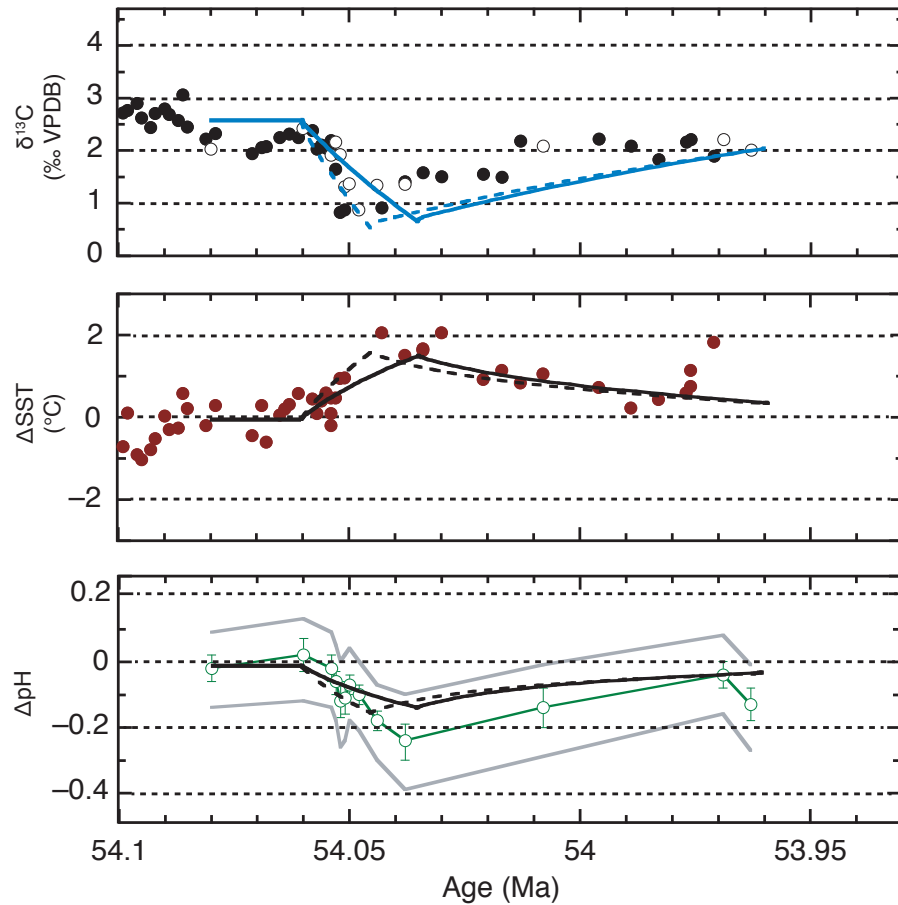


Figure 3.8. Geochemical data and interpretations from planktic foraminifera *Acarinina soldadoensis* during Eocene Thermal Maximum 2 (ETM-2) from Pacific ODP Site 1209 (closed circles) and 1210 (open circles). Data are placed on the absolute age model of Westerhold et al. (2017). Superposed on geochemical data is LOSCAR model output for the high latitude Pacific surface ocean for 1300 Pg -25‰ C + 1300 Pg -50‰ C over 25 kyr (solid black and blue lines) and 15 kyr (dashed black and blue lines) ETM-2 simulations.

Specifically, we start by applying the *Orbulina universa* B/Ca calibration of Haynes et al. (2017):

$$\text{B/Ca} = [\text{B(OH)}_4^-]/\text{DIC} * 1147 + c \quad (3.1)$$

We adjust the calibration intercept (c) to a reasonable pre-PETM baseline DIC value of 1750 $\mu\text{mol/kg}$ calculated using LOSCAR and pre-PETM parameters (i.e., atmospheric CO_2 of 800 ppmv and other parameters, such as CCD depth, following Zeebe et al. (2009)). We then use $\delta^{11}\text{B}$ -based pH estimates to compute $[\text{B(OH)}_4^-]$ and, in turn, DIC from $[\text{B(OH)}_4^-]$ and $\text{B/Ca}_{\text{foram}}$ following Haynes et al. (2017). B/Ca-based DIC display large increases during ETM-2 (DIC increases from $\sim 3000 \mu\text{mol/kg}$ to more than $16000 \mu\text{mol/kg}$; open diamonds in Figure 3.6) similar, but larger in magnitude, to DIC reconstructions for the PETM (Figure 3.5; Haynes et al., 2017). This unusually large increase in DIC, may simply be an artifact of applying a calibration of a modern species to an extinct species which might have had a lower sensitivity (Haynes et al., 2017). To test this possibility, we alter the sensitivity of Equation (3.1) until DIC increases by less than $2000 \mu\text{mol/kg}$ during both the PETM and ETM-2 (Figure 3.5; Figure 3.6; '+' symbols), and obtain Equation (3.2):

$$\text{B/Ca} = [\text{B(OH)}_4^-]/\text{DIC} * 1600 + c \quad (3.2)$$

While this new calibration sensitivity does not yet reflect experimental observations, it does suggest that calibrations using additional foraminifera species are required in order to reliably estimate DIC changes across hyperthermals going forward.

Based on the $\text{B/Ca}_{\text{foram}}$ versus carbonate chemistry relationships described by Haynes et al. (2017), the decline in B/Ca during the earliest Eocene following the

PETM could be a consequence of increasing DIC and/or decreasing pH from the PETM to ETM-2. However, this is inconsistent with $\delta^{11}\text{B}$ records that suggest a slight increase in pH ($\sim+0.1$ pH units) from the PETM to ETM-2 (Figure 3.5; Figure 3.6). Even with lower sensitivity (i.e., Equation 3.2), the DIC would have needed to increase by more than ~ 1000 $\mu\text{mol}/\text{kg}$ to account for the pre-PETM to pre-ETM-2 differences B/Ca with all else being equal (Figure 3.5; Figure 3.6; '+' symbols).

If DIC did not vary from the PETM to ETM-2, the patterns reconstructed here might reflect on secular shifts in global ocean boron chemistry (i.e., $\delta^{11}\text{B}_{\text{sw}}$ and [B]) either by enhanced removal of $\delta^{11}\text{B}$ -depleted boron from the oceans via a decrease in global hydrothermal activity, a decrease in boron riverine flux to oceans, an increase in boron adsorption onto clays, and/or an increase in oceanic crust alteration (see Hönisch et al., 2019). Over the late Cenozoic $\delta^{11}\text{B}_{\text{sw}}$ changed by as much by 0.1‰/Myr (Hönisch et al., 2019) so a shift of several tenths of ‰ over 2 Myr seems plausible. As for $\text{B}/\text{Ca}_{\text{foram}}$, in addition to possible changes in seawater concentrations, pH and DIC, other carbonate chemistry parameters, such as CO_3^{2-} , may be influencing the proxy, and/or foraminifera growth rates may be changing due to ocean acidification.

Are large changes in DIC over this time interval theoretically feasible? We estimate possible baseline differences in DIC with LOSCAR, using maximum estimated changes in pre-PETM and pre-ETM-2 baseline temperatures (i.e., 35° C to 40° C, which is notably larger than the difference in pre-event baseline SSTs of 34° C to 35° C), $[\text{CO}_3^{2-}]$ estimates (i.e., no significant change between the two pre-event

baselines following Komar et al. (2013)), and atmospheric CO₂ (i.e., 800 ppmv pre-PETM to 1600 ppmv pre-ETM-2 following differences in pre-event temperatures, and based on the earliest Eocene estimates of Anagnostou et al. (2016)). LOSCAR-based estimates of pre-PETM and pre-ETM-2 baseline DIC do not suggest large magnitude changes in DIC from event to event (i.e., increased background atmospheric CO₂ and temperature result in small differences in DIC reconstructions: ~1750 μmol/kg for pre-PETM and ~2400 μmol/kg for pre-ETM-2). However, when DIC calibrations (i.e., B/Ca–DIC proxy calibration intercepts) are scaled to these pre-event baseline DIC values and applied to the B/Ca_{foram}-based reconstructions using the diminished calibration sensitivity of Equation (3.2), slightly more reasonable changes in DIC are estimated for ETM-2 (i.e., increase from ~2400 μmol/kg to 3000 μmol/kg and 4000 μmol/kg during the main CIE, for Sites 1210 and 1265, respectively; closed circles Figure 3.6). These proxy-based changes are larger than those predicted by LOSCAR simulations (e.g., LOSCAR predicts an increase of only ~2380 to ~2500 μmol/kg from pre-event to CIE; Figure 3.7), which is similar to observations during the PETM (e.g., Haynes et al., 2017), indicating further calibration experiments are required to reliably apply planktic B/Ca as a proxy for DIC in the late Paleocene and early Eocene.

3.5. Conclusions

We present the first planktic foraminifera δ¹¹B and B/Ca data spanning ETM-2 from sites in the Atlantic and Pacific, which indicate global sea surface acidification of $-0.26 \pm 0.15 / -0.14$ (i.e., the N. Pacific Site 1210 record is interpreted as more

representative of the global sea surface pH signal due to paleogeographic location). The computed pH anomalies are similar to those estimated for the PETM, and exceed estimates based on carbon cycle simulations, which use records of the ETM-2 CCD and $\delta^{13}\text{C}$ anomalies to constrain carbon fluxes. To obtain a decrease in pH within the error of observations, the LOSCAR simulations require a higher carbon flux (i.e., double) than previously estimated for ETM-2. Combined carbon sources of biogenic methane (-50‰) and organic carbon (-25‰) are required to achieve this carbon flux and stay within the limits of the observed CIE. If we use the full Pacific sea surface pH anomaly from $\delta^{11}\text{B}_{\text{foram}}$ (i.e., -0.26), the LOSCAR simulations would require a much higher carbon flux. This would not only require a relatively enriched (i.e., $\delta^{13}\text{C}$ greater than -20‰) source of carbon, but it would necessitate a magnitude of warming that exceeds observations ($\sim 2\text{ }^\circ\text{C}$) assuming nominal climate sensitivity. DIC reconstructions suggest 1) a need for more proxy calibration data, including from additional planktic species, and under varied seawater chemistry, and 2) possible changes in boron seawater chemistry during the earliest Eocene.

4. Long-term Trends and Orbital Variability in Climate, the Carbon Cycle and Marine Chemistry During the Late Paleocene and Early Eocene

Abstract

The late Paleocene and early Eocene (LPEE) was an interval of long-term warming, characterized by sporadic transient episodes of abrupt global warming associated with the release of massive amounts of ^{13}C -depleted carbon to the atmosphere (hyperthermals). Observations of the carbonate compensation depth (CCD), sea surface temperatures (SST), bottom water temperatures (BWT), and surface and deep $\delta^{13}\text{C}$ indicate long-term greenhouse gas (GHG) induced warming during the LPEE. However, reconstructions of atmospheric CO_2 lack the detail and precision to verify such speculation. Here, changes in sea surface pH are quantified using $\delta^{11}\text{B}$ in planktic foraminifera from subtropical Pacific Sites 1209 and 1210, and infer changes in ocean carbonate chemistry using benthic and planktic foraminiferal B/Ca from Sites 1209 and 1262 (subtropical S. Atlantic), to constrain simulations of long-term carbon release during the LPEE, and, in turn, evaluate the likely source of carbon. Additionally, short- (i.e., orbital) and long-term (i.e. ~ 3 Myr) controls on planktic Mg/Ca are investigated to assess possible changes in SST and/or seawater Mg/Ca on these timescales.

4.1. Introduction

Over the Phanerozoic, Earth has experienced a number of episodes of long-term warming generally associated with and attributed to rising greenhouse gas

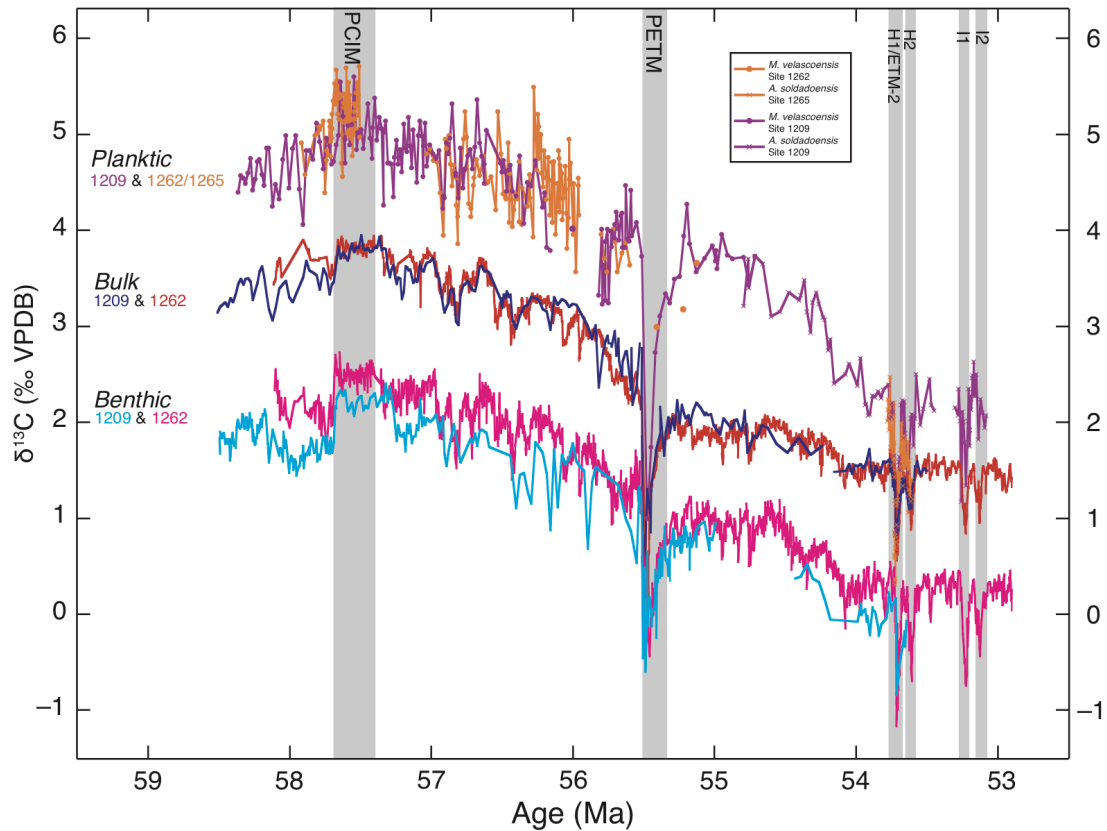


Figure 4.1. Compilation of late Paleocene early Eocene $\delta^{13}\text{C}$ data from Shatsky Rise (ODP Site 1209) and Walvis Ridge (ODP Sites 1262 and 1265). Planktic data: this study. Bulk carbonate data (Site 1209): this study, Gibbs et al., 2012, and Zachos et al., 2001. Bulk carbonate data (Site 1262): Littler et al., 2014. Benthic (*N. truempyi*) data (Site 1209): this study, McCarren 2008, Westerhold et al., 2011. Benthic (*N. truempyi*) data (Site 1262): Littler et al., 2014, Stap et al., 2010, McCarren et al., 2009. Major climate events have been highlighted (gray bars). Plotted against option 1 age model of Westerhold et al., 2008.

(GHG) levels (e.g., Anagnostou et al., 2016; Royer, 2014). One of the more prominent and enigmatic periods of warming occurred fairly recently during the transition from the late Paleocene to early Eocene, when global temperatures increased by 4–5 °C during a ~6 Myr period (LPEE; 58–52 Ma) climaxing in the Early Eocene Climatic Optimum (EECO; 50–53 Ma) (Miller et al., 1987; Zachos et

al., 2001; Zachos et al., 2008). As with previous warm episodes, this well-defined trend appears to be coupled to a rise in GHG levels as constrained by various proxies, though the nature of the coupling is unclear, in part due to the low resolution and high uncertainty in proxy data (Royer et al., 2014). A stronger coupling of the LPEE climate signal is observed with other carbon system parameters, specifically changes in ocean stable carbon isotope ($\delta^{13}\text{C}$) composition (e.g., Miller et al., 1987; Zachos et al., 2001; Zachos et al., 2008) and carbonate ion saturation as inferred from the carbonate compensation depth (CCD) (Hancock et al., 2007; Slotnick et al., 2015).

These general observations have been bolstered by recent advances in the development of high-resolution marine isotope (i.e., benthic foraminifera $\delta^{13}\text{C}$ and $\delta^{18}\text{O}$) records that, for the first time, place the long-term climate trends into an orbital framework (Figure 4.1 and Figure 4.2). These high-fidelity records resolve a number of short-term events superposed on the long-term trends, thus providing new insight into the character of carbon cycle/climate coupling (Littler et al., 2014; Westerhold et al., 2011). This includes the Paleocene-Eocene Thermal Maximum (PETM; ca. ~56 Ma), an extreme global warming event, and subsequent hyperthermals (e.g., Eocene Thermal Maximum 2; ETM-2; ca. ~54.2 Ma) which appear to be paced by orbital variations, but amplified by carbon cycle feedbacks (Dickens et al., 1997; Lourens et al., 2005). Although the coupling between climate and the carbon cycle likely differs for the short-term anomalies and the long-term secular trend, modeling suggests the long-term trends might be key to preconditioning the earth system for the anomalies (e.g., Komar et al., 2013; Lunt et al., 2011).

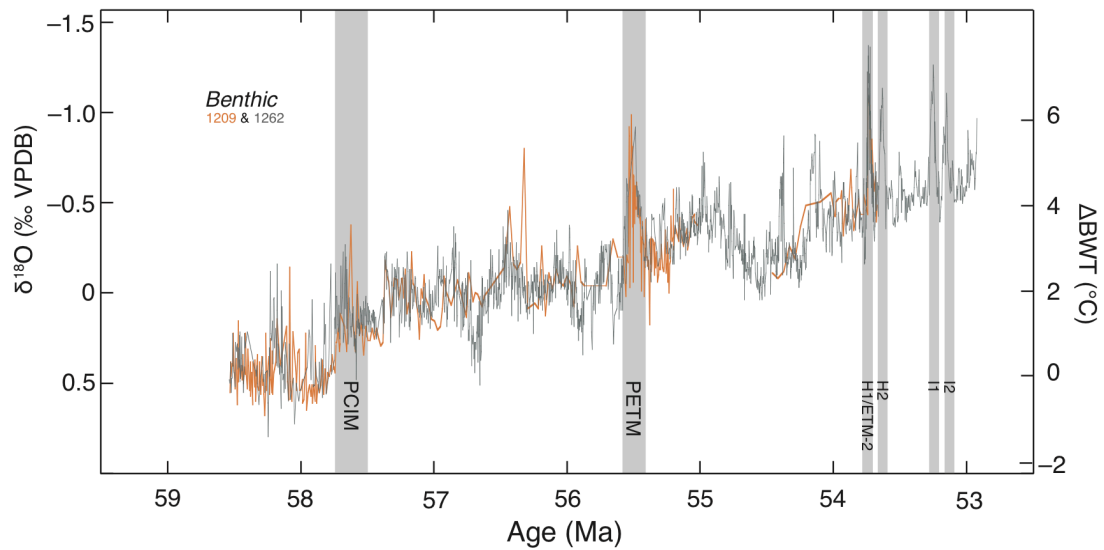


Figure 4.2. Late Paleocene and early Eocene benthic $\delta^{18}\text{O}$ data from ODP Sites 1209 and 1262. Benthic (*N. truempyi*) data (Site 1209): this study, McCarren (2008), Westerhold et al. (2011). Benthic (*N. truempyi*) data (Site 1262): Littler et al. (2014), Stap et al. (2010a), McCarren et al. (2008). Change in bottom water temperature (ΔBWT) calculated from $\delta^{18}\text{O}_{\text{benthic}}$ relationship of Miller et al. (1987) (i.e., 0.228‰ per $^{\circ}\text{C}$). Major climate events have been highlighted (gray bars). Plotted against option 1 age model of Westerhold et al. (2008).

The magnitude and relative timing of warming and changes in the CCD indicate that the LPEE warming was driven by a rise in atmospheric CO_2 nearly equivalent to that of the PETM (Komar et al., 2013; Zachos et al., 2008). Based on the long-term decline in $\delta^{13}\text{C}$ of benthic foraminifera, the rise in atmospheric CO_2 has often been attributed to elevated volcanic emissions, and/or decreased net burial of reduced carbon. Using a numerical model, Komar et al. (2013) found that warming during the LPEE was most likely due to decreased net burial of organic carbon, but could not rule out volcanic emissions entirely due to the large volume of the organic carbon reservoir that was required in order to reproduce observations with no

volcanic degassing. As a consequence, the exact cause of the long-term warming trend remains enigmatic.

The latest high-resolution, orbitally-tuned benthic isotope records, representing both the Atlantic and Pacific basins (ODP Sites 1262 and 1209; Figure 4.1), show that the long-term trend in climate during the LPEE initiated relatively abruptly, with a stepwise transition (decrease in $\delta^{18}\text{O}$ indicative of 2–3 °C of warming, and increase in $\delta^{13}\text{C}$ of +1‰) during the Paleocene Carbon Isotope Maximum (PCIM; 57.8 Ma). The abrupt initial warming was then followed by a series of large amplitude 400 kyr cycles, coherent in both climate and the carbon cycle, leading up to the PETM (Littler et al., 2014). The onset of warming, attributed to an increase in greenhouse gases (Littler et al., 2014; Westerhold et al., 2011), preceded a major reversal in the global carbon cycle as reflected in a long-term decline in carbon isotopes starting at the PCIM. As carbon isotopic values began to decline from ~57.8 Ma in the late Paleocene, large amplitude cyclic-like excursions became common, where oxygen and carbon isotopes both spike, possibly due to slow release of exogenic carbon into the atmosphere (Figure 4.1). The supposition that these ^{13}C cycles reflect GHG induced warming is supported by the local changes in sediment carbonate content, consistent with a shoaling lysocline, coincident with lower carbon isotopes and higher ocean temperatures inferred from $\delta^{18}\text{O}_{\text{benthic}}$ (Zachos et al., 2010). The dominant cycles have periodicities of 100 kyr and 400 kyr, and the amplitude appears to be ~0.2‰ and ~0.4‰, respectively, with 400 kyr cycles associated with temperature changes on the order of ~1–2 °C (e.g., Littler et al.,

2014). These orbital scale variations could be cycles of exchange of carbon between the ocean/atmosphere and crustal reservoirs. One possible carbon sink/source reservoir that could be exchanging on these timescales is the gas hydrate “capacitor”, which may allow for uptake, storage and subsequent release of reduced carbon (Dickens, 2003). Other possible reservoirs include areas where oxidation and reduction of carbon can take place in the terrestrial realm, such as peat and permafrost deposits (e.g., DeConto et al., 2012), which would be potentially sensitive to variations in regional precipitation (P–E) as influenced by eccentricity and greenhouse warming.

While records of stable carbon and oxygen isotopes and the CCD provide important constraints on the state of climate and the carbon cycle, additional information on the carbonate chemistry of the ocean is required to constrain and test models. Additionally, long- and short-term records of climate have been documented in benthic marine $\delta^{18}\text{O}$, but reliable records of mid- to low-latitude sea surface temperature (SST) during the LPEE are lacking. In particular, the planktic and bulk carbonate $\delta^{18}\text{O}$ records have been compromised by diagenesis (see Dutton et al., 2005; Edgar et al., 2015; Pearson et al., 2007; Schrag et al., 1995). The overarching goal of this study is to provide the context for evaluating models of the long-term evolution and coupling of the carbon cycle and climate during the late Paleocene to early Eocene warming trend and the long-term relation to short-term anomalies. To complement existing detailed marine isotope records, high-resolution mixed-layer planktic foraminifera Mg/Ca records are generated over the late Paleocene and early

Eocene to constrain long-term changes in SST. Additionally, planktic and benthic B/Ca (ODP Sites 1209, 1262 and 1265) and planktic $\delta^{11}\text{B}$ (ODP Sites 1209 and 1210) records are produced to assess surface and deep ocean carbonate chemistry. Further, the long-term controls on Mg/Ca and boron-based proxies are investigated to determine the possible influence of changing seawater chemistry during this time.

4.2. Methods

4.2.1. Site descriptions

The data compilation includes records from Sites 1262 and 1265 cored on the Walvis Ridge, South Atlantic during ODP Leg 208, and Sites 1209 and 1210 cored on Shatsky Rise, Pacific, during ODP Leg 198. The Walvis Ridge sites are comprised of carbonate rich foraminiferal nannofossil ooze and the Shatsky Rise sites are comprised of nannofossil ooze with clay.

Site 1262 (27° 11' S, 1° 35' E) and 1265 (28° 50.10' S, 2° 38.35' E) were cored at a water depths of 4759 m and 3083 m respectively with estimated paleodepths of ~1850 and 3600 m (Zachos et al., 2004). At these depths, during the LPEE, Site 1262 was close to the lysocline while Site 1265 was well above. Both Walvis Ridge sites have one prominent clay layer associated with the PETM, and lesser dissolution horizons associated with hyperthermals. The ca. 55 Ma paleolatitude for both sites is ~42° S (van Hinsbergen et al., 2015).

ODP Sites 1209 (32° 39' N, 158° 30' E) and 1210 (32° 13' N, 158° 16' E) were cored at the southern high of the central section of Shatsky Rise at water depths of 2387 and 2574 m, respectively. The paleolatitude of these sites at ~55 Ma is ~28°

N (van Hinsbergen et al., 2015), with paleodepths of ~1900 and ~2100 m (ca. 55 Ma; Takeda and Kaiho, 2007; van Hinsbergen et al., 2015). The lithology consists primarily of carbonate-rich, white nannofossil ooze, which becomes enriched in clay at the P/E boundary causing a brief transition into brown nannofossil ooze. There is a sharp basal contact at the onset of the PETM at the P/E boundary and a gradational upper contact as carbonate content rebounds in the Early Eocene.

Complete Paleocene benthic $\delta^{13}\text{C}$ records have been generated for Sites 1262 (Littler et al., 2014) and Site 1209 (Westerhold et al., 2011). A bulk carbonate $\delta^{13}\text{C}$ record has also been generated for the entire LPEE of 1262 (Zachos et al., 2010) and the early Eocene at 1209 (Gibbs et al., 2012). Here, the previously published early Eocene Site 1209 bulk carbonate $\delta^{13}\text{C}$ record is extended through the late Paleocene with data generated by this study.

4.2.2. Analytical Chemistry

Late Paleocene to early Eocene (~58.5–55.0 Ma; 233.9–216.7 arcmd) Site 1209 pelagic marine sediments were sampled at 10 cm resolution, freeze-dried and homogenized using a mortar and pestle. 50 μg s of each sample were analyzed for bulk carbonate stable carbon and oxygen isotopes at UC Santa Cruz using a Thermo MAT253 Ion Ratio Mass Spectrometer (IRMS) outfitted with a Kiel IV carbonate device. Long-term reproducibility of the Carrerra Marble (CM) standard indicates analytical precision (2sd) of $\pm 0.1\text{‰}$ and $\pm 0.16\text{‰}$ for $\delta^{13}\text{C}$ and $\delta^{18}\text{O}$, respectively.

Mixed-layer planktic foraminifera species *Morozovella velascoensis* and *Acarinina soldadoensis* samples (250–355 μm) spanning the LPEE were picked from

sediments from Sites 1209 (58.4–53.8 Ma) and 1262 (58.2–55.1 Ma). Depending on foraminiferal abundance, 5–25 specimens were lightly crushed, homogenized, ultrasonicated for 10 seconds and briefly rinsed with methanol. 50 µg of sample was then isolated and analyzed for $\delta^{13}\text{C}/\delta^{18}\text{O}$ via IRMS similarly to bulk carbonate samples. *M. velascoensis* was used for the record, with the exception of samples < 55 Ma, where the species becomes scarce, and *A. soldadoensis* was used.

Foraminiferal samples (i.e., splits of $\delta^{13}\text{C}/\delta^{18}\text{O}$ samples following Harper et al. (2017)) were prepared for multi-element analyses following an adjusted Mg/Ca-based cleaning method developed by Barker et al. (2003) to optimize for low boron contamination following Brown et al. (2011). Briefly, samples were rinsed in B-free milliQ and methanol to remove clay particles, oxidatively cleaned to remove organics, reductively cleaned to remove metal coatings, and thoroughly rinsed in B-free milliQ before being dissolved in optima-grade 0.075 N HNO_3 . The samples were analyzed at the UC Santa Cruz using an Element XR ICP-MS, with a front-end sample introduction system optimized for boron cleanliness (i.e., Teflon tubing and cyclonic spray chamber). In house multi-element standards allow for a suite of elements to be measured simultaneously. Certain element/calcium ratios are used to detect unclean samples and as a check for any contamination introduced during the cleaning procedure. Mn/Ca and Fe/Ca are used as metal coating contamination indicators, Al/Ca is used as a clay indicator, Ti/Ca is used as a silicate indicator, and Zn/Ca is used as a glove contamination indicator. Procedural blanks are used as contamination checks as well. The long-term reproducibility (2 sd) of consistency

standards for B/Ca and Mg/Ca is 6% and 3%, respectively. The calcium concentration matrix effect is accounted for by measuring a standard at multiple [Ca]. Typically, a trend of changing element/calcium ratios with [Ca] is not observed. When any matrix effect is observed it is accounted for via an exponential or linear correction function.

Boron isotopes were measured on a Thermo TRITON Thermal Ionization Mass Spectrometer in negative mode (N-TIMS) at Lamont-Doherty Earth Observatory following Hönisch et al. (2009). Samples containing 80–160 individuals (250–355 μm) of either *M. velascoensis* or *A. soldadoensis* from Site 1209 were cleaned similarly to samples prepared for ICP analysis, following the protocol of Barker et al. (2003). Individual replicates were rejected if they fractionated excessively (i.e. $> 1\text{‰}$) over the ~ 40 minutes of acquisition. Data uncertainty is reported as the larger of either the 2σ standard error (SE) of acceptable replicate analyses or the 2σ SE of an equal number of repeat measurements of an in-house standard of NIST 951 precipitated in CaCO_3 matrix (vaterite) (see Foster et al. (2013) for details). Site 1210 planktic $\delta^{11}\text{B}$ data from Chapter 3 is also included.

4.2.3. Compilation and timescales

High-resolution bulk $\delta^{13}\text{C}$ and benthic $\delta^{13}\text{C}$ records have been previously generated (Littler et al., 2014; Lourens et al., 2005; McCarren et al., 2008; Zachos et al., 2010; Zachos et al., 2005) and compiled (Littler et al., 2014) for the LPEE at Site 1262. In this study, the orbitally-tuned age model of Westerhold et al. (2008), option 1 is applied to the compiled records at Site 1262. Bulk carbonate $\delta^{13}\text{C}$ records from Sites 1265, 1210 and 1209 are then matched using Analyseries 2.0 to the high-

resolution, high-fidelity bulk carbonate $\delta^{13}\text{C}$ record at 1262 in order to place them on a common timescale.

4.3. Results

The new extended carbonate $\delta^{13}\text{C}$ record from Site 1209 closely mimics the Site 1262 record both in terms of long-term change (decrease of $\sim 2.4\%$ during LPEE) and orbitally-paced variability (Figure 4.1). Planktic (*M. velascoensis* and *A. soldadoensis*) $\delta^{13}\text{C}$ data shows a $\sim 3\%$ decline from the PCIM to the early Eocene (~ 53 Ma) in the Pacific and Atlantic (Figure 4.1). Planktic $\delta^{18}\text{O}$ exhibits little to no long-term change over the LPEE in the Pacific or the Atlantic, however, short-term, likely orbital-related signals (i.e., declining planktic $\delta^{18}\text{O}$ over intervals < 500 kyr), during the PETM and PCIM are preserved (Figure 4.3).

Planktic Mg/Ca increases prior to the PCIM from 58.5–57.8 Ma by ~ 1.5 mmol/mol in the Pacific and the Atlantic. From the peak-PCIM (~ 57.8 Ma) until ~ 56 Ma planktic Mg/Ca declines by ~ 2.0 mmol/mol, and then increases steadily by ~ 0.7 mmol/mol from 56 Ma to 53.5 Ma, with short-term hyperthermal-related Mg/Ca spikes associated with the PETM, ETM-2/H1, H2, I1, and I2 superposed (Figure 4.4). *A. soldadoensis* is slightly lower in Mg/Ca compared to *M. velascoensis*, perhaps due to a slightly deeper depth habitat as suggested in Chapter 3 (Figure 4.4). Planktic B/Ca decreases during the LPEE by ~ 30 $\mu\text{mol/mol}$ in the Pacific (from ~ 80 $\mu\text{mol/mol}$ to ~ 50 $\mu\text{mol/mol}$) and Atlantic (from ~ 68 $\mu\text{mol/mol}$ to ~ 38 $\mu\text{mol/mol}$) (Figure 4.5). *M. velascoensis* and *A. soldadoensis* B/Ca tend to align in the early Eocene (Figure 4.5). At Sites 1209 and 1262, B/Ca in epifaunal benthic foraminifera, *Nuttalides*

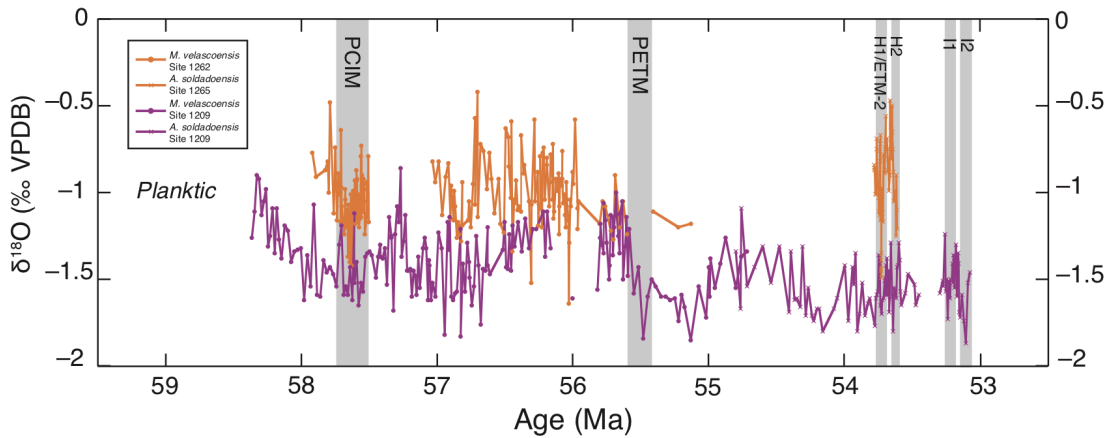


Figure 4.3. Late Paleocene early Eocene planktic foraminifera (*M. velascoensis* and *A. soldadoensis*) $\delta^{18}\text{O}$ data from ODP Sites 1209 and 1262/1265 (this study). Major climate events have been highlighted (gray bars). Plotted against option 1 age model of Westerhold et al. (2008).

truempyi, remains fairly steady over the LPEE while infaunal benthic species, *Oridorsalis umbonatus*, shows a minimal decrease (Figure 4.6). Planktic $\delta^{11}\text{B}$ is highest following the PCIM ~57 Ma and show a steady decline into the early Eocene from ~16.7‰ to ~15.2‰ (Figure 4.5). As documented in Chapter 3, *A. soldadoensis* $\delta^{11}\text{B}$ is offset by -0.2‰ with respect to *M. velascoensis*, likely due to slightly different depth habitats for the two species. When this species offset is accounted for the decline in planktic $\delta^{11}\text{B}$ from Shatsky Rise, in the Pacific, during the LPEE amounts to -1.3‰ .

4.4. Discussion

4.4.1. Response of boron-based proxies

Sea surface pH is calculated from $\delta^{11}\text{B}_{\text{foram}}$ following Hönisch et al. (2019) and the chemistry routines of Zeebe and Wolf-Gladrow (2001). This includes the effects of pressure (i.e., Millero, 1995), temperature, and salinity on equilibrium

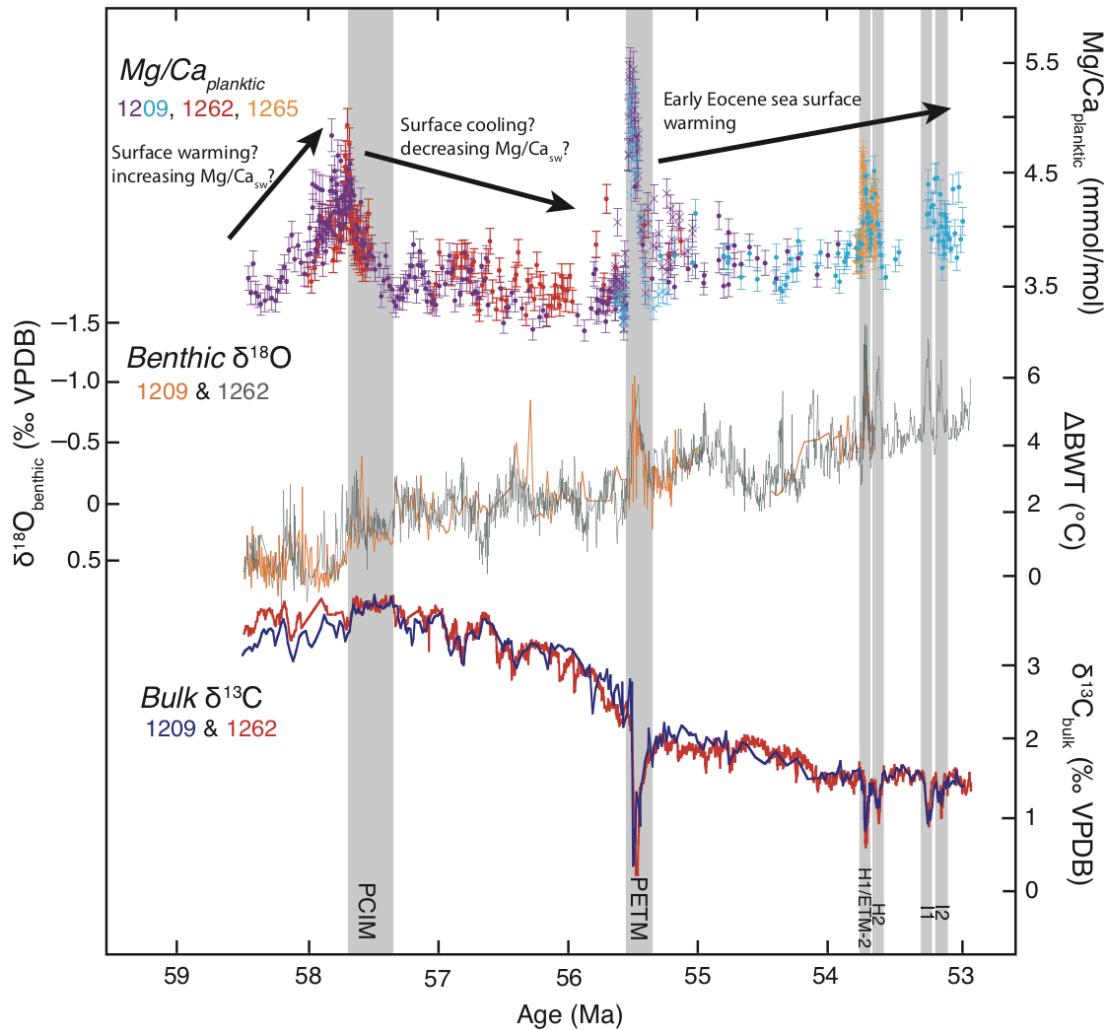


Figure 4.4. Late Paleocene early Eocene planktic Mg/Ca from Shatsky Rise (ODP Site 1209; panel A) and Walvis Ridge (ODP Sites 1262 and 1265 [ETM-2 Mg/Ca only]) with bulk carbonate $\delta^{13}\text{C}$ (this study; Gibbs et al., 2012; Zachos et al., 2001; Littler et al., 2014) and benthic (*N. truempyi*) $\delta^{18}\text{O}$ (this study; McCarren, 2008; Westerhold et al., 2011; McCarren et al., 2008; Stap et al., 2010; Littler et al., 2014). Mg/Ca: red circles = *M. velascoensis* (Site 1262; this study), orange circles = *A. soldadoensis* (Site 1265; Harper et al., 2017), purple circles = *M. velascoensis* (Site 1209; this study), purple Xs = *M. velascoensis* (Site 1209; Penman et al., 2014), blue circles = *A. soldadoensis* (Site 1209; this study and Harper et al., 2017), blue Xs = *A. soldadoensis* (Site 1209; Penman et al., 2014). Plotted against option 1 age model of Westerhold et al. (2008).

constants, but not effects of seawater elemental composition on pK_B^* . To constrain relative uncertainty, computations are made for a range of sea surface salinity (35 ± 2 ppt), and seawater boron isotopic compositions, or $\delta^{11}B_{sw}$ ($38.94\text{‰} \pm 0.41\text{‰}$; i.e., the value applied to PETM pH reconstructions following Gutjahr et al. (2017)). The symbiont-bearing foraminifera multi-species $\delta^{11}B_{calcite}$ versus $\delta^{11}B_{borate}$ sensitivity of Hönisch et al. (2019) is applied (i.e. slope $m = 0.68$) and the species-specific $\delta^{11}B_{foram}$ intercept is calibrated to an initial pH of 8.0 (i.e., $c = 4.8$ for *M. velascoensis* and 4.4 for *A. soldadoensis*; see Hönisch et al., 2019). Data from the main body CIE intervals of the PETM and ETM-2 are excluded. As ΔSST from $Mg/Ca_{planktic}$ is complicated by possible changes in Mg/Ca_{sw} on these timescales (see below for details), SST is held fixed at 30 °C for these calculations (Figure 4.7, black circles and line). Additionally, the sensitivity of the pH record to an imposed long-term warming trend is tested using $\delta^{18}O_{benthic}$ warming from Site 1209 (Figure 4.2) with an initial (58.5 Ma) temperature of 28 °C (Figure 4.7, dashed pink line).

When analytical and calibration uncertainties are propagated, the change in sea surface pH amounts to -0.20 ± 0.20 in the subtropical N. Pacific during the LPEE. If fixed sea surface salinity and $\delta^{11}B_{sw}$ is assumed over the interval (as in Penman et al. (2014)), the sea surface ΔpH is more narrowly constrained to $-0.20 +0.11/-0.08$. Shatsky Rise Sites 1209 and 1210 were located within the North Pacific gyre during the late Paleocene and early Eocene (van Hinsbergen et al., 2015), and thus, likely remained in equilibrium with the atmosphere and experienced little to no circulation

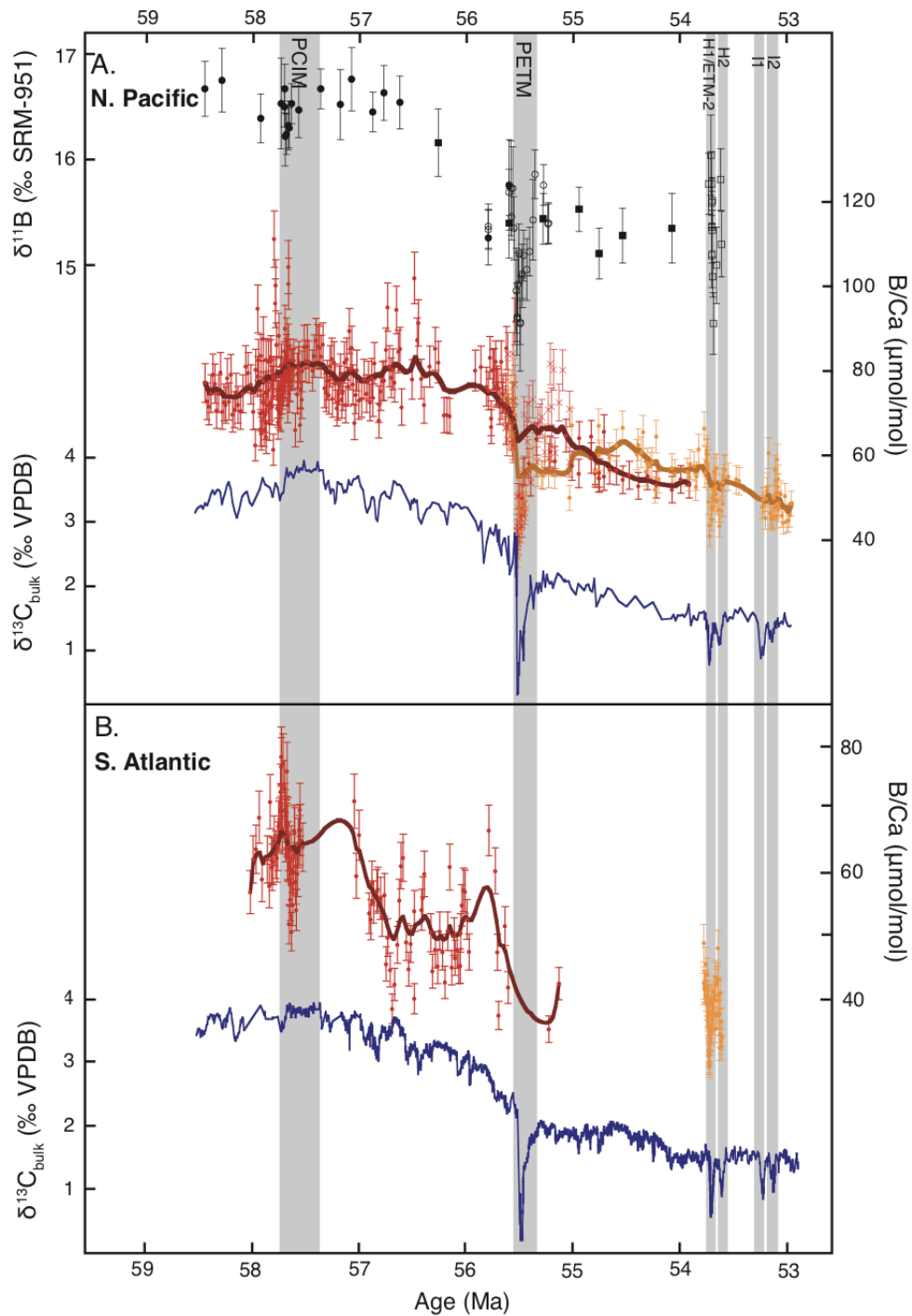


Figure 4.5. Late Paleocene early Eocene boron proxy data from Shatsky Rise (ODP Site 1209; panel A) and Walvis Ridge (ODP Sites 1262 and 1265 [ETM-2 B/Ca only]; panel B) with bulk carbonate $\delta^{13}\text{C}$ (this study; Gibbs et al., 2012; Zachos et al., 2001; Littler et al., 2014). $\delta^{11}\text{B}$: filled black circles = *M. velascensis* (this study), filled black squares = *A. soldadoensis* (this study), open black circles = *M.*

velascoensis (Penman et al., 2014), open black squares = *A. soldadoensis* (Chapter 2). B/Ca: red circles = *M. velascoensis* (this study), red Xs = *M. velascoensis* (Penman et al., 2014), orange circles = *A. soldadoensis* (Chapter 2; this study), orange Xs = *A. soldadoensis* (Penman et al., 2014). B/Ca curve fits: *M. velascoensis* data smoothed curve (dark red line) and *A. soldadoensis* smoothed curve (dark orange line) generated in Kaleidagraph 4.5.2 by applying a Stineman function, the output of which has a geometric weight applied to a given data point and $\pm 10\%$ of the data range. Gray bars indicate major climate events. Plotted against option 1 age model of Westerhold et al. (2008).

induced change in pH over the interval. Therefore, the magnitude of long-term ocean acidification documented here is likely representative of the global decline in sea surface pH during the LPEE.

The long-term decrease in B/Ca_{planktic} during the LPEE at Sites 1209 and 1262 (Figure 4.5), is consistent with sea surface acidification and increasing atmospheric CO_2 , based on the sensitivity of the proxy to changes in sea surface carbonate chemistry (e.g., Haynes et al., 2017). DIC is not computed from B/Ca and pH until parameters such as $\delta^{11}B_{\text{sw}}$ are better constrained for the late Paleocene and additional planktic B/Ca proxy calibrations are generated. However, the records of Pacific and Atlantic planktic B/Ca, place the boron-based proxy records of the PETM (i.e., Babila et al., 2018 and references therein) and ETM-2 (Chapter 3) in the context of long-term sea surface carbonate chemistry variability. That is, the PETM and ETM-2 both display negative pH excursions larger in magnitude than, but comparable to, that observed during the LPEE. Additionally, planktic B/Ca decreases by $\sim 35\%$ in the Pacific and Atlantic during the LPEE, comparable to the decrease established for ETM-2 and the PETM (Chapter 3; Babila et al., 2018). The consistency of long- and

short-term patterns in boron-based proxies are encouraging, suggesting that they are faithfully representing carbonate system parameters.

Further, the LPEE records highlight the relatively large and abrupt nature of the hyperthermal climate and carbon-cycle perturbations, with respect to background climate and carbon cycle variability. Orbital-scale changes in ocean carbonate chemistry are not resolvable using boron-based proxies during the LPEE. The eccentricity-paced variability in $\delta^{13}\text{C}_{\text{benthic}}$ suggests exchanges of carbon between sediment and the atmosphere on the order of ~ 100 ppmv for a carbon source with $\delta^{13}\text{C}$ of -25‰ (i.e., organic carbon) (Zeebe et al., 2017). Thus, it is unlikely that these subtler carbon exchanges would generate changes in ocean carbonate chemistry large enough to be captured by boron-based proxies. This is due in part to the relatively large uncertainty associated with reconstructions of sea surface pH from $\delta^{11}\text{B}_{\text{planktic}}$ (Figure 4.7 and Chapter 3) and DIC from sea surface pH and $\text{B}/\text{Ca}_{\text{planktic}}$ (e.g., Haynes et al., 2017; Chapter 3) during the LPEE.

Brown et al. (2011) proposed that infaunal benthic foraminifera (*O. umbonatus*) may be buffered against changes in bottom water carbonate ion over intervals in which carbonate is continuously deposited, consistent with the species' insensitivity to changes in bottom water carbonate ion concentration in calibration studies. Thus, they suggest the species can be used to deduce changes in seawater B/Ca ($\text{B}/\text{Ca}_{\text{sw}}$), as that is likely the primary control on test B/Ca. The B/Ca in *O. umbonatus* from Sites 1209 and 1262 decreases slightly during the LPEE when PETM samples are omitted (Figure 4.6, panel A), suggesting a slight decrease in

B/Ca_{sw}. However, PETM *O. umbonatus* from Site 1209 show anomalously high B/Ca during the CIE, and when these values are included, little to no long-term change in infaunal benthic B/Ca is observed (Figure 4.6, panel B), suggesting steady B/Ca_{sw}

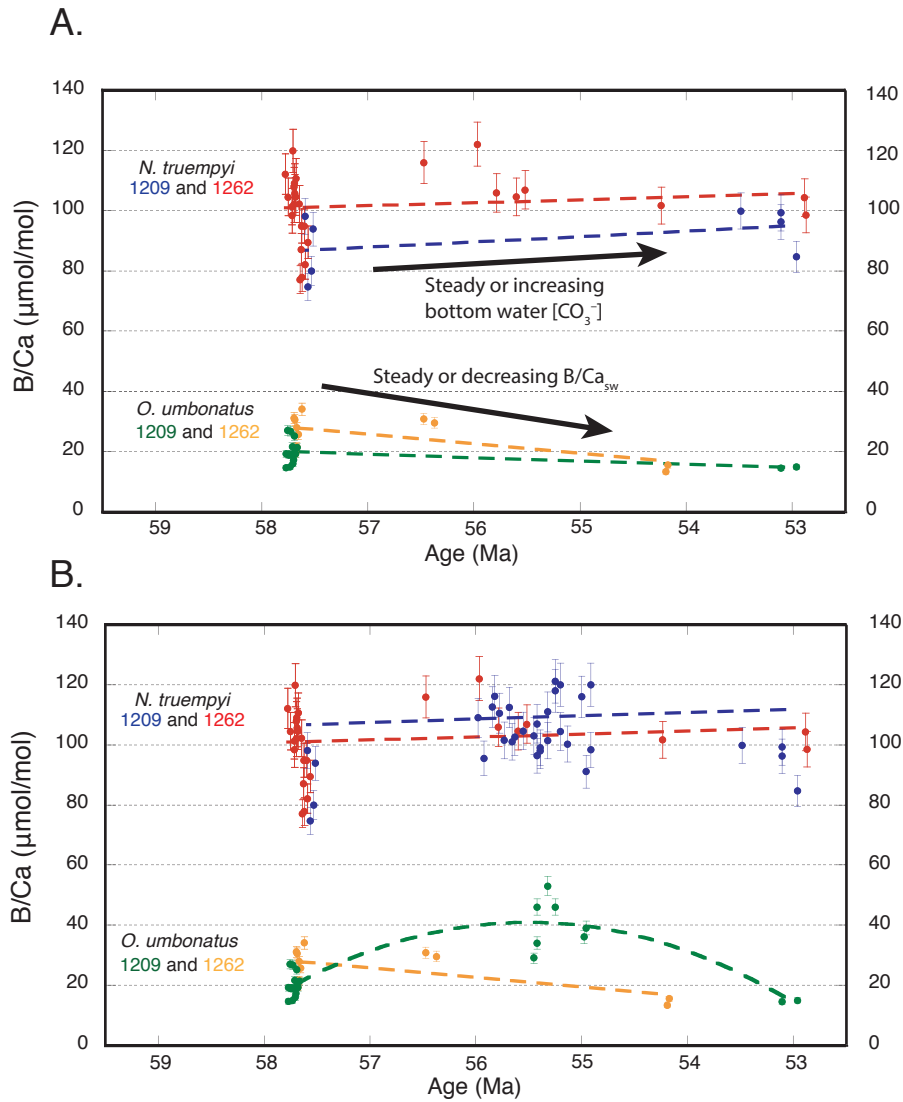


Figure 4.6. Late Paleocene early Eocene benthic B/Ca from ODP Sites 1209 and 1262. Panel A: Excludes PETM data. Panel B: Includes all data. Linear fits are included for each set of data, except Site 1262 *O. umbonatus* (Exponential fit). Plotted versus option 1 age model of Westerhold et al., (2008).

over the LPEE. Epifaunal benthic species, *N. truempyi*, resides at or above the sediment-water interface (Brown et al., 2011), and therefore should be sensitive to changes in bottom water carbonate ion concentration (e.g., Brown et al., 2011; Yu and Elderfield, 2007). However, *N. truempyi* B/Ca is also relatively constant suggesting any changes in carbonate ion saturation over the LPEE were too small to resolve (i.e., the short-term PCIM range in values is equal to the long-term range in values with and without inclusion of 1209 PETM data; Figure 4.6). This observation is somewhat consistent with observations of the CCD (e.g., Hancock et al., 2007; Slotnick et al., 2015), which indicate a small long-term deepening of several hundred meters during the LPEE (i.e., a change in CCD which would likely fall within the error of proxy-based reconstructions of deep water carbonate saturation, given the spread in benthic B/Ca).

4.4.2. Planktic Mg/Ca during the LPEE

We first consider whether the trends in $\text{Mg}/\text{Ca}_{\text{planktic}}$ could be the result of diagenetic overprinting. This seems unlikely for multiple reasons. First, Kozdon et al. (2013) concluded, using nanoSIMS, that the addition of diagenetic calcite to foraminifera shells during post-depositional alteration in a relatively closed system does not significantly differ from the original Mg/Ca, even when dissolution and reprecipitation of secondary diagenetic calcite occurs. This is consistent with the notion that at relatively low water/rock ratios in carbonate rich, closed systems, recrystallization cannot significantly alter the Mg/Ca ratios of the bulk calcite (see Edgar et al., 2015). This hypothesis is confirmed by the similarity of Mg/Ca ratios in

recrystallized and non-recrystallized mixed-layer foraminifera shells from tropical pelagic and shallow marine clay rich sections spanning the P-E boundary (Zachos et al., 2003; Penman et al., 2014; Babila et al., 2018). Third, at Sites 1209 and 1262, there is no evidence of dissolution during the late Paleocene suggesting that both locations lie well above the CCD during the interval, and thus, reprecipitated calcite would likely preserve the original Mg/Ca value over long and short timescales. This is further supported by the close alignment of Mg/Ca_{planktic} for the Pacific and Atlantic, which indicate that changes in Mg/Ca_{planktic} are most likely representative of global signals of temperature change and seawater Mg/Ca chemistry, and therefore not the product of local diagenetic alteration.

While early Eocene Site 1209 and 1262 Mg/Ca_{planktic} are consistent with the long-term warming observed in $\delta^{18}O_{\text{benthic}}$ (i.e., Figure 4.4 and Chapter 3), long-term trends in late Paleocene Mg/Ca_{planktic} (Figure 4.4) are inconsistent with benthic warming (Figure 4.2; 2–5 °C late Paleocene deep water warming) and TEX₈₆-based southwest Pacific SST records of Bijl et al. (2009) (i.e., 3–5 °C late Paleocene sea surface warming). Cramer et al. (2011) similarly observed decreasing benthic Mg/Ca over the late Paleocene coincident with decreasing $\delta^{18}O_{\text{benthic}}$ and suggested that seawater Mg/Ca remained constant thus attributing this discrepancy to changes in global ice volume (i.e., a decrease in ice volume with decreasing bottom water temperature). While there is nominal evidence for Southern hemisphere ice in the late Paleocene (e.g., Hollis et al., 2014), the Mg/Ca-based subtropical surface cooling in both the Pacific and S. Atlantic remains contradictory to melting sea ice (i.e.,

warming). However, long-term (> 1 Myr) records of Mg/Ca may be influenced by changes in seawater Mg/Ca ($\text{Mg}/\text{Ca}_{\text{sw}}$) primarily due to the ~ 1 Myr residence time of Ca in seawater. Indeed, recent work by Evans et al. (2018) indicates that $\text{Mg}/\text{Ca}_{\text{sw}}$ was likely decreasing during the earliest Eocene from the PETM to the EECO, though their records do not extend into the Paleocene. To assess these alternative scenarios, $\text{Mg}/\text{Ca}_{\text{planktic}}$ is first interpreted assuming there is no change in $\text{Mg}/\text{Ca}_{\text{sw}}$ over the interval, and relative changes in sea surface temperature are calculated from planktic Mg/Ca (Figure 4.8). Then, assuming a constant SST, changes in planktic Mg/Ca are interpreted as $\Delta\text{Mg}/\text{Ca}_{\text{sw}}$ (or the change in $\text{Mg}/\text{Ca}_{\text{sw}}$ from the earliest average baseline values) during the late Paleocene (58.5–55.6 Ma; Figure 4.9).

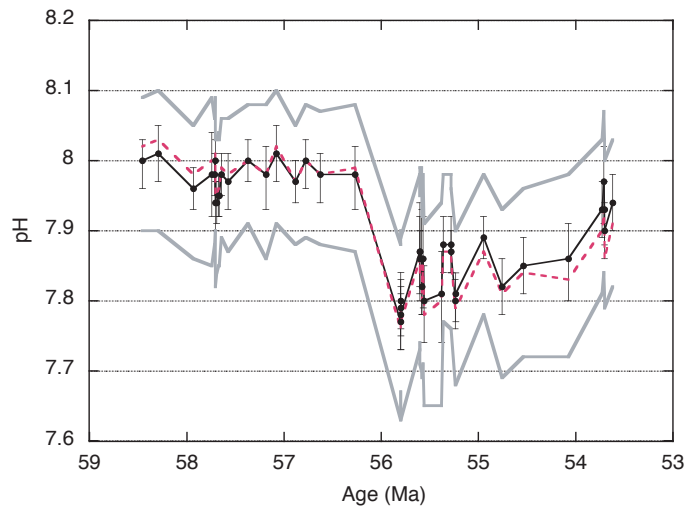


Figure 4.7. Reconstructed pH from ODP Site 1209 during the late Paleocene and early Eocene (LPEE) (see text for details on calculations). Black circles and solid black line plotted with propagated analytical uncertainty (black error bars) = pH calculated at constant 30 °C SST. Dashed pink line = pH calculated using an initial (i.e., 58.5 Ma) sea surface temperature (SST) of 28 °C plus relative warming from long-term benthic $\delta^{18}\text{O}$ (approximated with a linear function) during the LPEE. Gray lines represent propagated analytical uncertainty, and pH calculated with ranges in $\delta^{11}\text{B}$ of seawater ($38.94 \pm 0.41\text{‰}$) and sea surface salinity (35 ± 2 ppt). Plotted versus option 1 age model of Westerhold et al. (2008).

4.4.3. Δ SST from Mg/Ca_{planktic}

Following Zachos et al. (2003), the Δ SST is computed from Mg/Ca_{planktic} by applying a range of pre-exponential constants ('A' value) consistent with earliest Eocene Mg/Ca_{sw} from Evans et al. (2018) and the culturing studies of Evans et al. (2016) (i.e., 0.075 ± 0.005). Where sea surface pH data is available (i.e., Site 1209; Figure 4.7), a pH-adjustment to Mg/Ca_{planktic} is applied following the linear

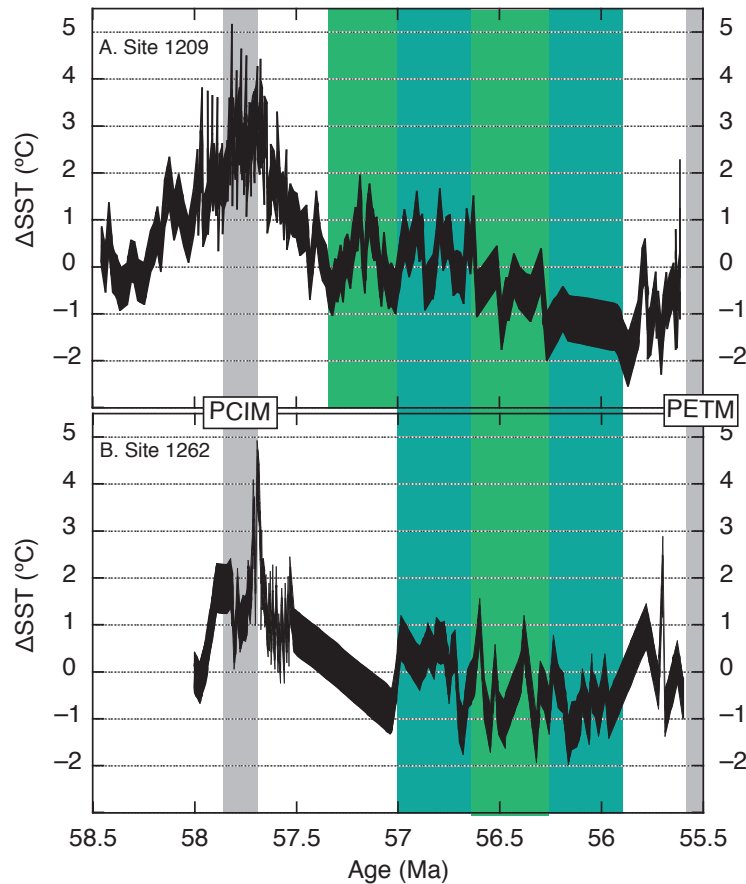


Figure 4.8. Reconstructed late Paleocene sea surface temperature anomalies (Δ SST) from ODP Sites 1209 (panel A) and 1262 (panel B) using planktic (*M. velascoensis*) Mg/Ca assuming no change in Mg/Ca seawater composition. Gray bars indicate climate events. Green and blue bars highlight 400 kyr orbital cycles in the Δ SST data. Plotted against option 1 age model of Westerhold et al. (2008).

relationship of Evans et al. (2016). Sea surface pH data is lacking from the S. Atlantic during this time, and relative changes in pH may be different for the two sites (e.g., Chapter 3). Accordingly, Site 1262 Δ SST is calculated using non-pH-adjusted $\text{Mg}/\text{Ca}_{\text{planktic}}$. Assuming no change in $\text{Mg}/\text{Ca}_{\text{sw}}$, planktic Mg/Ca at both Pacific and Atlantic sites suggests large magnitude subtropical transient sea surface warming (i.e., +1.5 to +4 °C) and peak late Paleocene SSTs during the PCIM (Figure 4.8). The PCIM is typically associated with the coolest $\delta^{18}\text{O}_{\text{benthic}}$ temperatures of the late Paleocene, and the highest $\delta^{13}\text{C}_{\text{benthic}}$ of the entire Paleocene, which could be associated with reduced atmospheric CO_2 though this is not a necessity. Following the ~1 Myr-long transient warming during the PCIM, temperatures remain fairly constant from ~57.3 Ma to the PETM at Site 1262, and decrease at Site 1209 by –1 to –2 °C.

While the long-term records may be influenced by $\Delta\text{Mg}/\text{Ca}_{\text{sw}}$, due to the relatively short residence time of Ca in seawater (i.e., ~1 Ma), short term (< 1 Myr) variations are likely reflecting Δ SST. 400 kyr cycles in Δ SST are observed at Site 1209 (four cycles from 57.4–55.8 Ma) and Site 1262 (three cycles from 57.0–55.8 Ma). The magnitude of warming for each orbital cycle is variable (+0.5 to +2 °C), and scales with orbitally-paced fluctuations in $\delta^{18}\text{O}_{\text{planktic}}$ (Figure 4.3). These results confirm observations of $\delta^{18}\text{O}_{\text{benthic}}$ warming which suggest a similar magnitude (i.e., +1 to +2 °C) of 400 kyr eccentricity-paced warming (Littler et al., 2014), leaving little room for global ice sheet variability within the $\delta^{18}\text{O}_{\text{benthic}}$ signal on these timescales. Additionally, the 400 kyr cycles in $\text{Mg}/\text{Ca}_{\text{planktic}}$ align with $\delta^{18}\text{O}_{\text{benthic}}$ and $\delta^{13}\text{C}_{\text{benthic}}$

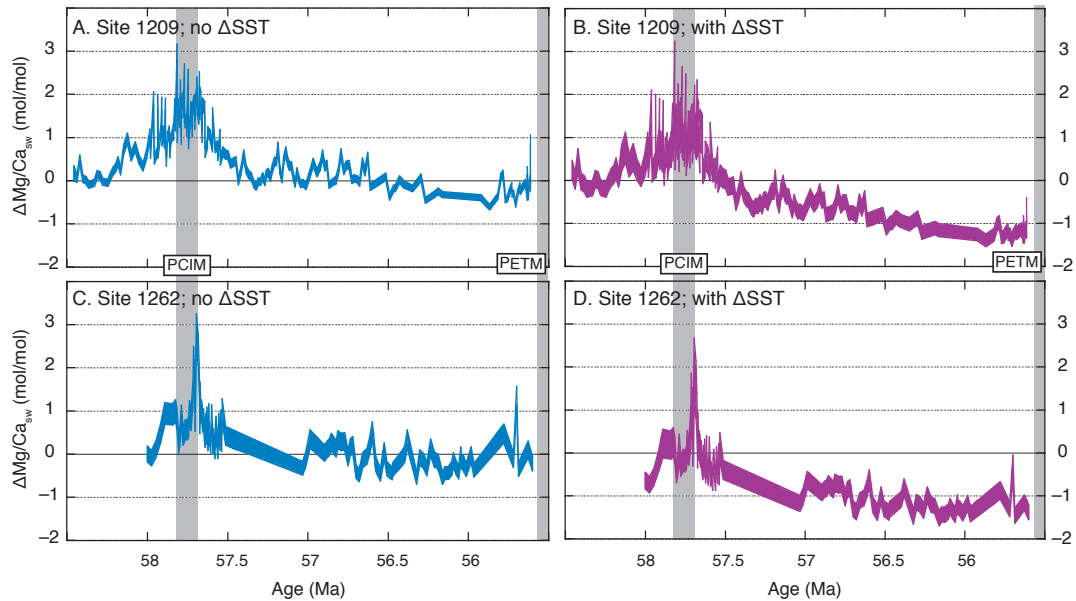


Figure 4.9. Reconstructed late Paleocene anomalies in Mg/Ca seawater composition ($\Delta\text{Mg}/\text{Ca}_{\text{sw}}$) from ODP Sites 1209 and 1262 using planktic (*M. velascoensis*) Mg/Ca assuming no change in sea surface temperature (SST) (panels A and C) and $\delta^{18}\text{O}_{\text{benthic}}$ -based warming (panels B and D). Gray bars highlight two climate events. Plotted against option 1 age model of Westerhold et al. (2008).

eccentricity-paced orbital variability during the late Paleocene at Sites 1209 and 1262, suggesting a close coupling of climate and the carbon cycle on these timescales. As mentioned above, this close coupling may be related to eccentricity-induced changes in climate which trigger positive carbon-cycle feedbacks in reservoirs that are able to exchange carbon with the atmosphere on these timescales. For example, warming/cooling may influence the atmospheric exchange with the marine gas hydrate “capacitor” and/or terrestrial regions of organic carbon deposition sensitive to changes in the hydrologic cycle given observations of, for example, Chapter 2.

4.4.4. $\Delta\text{Mg}/\text{Ca}_{\text{sw}}$ from $\Delta\text{Mg}/\text{Ca}_{\text{planktic}}$ and ΔSST

As the Mg/Ca-based ΔSST records are inconsistent with the long-term records of benthic $\delta^{18}\text{O}$ and $\delta^{13}\text{C}$ over the late Paleocene, it is important to consider the possible influence of $\text{Mg}/\text{Ca}_{\text{sw}}$ on the proxy during this time. Therefore, assuming constant temperature over the interval (Figure 4.9, panels A and C) the $\text{Mg}/\text{Ca}_{\text{planktic}}$ is used to estimate changes in $\text{Mg}/\text{Ca}_{\text{sw}}$. For this, the planktic foraminifera (*Globigerinoides sacculifer*) Mg/Ca versus $\text{Mg}/\text{Ca}_{\text{sw}}$ relationship of Delaney et al. (1985), is used to compute changes in Mg/Ca relative to baseline values (58.5–58.25 Ma for Site 1209 and 58.1–57.9 Ma for Site 1262). Further, because independent SST records do not exist for the late Paleocene at these locations, the $\Delta\text{Mg}/\text{Ca}_{\text{sw}}$ required to reproduce both the observed changes in planktic Mg/Ca and the relative warming observed in $\delta^{18}\text{O}_{\text{benthic}}$ at Sites 1209 and 1262 can be computed (Figure 4.9, panels B and D). This requires use of a temperature proxy calibration, here the $\delta^{18}\text{O}_{\text{benthic}}$ versus temperature relationship of Miller et al., 1987 (i.e., 0.228‰ per °C) is used, assuming the late Paleocene was largely ice-free. A linear fit function of the benthic warming data is applied so that only the $\Delta\text{Mg}/\text{Ca}_{\text{sw}}$ required to reproduce the long-term warming trend be considered (Figure 4.9, panels B and D). The ice-free assumption is bolstered by high-resolution records of Littler et al. (2014) and Westerhold et al. (2011), which show little to no obliquity related power in the orbital scale $\delta^{18}\text{O}_{\text{benthic}}$ records through the Paleocene or early Eocene. Certainly, if a continental ice-sheet was present on Antarctic in the late Paleocene, it would be sensitive to changes in obliquity (i.e., changes in Earth's axial tilt).

Both strategies for $\Delta\text{Mg}/\text{Ca}_{\text{sw}}$ estimation outlined above, require a large increase in $\text{Mg}/\text{Ca}_{\text{sw}}$ during the PCIM (+0.7 to +3.3 mol/mol), followed by a long-term decline over the late Paleocene prior to the PETM (−0.8 to −3.8 mol/mol; Figure 4.9). This observation is in alignment with calculated changes in $\text{Mg}/\text{Ca}_{\text{sw}}$ using coupled $\text{Mg}/\text{Ca}_{\text{benthic}}$ and TEX_{86} data (Evans et al., 2018), which indicate declining $\text{Mg}/\text{Ca}_{\text{sw}}$ in the earliest Eocene. Based on the inconsistencies in high latitude/deep ocean warming (Figure 4.2) with $\text{Mg}/\text{Ca}_{\text{planktic}}$ (Figure 4.4), and the consistencies in subtropical $\text{Mg}/\text{Ca}_{\text{planktic}}$ (i.e., Sites 1209 and 1262 show similar $\text{Mg}/\text{Ca}_{\text{planktic}}$ trends; Figure 4.4), it is likely that $\text{Mg}/\text{Ca}_{\text{sw}}$ did fluctuate during the late Paleocene, possibly as a consequence of increased exchange of Mg for Ca with increasing mid-ocean ridge volcanism in the north Atlantic and elsewhere (e.g., Eldholm and Thomas, 1993; Owen and Rea, 1985). However, until independent proxies of SST are applied to subtropical locations, or reliable records of late Paleocene $\text{Mg}/\text{Ca}_{\text{sw}}$ are established, interpretation of the long-term late Paleocene $\text{Mg}/\text{Ca}_{\text{planktic}}$ record will remain equivocal.

4.4.5. Proxy-model comparison of LPEE carbon cycle and climate

Observations of the CCD (Hancock et al., 2007; Slotnick et al., 2015), surface and deep $\delta^{13}\text{C}$ (Figure 4.1; Littler et al., 2014; Westerhold et al., 2011), deep ocean warming (Littler et al., 2014; Westerhold et al., 2011), high latitude sea surface warming (Bijl et al., 2009) and subtropical N. Pacific sea surface acidification (Figure 4.7) all suggest increasing atmospheric CO_2 over the LPEE. Two potential CO_2 sources on these timescales include 1) North Atlantic Igneous Province (NAIP)

volcanism (e.g., Storey et al., 2007) and 2) a net decrease in the burial of organic carbon globally (i.e., global organic carbon burial – global oxidation of organic carbon deposits; DeConto et al., 2012; Hilting et al., 2008; Komar et al., 2013; Kurtz et al., 2003). Komar et al. (2013) found using a coupled carbon-cycle/climate model (GEOCARB III coupled to LOSCAR; see Berner and Kothavala (2001) and Zeebe (2012), respectively) that the most likely source of carbon during the LPEE was a decrease in the net burial of organic carbon, however they could not rule out a component of volcanic CO₂. This is consistent with previous modeling studies (i.e., Hilting et al., 2008; Kurtz et al., 2003) which also suggest the CO₂ source was associated with a decrease in the net burial of organic carbon.

It has been proposed (Dickens, 2003; Dickens, 2011) that marine gas hydrates may act as a carbon capacitor in which large amounts of ¹³C-depleted carbon can be readily stored and exchanged with the atmosphere over long and short timescales. When this capacitor is included in carbon-cycle climate simulations over the LPEE (i.e., Komar et al., 2013), more subdued fluctuations in the CCD, consistent with observations, are produced (i.e., compare > 1000 m deepening to < 500 m deepening of the CCD in both the Pacific and the Atlantic).

A more modest CCD deepening is supported by B/C_{abenthic} data, which are consistent with a small change in bottom water carbonate ion concentration over the interval (Figure 4.6). However, when the carbon capacitor is included in these

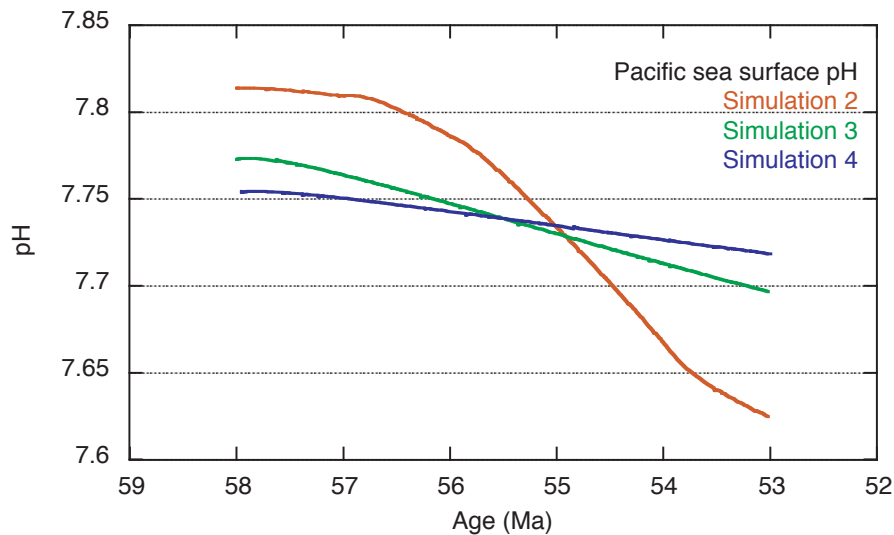


Figure 4.10. Sea surface pH output for the Pacific from Komar et al. (2013). Simulation 2 does not include a gas hydrate capacitor. Simulations 3 and 4 include a gas hydrate capacitor and exchange of carbon from sediments to the ocean occurs as CO_2 (Simulation 3) and HCO_3^- (Simulation 4). See Komar et al. (2013) for additional details regarding each simulation.

simulations, the resulting release of carbon to the atmosphere decreases during the LPEE and warming is subdued (i.e., $< 2^\circ\text{C}$), largely because less of the highly ^{13}C -depleted gas hydrate carbon is required to generate the long-term decrease in surface and deep $\delta^{13}\text{C}$. Additionally, simulations of Komar et al. (2013) which include a gas hydrate capacitor result in little surface pH change in the Pacific and Atlantic (i.e., Figure 4.10; $\Delta\text{pH} < -0.08$ and < -0.04 for simulations 3 and 4, respectively), while simulations that do not include such a capacitor (i.e., Figure 4.10, simulation 2) result in surface pH change in the Pacific and Atlantic of -0.20 pH units, similar to proxy-based results. The authors point out that they do not consider the role of the biological pump during the LPEE. A stronger biological pump (i.e., due to enhanced phosphate

supply from land to the ocean as surface temperatures rise) would tend to dampen the CCD deepening response while maintaining the observed surface to deep $\delta^{13}\text{C}$ gradient. However, a stronger biological pump would likely also dampen the ΔpH signal, though it is unclear to what degree. Thus, while the proxy-based observations support the theory that long-term warming during the LPEE was driven by a net decrease in the burial of organic matter, they do not necessarily support long-term carbon storage and release from a hydrate capacitor.

4.5. Conclusions

This study provides proxy-based long-term (LPEE; ca. 58–52 Ma) context to hyperthermal events, with respect to climate, the carbon cycle, and ocean chemistry, to constrain numerical simulations of climate and the carbon cycle. Boron-based proxies (B/Ca in planktic and benthic foraminifera and $\delta^{11}\text{B}$ in planktic foraminifera), benthic $\delta^{18}\text{O}$, surface and deep $\delta^{13}\text{C}$, and CCD observations indicate long-term CO_2 -induced warming during the LPEE. Mg/Ca_{planktic}-based records of ΔSST from the Pacific and Atlantic contradict observations of deep-sea and high latitude warming (i.e., 4–5 °C) during the LPEE, suggesting changes in Mg/Ca_{sw} during the late Paleocene. However, independent constraints on subtropical sea surface temperatures are needed to appropriately quantify changes in Mg/Ca_{sw}. $\delta^{11}\text{B}_{\text{planktic}}$ suggest a decrease in sea surface pH of -0.20 ± 0.11 to -0.08 during the LPEE, which 1) is most consistent with modeling studies that exclude a dynamic gas hydrate capacitor and 2) supports the theory that a decrease in the net burial of organic carbon was the primary source of CO_2 . Potential landscapes that are sensitive to the weathering/oxidation of

organic carbon, driven by changes in climate and the hydrologic cycle, include peat and permafrost deposits. The magnitude of ocean acidification over the LPEE (and on orbital timescales) was smaller than that of both the PETM and ETM-2, highlighting the uniqueness of the hyperthermal events with respect to background climate and carbon cycle variability and long-term trends.

5. Concluding remarks

This thesis uses geochemical proxies in foraminifera to document changes in global surface temperatures, carbonate chemistry, and the hydrologic cycle during the late Paleocene and early Eocene, with focus on the second largest early Eocene hyperthermal event, ETM-2. Observations produced herein are used to help constrain numerical simulations of carbon release during ETM-2, and demonstrate that a massive release of mixed-source carbon (i.e., 2600 Pg of -37.5‰ C) is required to generate the observed decrease in pH. Sea surface temperatures rose by 1.5–4.0 °C, and subtropical aridity increased during ETM-2, consistent with global circulation models of the hydrologic cycle in a warming world, suggesting enhanced meridional vapor transport. Additionally, this study documents changes in sea surface pH in the subtropical Pacific over longer timescales (i.e., the late Paleocene and early Eocene; LPEE; ca. 58 to 52 Ma), which indicate a similar, but slightly smaller, magnitude pH decrease in the Pacific over the LPEE (-0.20 pH units), with respect to the two largest early Eocene hyperthermals, the PETM (-0.33 pH units) and ETM-2 (-0.26 pH units). Mg/Ca_{planktic} data from subtropical Pacific and Atlantic sites show eccentricity-paced (400 kyr) variability likely reflecting changes in sea surface temperature on these timescales. The data also suggest previously undocumented long-term (i.e., > 1 Myr) changes in Mg/Ca_{sw} during the late Paleocene.

Future work documenting shifts in the hydrologic cycle in the surface ocean and on land are needed to better quantify the global nature of hydrologic cycle change in a warming world. Additional estimates of sea surface pH during ETM-2 and the

LPEE are required to demonstrate the global extent of acidification over these timescales, and constrain scenarios of carbon release. Furthermore, Mg/Ca- and B/Ca-based proxy calibrations using late Paleocene early Eocene seawater chemistry and multiple modern planktic species are needed so that the paleoceanographic community may more precisely estimate past changes in sea surface temperatures and more accurately estimate past DIC. Last, to determine the nature and scale of change in Mg/Ca_{sw} over the late Paleocene suggested by this work, additional Mg/Ca-independent sea surface temperature records from mid to low latitudes are required.

6. References

- Abels, H. A., Clyde, W. C., Gingerich, P. D., Hilgen, F. J., Fricke, H. C., Bowen, G. J., and Lourens, L. J., 2012, Terrestrial carbon isotope excursions and biotic change during Palaeogene hyperthermals: *Nature Geoscience*, v. 5, no. 5, p. 326-329.
- Allen, K. A., and Hönisch, B., 2012, The planktic foraminiferal B/Ca proxy for seawater carbonate chemistry: A critical evaluation: *Earth and Planetary Science Letters*, v. 345-348, p. 203-211.
- Allen, K. A., Hönisch, B., Eggins, S. M., Yu, J., Spero, H. J., and Elderfield, H., 2011, Controls on boron incorporation in cultured tests of the planktic foraminifer *Orbulina universa*: *Earth and Planetary Science Letters*, v. 309, no. 3-4, p. 291-301.
- Anagnostou, E., John, E. H., Edgar, K. M., Foster, G. L., Ridgwell, A., Inglis, G. N., Pancost, R. D., Lunt, D. J., and Pearson, P. N., 2016, Changing atmospheric CO₂ concentration was the primary driver of early Cenozoic climate: *Nature*, v. 533, no. 7603, p. 380-384.
- Anand, P., Elderfield, H., and Conte, M. H., 2003, Calibration of Mg/Ca thermometry in planktonic foraminifera from a sediment trap time series: *Paleoceanography*, v. 18, no. 2.
- Babila, T. L., Penman, D. E., Honisch, B., Kelly, D. C., Bralower, T. J., Rosenthal, Y., and Zachos, J. C., 2018, Capturing the global signature of surface ocean acidification during the Palaeocene-Eocene Thermal Maximum: *Philos Trans A Math Phys Eng Sci*, v. 376, no. 2130.
- Babila, T. L., Rosenthal, Y., and Conte, M. H., 2014, Evaluation of the biogeochemical controls on B/Ca of *Globigerinoides ruber* white from the Oceanic Flux Program, Bermuda: *Earth and Planetary Science Letters*, v. 404, p. 67-76.
- Babila, T. L., Rosenthal, Y., Wright, J. D., and Miller, K. G., 2016, A continental shelf perspective of ocean acidification and temperature evolution during the Paleocene-Eocene Thermal Maximum: *Geology*, v. 44, no. 4, p. 275-278.
- Baczynski, A. A., McInerney, F. A., Wing, S. L., Kraus, M. J., Bloch, J. I., and Secord, R., 2017, Constraining paleohydrologic change during the Paleocene-Eocene Thermal Maximum in the continental interior of North America: *Palaeogeography, Palaeoclimatology, Palaeoecology*, v. 465, p. 237-246.

- Barker, S., Greaves, M., and Elderfield, H., 2003, A study of cleaning procedures used for foraminiferal Mg/Ca paleothermometry: *Geochemistry, Geophysics, Geosystems*, v. 4, no. 9, p. 20.
- Bartoli, G., Hönisch, B., and Zeebe, R. E., 2011, Atmospheric CO₂ decline during the Pliocene intensification of Northern Hemisphere glaciations: *Paleoceanography*, v. 26, no. 4, p. 14.
- Berner, R. A., and Kothavala, Z., 2001, Geocarb III: A revised model of atmospheric CO₂ over Phanerozoic time: *American Journal of Science*, v. 301, p. 22.
- Bijl, P. K., Schouten, S., Sluijs, A., Reichert, G. J., Zachos, J. C., and Brinkhuis, H., 2009, Early Palaeogene temperature evolution of the southwest Pacific Ocean: *Nature*, v. 461, no. 7265, p. 776-779.
- Bohaty, S. M., Zachos, J. C., and Delaney, M. L., 2012, Foraminiferal Mg/Ca evidence for Southern Ocean cooling across the Eocene–Oligocene transition: *Earth and Planetary Science Letters*, v. 317-318, p. 251-261.
- Bralower, T. J., Premoli-Silva, I., Malone, M. J., and Party, L. S. S., 2002, *Proceedings of the Ocean Drilling Program, Initial Reports, Vol. 198: Ocean Drilling Program*.
- Broecker, W. S., and Peng, T.-H., 1982, *Tracers in the Sea*, Eldigio Press.
- Brown, R. E., Anderson, L. D., Thomas, E., and Zachos, J. C., 2011, A core-top calibration of B/Ca in the benthic foraminifers *Nuttallides umbonifera* and *Oridorsalis umbonatus*: A proxy for Cenozoic bottom water carbonate saturation: *Earth and Planetary Science Letters*, v. 310, no. 3-4, p. 360-368.
- Carmichael, M. J., Lunt, D. J., Huber, M., Heinemann, M., Kiehl, J., LeGrande, A., Loptson, C. A., Roberts, C. D., Sahoo, N., Shields, C., Valdes, P. J., Winguth, A., Winguth, C., and Pancost, R. D., 2015, Insights into the early Eocene hydrological cycle from an ensemble of atmosphere–ocean GCM simulations: *Climate of the Past Discussions*, v. 11, no. 4, p. 3277-3339.
- Chalk, T. B., Hain, M. P., Foster, G. L., Rohling, E. J., Sexton, P. F., Badger, M. P. S., Cherry, S. G., Hasenfratz, A. P., Haug, G. H., Jaccard, S. L., Martinez-Garcia, A., Palike, H., Pancost, R. D., and Wilson, P. A., 2017, Causes of ice age intensification across the Mid-Pleistocene Transition: *Proc Natl Acad Sci U S A*, v. 114, no. 50, p. 13114-13119.
- Colosimo, A. B., Bralower, T. J., and Zachos, J. C., 2006, Evidence for Lysocline Shoaling at the Paleocene/Eocene Thermal Maximum on Shatsky Rise,

Northwest Pacific: Proceedings of the Ocean Drilling Program, Scientific Results, v. 198.

- Cramer, B. S., Miller, K. G., Barrett, P. J., and Wright, J. D., 2011, Late Cretaceous–Neogene trends in deep ocean temperature and continental ice volume: Reconciling records of benthic foraminiferal geochemistry ($\delta^{18}\text{O}$ and Mg/Ca) with sea level history: *Journal of Geophysical Research*, v. 116, no. C12.
- Cui, Y., Kump, L. R., Ridgwell, A. J., Charles, A. J., Junium, C. K., Diefendorf, A. F., Freeman, K. H., Urban, N. M., and Harding, I. C., 2011, Slow release of fossil carbon during the Palaeocene–Eocene Thermal Maximum: *Nature Geoscience*, v. 4, no. 7, p. 481-485.
- D'Hondt, S., Zachos, J. C., and Schultz, G., 1994, Stable Isotope Signals and Photosymbiosis in Late Paleocene Planktic Foraminifera: *Paleobiology*, v. 20, no. 3, p. 16.
- DeConto, R. M., Galeotti, S., Pagani, M., Tracy, D., Schaefer, K., Zhang, T., Pollard, D., and Beerling, D. J., 2012, Past extreme warming events linked to massive carbon release from thawing permafrost: *Nature*, v. 484, no. 7392, p. 87-91.
- Dekens, P. S., Lea, D. W., Pak, D. K., and Spero, H. J., 2002, Core top calibration of Mg/Ca in tropical foraminifera: Refining paleotemperature estimation: *Geochemistry, Geophysics, Geosystems*, v. 3, no. 4, p. 1-29.
- Delaney, M. L., Bè, A. W. H., and Boyle, E. A., 1985, Li, Sr, Mg, and Na in foraminiferal calcite shells from laboratory culture, sediment traps, and sediment cores: *Geochimica et Cosmochimica Acta*, v. 49, p. 14.
- Dickens, G. R., 2003, Rethinking the global carbon cycle with a large, dynamic and microbially mediated gas hydrate capacitor: *Earth and Planetary Science Letters*, v. 213, no. 3-4, p. 169-183.
- Dickens, G. R., 2011, Down the Rabbit Hole: toward appropriate discussion of methane release from gas hydrate systems during the Paleocene-Eocene thermal maximum and other past hyperthermal events: *Climate of the Past*, v. 7, no. 3, p. 831-846.
- Dickens, G. R., Castillo, M. M., and Walker, J. C. G., 1997, A blast of gas in the latest Paleocene: Simulating first-order effects of massive dissociation of oceanic methane hydrate: *Geology*, v. 25, no. 3.
- Dunkley Jones, T., Lunt, D. J., Schmidt, D. N., Ridgwell, A., Sluijs, A., Valdes, P. J., and Maslin, M., 2013, Climate model and proxy data constraints on ocean

- warming across the Paleocene–Eocene Thermal Maximum: *Earth-Science Reviews*, v. 125, p. 123-145.
- Dutton, A., Lohmann, K. C., and Leckie, R. M., 2005, Insights from the Paleogene tropical Pacific: Foraminiferal stable isotope and elemental results from Site 1209, Shatsky Rise: *Paleoceanography*, v. 20, no. 3, p. 16.
- Edgar, K. M., Anagnostou, E., Pearson, P. N., and Foster, G. L., 2015, Assessing the impact of diagenesis on $\delta^{11}\text{B}$, $\delta^{13}\text{C}$, $\delta^{18}\text{O}$, Sr/Ca and B/Ca values in fossil planktic foraminiferal calcite: *Geochimica et Cosmochimica Acta*, v. 166, p. 189-209.
- Eldholm, O., and Thomas, E., 1993, Environmental impacts of volcanic margin formation: *Earth and Planetary Science Letters*, v. 117, p. 10.
- Evans, D., and Müller, W., 2012, Deep time foraminifera Mg/Ca paleothermometry: Nonlinear correction for secular change in seawater Mg/Ca: *Paleoceanography*, v. 27, no. 4.
- Evans, D., Sagoo, N., Renema, W., Cotton, L. J., Muller, W., Todd, J. A., Saraswati, P. K., Stassen, P., Ziegler, M., Pearson, P. N., Valdes, P. J., and Affek, H. P., 2018, Eocene greenhouse climate revealed by coupled clumped isotope-Mg/Ca thermometry: *Proc Natl Acad Sci U S A*, v. 115, no. 6, p. 1174-1179.
- Evans, D., Wade, B. S., Henahan, M., Erez, J., and Müller, W., 2016, Revisiting carbonate chemistry controls on planktic foraminifera Mg / Ca: implications for sea surface temperature and hydrology shifts over the Paleocene–Eocene Thermal Maximum and Eocene–Oligocene transition: *Climate of the Past*, v. 12, no. 4, p. 819-835.
- Foreman, B. Z., Heller, P. L., and Clementz, M. T., 2012, Fluvial response to abrupt global warming at the Palaeocene/Eocene boundary: *Nature*, v. 491, no. 7422, p. 92-95.
- Foster, G. L., 2008, Seawater pH, pCO₂ and [CO₂–3] variations in the Caribbean Sea over the last 130 kyr: A boron isotope and B/Ca study of planktic foraminifera: *Earth and Planetary Science Letters*, v. 271, no. 1-4, p. 254-266.
- Foster, G. L., Hönisch, B., Paris, G., Dwyer, G. S., Rae, J. W. B., Elliott, T., Gaillardet, J., Hemming, N. G., Louvat, P., and Vengosh, A., 2013, Interlaboratory comparison of boron isotope analyses of boric acid, seawater and marine CaCO₃ by MC-ICPMS and NTIMS: *Chemical Geology*, v. 358, p. 1-14.

- Frieling, J., Reichart, G.-J., Middelburg, J. J., Röhl, U., Westerhold, T., Bohaty, S. M., and Sluijs, A., 2018, Tropical Atlantic climate and ecosystem regime shifts during the Paleocene–Eocene Thermal Maximum: *Climate of the Past*, v. 14, no. 1, p. 39-55.
- Gibbs, S. J., Bown, P. R., Murphy, B. H., Sluijs, A., Edgar, K. M., Pälike, H., Bolton, C. T., and Zachos, J. C., 2012, Scaled biotic disruption during early Eocene global warming events: *Biogeosciences*, v. 9, no. 11, p. 4679-4688.
- Gutjahr, M., Ridgwell, A., Sexton, P. F., Anagnostou, E., Pearson, P. N., Pälike, H., Norris, R. D., Thomas, E., and Foster, G. L., 2017, Very large release of mostly volcanic carbon during the Palaeocene-Eocene Thermal Maximum: *Nature*, v. 548, no. 7669, p. 573-577.
- Hancock, H. J. L., Dickens, G. R., Thomas, E., and Blake, K. L., 2007, Reappraisal of early Paleogene CCD curves: foraminiferal assemblages and stable carbon isotopes across the carbonate facies of Perth Abyssal Plain: *International Journal of Earth Sciences*, v. 96, no. 5, p. 925-946.
- Harper, D. T., Zeebe, R., Hönisch, B., Schrader, C. D., Lourens, L. J., and Zachos, J. C., 2017, Subtropical sea-surface warming and increased salinity during Eocene Thermal Maximum 2: *Geology*, v. 46, no. 2, p. 187-190.
- Haynes, L. L., Hönisch, B., Dyez, K. A., Holland, K., Rosenthal, Y., Fish, C. R., Subhas, A. V., and Rae, J. B., 2017, Calibration of the B/Ca proxy in the planktic foraminifer *Orbulina universa* to Paleocene seawater conditions: *Paleoceanography*, v. 32, no. 6, p. 580-599.
- Henehan, M. J., Foster, G. L., Rae, J. W. B., Prentice, K. C., Erez, J., Bostock, H. C., Marshall, B. J., and Wilson, P. A., 2015, Evaluating the utility of B/Ca ratios in planktic foraminifera as a proxy for the carbonate system: A case study of *Globigerinoides ruber*: *Geochemistry, Geophysics, Geosystems*, v. 16, no. 4, p. 1052-1069.
- Hilting, A. K., Kump, L. R., and Bralower, T. J., 2008, Variations in the oceanic vertical carbon isotope gradient and their implications for the Paleocene-Eocene biological pump: *Paleoceanography*, v. 23, no. 3.
- Hollis, C. J., Tayler, M. J. S., Andrew, B., Taylor, K. W., Lurcock, P., Bijl, P. K., Kulhanek, D. K., Crouch, E. M., Nelson, C. S., Pancost, R. D., Huber, M., Wilson, G. S., Ventura, G. T., Crampton, J. S., Schiøler, P., and Phillips, A., 2014, Organic-rich sedimentation in the South Pacific Ocean associated with Late Paleocene climatic cooling: *Earth-Science Reviews*, v. 134, p. 81-97.

- Hönisch, B., Allen, K. A., Lea, D. W., Spero, H. J., Eggins, S. M., Arbuszewski, J., deMenocal, P., Rosenthal, Y., Russell, A. D., and Elderfield, H., 2013, The influence of salinity on Mg/Ca in planktic foraminifers – Evidence from cultures, core-top sediments and complementary $\delta^{18}\text{O}$: *Geochimica et Cosmochimica Acta*, v. 121, p. 196-213.
- Hönisch, B., Bijma, J., Russell, A. D., Spero, H. J., Palmer, M. R., Zeebe, R. E., and Eisenhauer, A., 2003, The influence of symbiont photosynthesis on the boron isotopic composition of foraminifera shells: *Marine Micropaleontology*, v. 49, no. 1-2, p. 87-96.
- Hönisch, B., and Hemming, N. G., 2004, Ground-truthing the boron isotope-paleo-pH proxy in planktonic foraminifera shells: Partial dissolution and shell size effects: *Paleoceanography*, v. 19.
- Hönisch, B., Hemming, N. G., Archer, D., Siddall, M., and McManus, J. F., 2009, Atmospheric carbon dioxide concentration across the mid-Pleistocene transition: *Science*, v. 324, no. 5934, p. 1551-1554.
- Hönisch, B. r., Eggins, S. M., Haynes, L. L., Allen, K. A., Holland, K., and Lorbacher, K., 2019, *Boron Proxies in Paleoceanography and Paleoclimatology*, John Wiley & Sons Ltd.
- Howes, E. L., Kaczmarek, K., Raitzsch, M., Mewes, A., Bijma, N., Horn, I., Misra, S., Gattuso, J.-P., and Bijma, J., 2017, Decoupled carbonate chemistry controls on the incorporation of boron into *Orbulina universa*: *Biogeosciences*, v. 14, no. 2, p. 415-430.
- Jennions, S. M., Thomas, E., Schmidt, D. N., Lunt, D., and Ridgwell, A., 2015, Changes in benthic ecosystems and ocean circulation in the Southeast Atlantic across Eocene Thermal Maximum 2: *Paleoceanography*, v. 30, no. 8, p. 1059-1077.
- Kennett, J. P., and Stott, L. D., 1991, Abrupt deep-sea warming, palaeoceanographic changes and benthic extinctions at the end of the Palaeocene: *Nature*, v. 353.
- Kiehl, J. T., and Shields, C. A., 2013, Sensitivity of the Palaeocene-Eocene Thermal Maximum climate to cloud properties: *Philos Trans A Math Phys Eng Sci*, v. 371, no. 2001, p. 20130093.
- Kirtland Turner, S., and Ridgwell, A., 2016, Development of a novel empirical framework for interpreting geological carbon isotope excursions, with implications for the rate of carbon injection across the PETM: *Earth and Planetary Science Letters*, v. 435, p. 1-13.

- Klochko, K., Kaufman, A. J., Yao, W., Byrne, R. H., and Tossell, J. A., 2006, Experimental measurement of boron isotope fractionation in seawater: *Earth and Planetary Science Letters*, v. 248, no. 1-2, p. 276-285.
- Koch, P. L., Zachos, J. C., and Gingerich, P. D., 1992, Correlation between isotope records in marine and continental carbon reservoirs near the Palaeocene/Eocene boundary: *Nature*, v. 358.
- Komar, N., Zeebe, R. E., and Dickens, G. R., 2013, Understanding long-term carbon cycle trends: The late Paleocene through the early Eocene: *Paleoceanography*, v. 28, no. 4, p. 650-662.
- Kozdon, R., Kelly, D. C., Kitajima, K., Strickland, A., Fournelle, J. H., and Valley, J. W., 2013, In situ $\delta^{18}\text{O}$ and Mg/Ca analyses of diagenetic and planktic foraminiferal calcite preserved in a deep-sea record of the Paleocene-Eocene thermal maximum: *Paleoceanography*, v. 28, no. 3, p. 517-528.
- Kraus, M. J., and Riggins, S., 2007, Transient drying during the Paleocene–Eocene Thermal Maximum (PETM): Analysis of paleosols in the bighorn basin, Wyoming: *Palaeogeography, Palaeoclimatology, Palaeoecology*, v. 245, no. 3-4, p. 444-461.
- Kucera, M., Malmgren, B. A., and Stouresson, U., 1997, Foraminiferal dissolution at the shallow depths of the Walvis Ridge and Rio Grande Rise during the latest Cretaceous: Inferences for deep-water circulation in the South Atlantic: *Palaeogeography, Palaeoclimatology, Palaeoecology*, v. 129, p. 18.
- Kurtz, A. C., Kump, L. R., Arthur, M. A., Zachos, J. C., and Paytan, A., 2003, Early Cenozoic decoupling of the global carbon and sulfur cycles: *Paleoceanography*, v. 18, no. 4.
- Lauretano, V., Hilgen, F. J., Zachos, J. C., and Lourens, L. J., 2016, Astronomically tuned age model for the early Eocene carbon isotope events: A new high-resolution $\delta^{13}\text{C}$ benthic record of ODP Site 1263 between ~ 49 and ~ 54 Ma: *Newsletters on Stratigraphy*, v. 49, no. 2, p. 383-400.
- Littler, K., Röhl, U., Westerhold, T., and Zachos, J. C., 2014, A high-resolution benthic stable-isotope record for the South Atlantic: Implications for orbital-scale changes in Late Paleocene–Early Eocene climate and carbon cycling: *Earth and Planetary Science Letters*, v. 401, p. 18-30.
- Lourens, L. J., Sluijs, A., Kroon, D., Zachos, J. C., Thomas, E., Röhl, U., Bowles, J., and Raffi, I., 2005, Astronomical pacing of late Palaeocene to early Eocene global warming events: *Nature*, v. 435, no. 7045, p. 1083-1087.

- Lunt, D. J., Ridgwell, A., Sluijs, A., Zachos, J., Hunter, S., and Haywood, A., 2011, A model for orbital pacing of methane hydrate destabilization during the Palaeogene: *Nature Geoscience*, v. 4, no. 11, p. 775-778.
- Martin, P. A., and Lea, D. W., 2002, A simple evaluation of cleaning procedures on fossil benthic foraminiferal Mg/Ca: *Geochemistry, Geophysics, Geosystems*, v. 3, no. 10, p. 1-8.
- Matsumoto, K., 2007, Biology-mediated temperature control on atmospheric pCO₂ and ocean biogeochemistry: *Geophysical Research Letters*, v. 34, no. 20.
- Matthews, K. J., Maloney, K. T., Zahirovic, S., Williams, S. E., Seton, M., and Müller, R. D., 2016, Global plate boundary evolution and kinematics since the late Paleozoic: *Global and Planetary Change*, v. 146, p. 226-250.
- McCarren, H., Thomas, E., Hasegawa, T., Röhl, U., and Zachos, J. C., 2008, Depth dependency of the Paleocene-Eocene carbon isotope excursion: Paired benthic and terrestrial biomarker records (Ocean Drilling Program Leg 208, Walvis Ridge): *Geochemistry, Geophysics, Geosystems*, v. 9, no. 10, p. n/a-n/a.
- McCarren, H. K., 2009, Paleooceanographic variability of extreme climates in the early Paleogene [Ph.D.: University of California, Santa Cruz, 196 p.
- McInerney, F. A., and Wing, S. L., 2011, The Paleocene-Eocene Thermal Maximum: A Perturbation of Carbon Cycle, Climate, and Biosphere with Implications for the Future: *Annual Review of Earth and Planetary Sciences*, v. 39, no. 1, p. 489-516.
- Miller, K. G., Janecek, T. R., Katz, M. E., and Keil, D. J., 1987, Abyssal circulation and benthic foraminiferal changes near the Paleocene/Eocene boundary: *Paleoceanography*, v. 2, no. 6, p. 20.
- Millero, F. J., 1995, Thermodynamics of the carbon dioxide system in the oceans: *Geochimica et Cosmochimica Acta*, v. 59, no. 4, p. 16.
- Nicolo, M. J., Dickens, G. R., Hollis, C. J., and Zachos, J. C., 2007, Multiple early Eocene hyperthermals: Their sedimentary expression on the New Zealand continental margin and in the deep sea: *Geology*, v. 35, no. 8.
- Owen, R. M., and Rea, D. K., 1985, Sea-floor hydrothermal activity links climate to tectonics: The Eocene carbon dioxide greenhouse: *Science*, v. 227, no. 4683, p. 3.
- PALAEOSENS, P. M., 2012, Making sense of palaeoclimate sensitivity: *Nature*, v. 491, no. 7426, p. 683-691.

- Panchuk, K., Ridgwell, A., and Kump, L. R., 2008, Sedimentary response to Paleocene-Eocene Thermal Maximum carbon release: A model-data comparison: *Geology*, v. 36, no. 4.
- Pearson, P. N., van Dongen, B. E., Nicholas, C. J., Pancost, R. D., Schouten, S., Singano, J. M., and Wade, B. S., 2007, Stable warm tropical climate through the Eocene Epoch: *Geology*, v. 35, no. 3.
- Penman, D. E., Hönlisch, B., Zeebe, R. E., Thomas, E., and Zachos, J. C., 2014, Rapid and sustained surface ocean acidification during the Paleocene-Eocene Thermal Maximum: *Paleoceanography*, v. 29, no. 5, p. 357-369.
- Roberts, C. D., LeGrande, A. N., and Tripathi, A. K., 2011, Sensitivity of seawater oxygen isotopes to climatic and tectonic boundary conditions in an early Paleogene simulation with GISS ModelE-R: *Paleoceanography*, v. 26, no. 4.
- Röhl, U., Westerhold, T., Bralower, T. J., and Zachos, J. C., 2007, On the duration of the Paleocene-Eocene thermal maximum (PETM): *Geochemistry, Geophysics, Geosystems*, v. 8, no. 12.
- Royer, D. L., 2014, Atmospheric CO₂ and O₂ during the Phanerozoic: Tools, patterns, and impacts: *Treatise on Geochemistry (Second Edition)*, v. 6.
- Salmon, K. H., Anand, P., Sexton, P. F., and Conte, M., 2016, Calcification and growth processes in planktonic foraminifera complicate the use of B/Ca and U/Ca as carbonate chemistry proxies: *Earth and Planetary Science Letters*, v. 449, p. 372-381.
- Schmitz, B., and Pujalte, V., 2007, Abrupt increase in seasonal extreme precipitation at the Paleocene-Eocene boundary: *Geology*, v. 35, no. 3.
- Schrag, D. P., DePaolo, D. J., and Richter, F. M., 1995, Reconstructing past sea surface temperatures: Correcting for diagenesis of bulk marine carbonate: *Geochimica et Cosmochimica Acta*, v. 59, no. 11, p. 13.
- Slotnick, B. S., Lauretano, V., Backman, J., Dickens, G. R., Sluijs, A., and Lourens, L., 2015, Early Paleogene variations in the calcite compensation depth: new constraints using old borehole sediments from across Ninetyeast Ridge, central Indian Ocean: *Climate of the Past*, v. 11, no. 3, p. 473-493.
- Sluijs, A., Brinkhuis, H., Schouten, S., Bohaty, S. M., John, C. M., Zachos, J. C., Reichart, G. J., Sinninghe Damste, J. S., Crouch, E. M., and Dickens, G. R., 2007, Environmental precursors to rapid light carbon injection at the Palaeocene/Eocene boundary: *Nature*, v. 450, no. 7173, p. 1218-1221.

- Sluijs, A., Schouten, S., Donders, T. H., Schoon, P. L., Röhl, U., Reichart, G. J., Sangiorgi, F., Kim, J. H., Sinninghe Damste, J. S., and Brinkhuis, H., 2009, Warm and wet conditions in the Arctic region during Eocene Thermal Maximum 2: *Nature Geoscience*, v. 2.
- Spero, H. J., Bijma, J., Lea, D. W., and Bemis, B. E., 1997, Effect of seawater carbonate concentration on foraminiferal carbon and oxygen isotopes: *Nature*, v. 390, p. 4.
- Spero, H. J., and Lea, D. W., 1996, Experimental determination of stable isotope variability in *Globigerina bulloides*: implications for paleoceanographic reconstructions: *Marine Micropaleontology*, v. 28, p. 15.
- Stap, L., Lourens, L., van Dijk, A., Schouten, S., and Thomas, E., 2010a, Coherent pattern and timing of the carbon isotope excursion and warming during Eocene Thermal Maximum 2 as recorded in planktic and benthic foraminifera: *Geochemistry, Geophysics, Geosystems*, v. 11, no. 11, p. n/a-n/a.
- Stap, L., Lourens, L. J., Thomas, E., Sluijs, A., Bohaty, S., and Zachos, J. C., 2010b, High-resolution deep-sea carbon and oxygen isotope records of Eocene Thermal Maximum 2 and H2: *Geology*, v. 38, no. 7, p. 607-610.
- Stap, L., Sluijs, A., Thomas, E., and Lourens, L., 2009, Patterns and magnitude of deep sea carbonate dissolution during Eocene Thermal Maximum 2 and H2, Walvis Ridge, southeastern Atlantic Ocean: *Paleoceanography*, v. 24, no. 1.
- Storey, M., Duncan, R. A., and Tegner, C., 2007, Timing and duration of volcanism in the North Atlantic Igneous Province: Implications for geodynamics and links to the Iceland hotspot: *Chemical Geology*, v. 241, no. 3-4, p. 264-281.
- Svensen, H., Planke, S., Malthe-Sorensen, A., Jamtveit, B., Myklebust, R., Eidem, T. R., and Rey, S. S., 2004, Release of methane from a volcanic basin as a mechanism for initial Eocene global warming: *Nature*, v. 429, no. 6991, p. 4.
- Takeda, K., and Kaiho, K., 2007, Faunal turnovers in central Pacific benthic foraminifera during the Paleocene–Eocene thermal maximum: *Palaeogeography, Palaeoclimatology, Palaeoecology*, v. 251, no. 2, p. 175-197.
- Thomas, E., and Shackleton, N. J., 1996, The Paleocene-Eocene benthic foraminiferal extinction and stable isotope anomalies: Geological Society, London, Special Publications, v. 101, no. 1, p. 401-441.
- Tindall, J., Flecker, R., Valdes, P., Schmidt, D. N., Markwick, P., and Harris, J., 2010, Modelling the oxygen isotope distribution of ancient seawater using a

- coupled ocean–atmosphere GCM: Implications for reconstructing early Eocene climate: *Earth and Planetary Science Letters*, v. 292, no. 3-4, p. 265-273.
- Tipple, B. J., Pagani, M., Krishnan, S., Dirghangi, S. S., Galeotti, S., Agnini, C., Giusberti, L., and Rio, D., 2011, Coupled high-resolution marine and terrestrial records of carbon and hydrologic cycles variations during the Paleocene–Eocene Thermal Maximum (PETM): *Earth and Planetary Science Letters*, v. 311, no. 1-2, p. 82-92.
- Tripati, A. K., and Elderfield, H., 2004, Abrupt hydrographic changes in the equatorial Pacific and subtropical Atlantic from foraminiferal Mg/Ca indicate greenhouse origin for the thermal maximum at the Paleocene-Eocene Boundary: *Geochemistry, Geophysics, Geosystems*, v. 5, no. 2, p. n/a-n/a.
- van Hinsbergen, D. J., de Groot, L. V., van Schaik, S. J., Spakman, W., Bijl, P. K., Sluijs, A., Langereis, C. G., and Brinkhuis, H., 2015, A Paleolatitude Calculator for Paleoclimate Studies: *PLoS One*, v. 10, no. 6, p. e0126946.
- Westerhold, T., Röhl, U., Donner, B., McCarren, H. K., and Zachos, J. C., 2011, A complete high-resolution Paleocene benthic stable isotope record for the central Pacific (ODP Site 1209): *Paleoceanography*, v. 26, no. 2.
- Westerhold, T., Röhl, U., Frederichs, T., Agnini, C., Raffi, I., Zachos, J. C., and Wilkens, R. H., 2017, Astronomical calibration of the Ypresian timescale: implications for seafloor spreading rates and the chaotic behavior of the solar system?: *Climate of the Past*, v. 13, no. 9, p. 1129-1152.
- Westerhold, T., Röhl, U., Raffi, I., Fornaciari, E., Monechi, S., Reale, V., Bowles, J., and Evans, H. F., 2008, Astronomical calibration of the Paleocene time: *Palaeogeography, Palaeoclimatology, Palaeoecology*, v. 257, no. 4, p. 377-403.
- Yu, J., and Elderfield, H., 2007, Benthic foraminiferal B/Ca ratios reflect deep water carbonate saturation state: *Earth and Planetary Science Letters*, v. 258, no. 1-2, p. 73-86.
- Yu, J., Thornalley, D. J. R., Rae, J. W. B., and McCave, N. I., 2013, Calibration and application of B/Ca, Cd/Ca, and $\delta^{11}\text{B}$ in *Neogloboquadrina pachyderma* (sinistral) to constrain CO₂ uptake in the subpolar North Atlantic during the last deglaciation: *Paleoceanography*, v. 28, no. 2, p. 237-252.
- Zachos, J., Pagani, M., Sloan, L., Thomas, E., and Billups, K., 2001, Trends, rhythms, and aberrations in global climate 65 Ma to present: *Science*, v. 292, no. 5517, p. 686-693.

- Zachos, J. C., Dickens, G. R., and Zeebe, R. E., 2008, An early Cenozoic perspective on greenhouse warming and carbon-cycle dynamics: *Nature*, v. 451, no. 7176, p. 279-283.
- Zachos, J. C., Kroon, D. C., Blum, P., and others, 2004, Proceedings of the Ocean Drilling Program. Vol. 208, Initial Reports. Early Cenozoic Extreme Climates: The Walvis Ridge Transect.
- Zachos, J. C., McCarren, H., Murphy, B., Röhl, U., and Westerhold, T., 2010, Tempo and scale of late Paleocene and early Eocene carbon isotope cycles: Implications for the origin of hyperthermals: *Earth and Planetary Science Letters*, v. 299, no. 1-2, p. 242-249.
- Zachos, J. C., Rohl, U., Schellenberg, S. A., Sluijs, A., Hodell, D. A., Kelly, D. C., Thomas, E., Nicolo, M., Raffi, I., Lourens, L. J., McCarren, H., and Kroon, D., 2005, Rapid acidification of the ocean during the Paleocene-Eocene thermal maximum: *Science*, v. 308, no. 5728, p. 1611-1615.
- Zachos, J. C., Schouten, S., Bohaty, S., Quattlebaum, T., Sluijs, A., Brinkhuis, H., Gibbs, S. J., and Bralower, T. J., 2006, Extreme warming of mid-latitude coastal ocean during the Paleocene-Eocene Thermal Maximum: Inferences from TEX86 and isotope data: *Geology*, v. 34, no. 9.
- Zachos, J. C., Wara, M. W., Bohaty, S., Delaney, M. L., Petrizzo, M. R., Brill, A., Bralower, T. J., and Premoli-Silva, I., 2003, A Transient Rise in Tropical Sea Surface Temperature During the Paleocene-Eocene Thermal Maximum: *Science*, v. 302.
- Zeebe, R. E., 2012, LOSCAR: Long-term Ocean-atmosphere-Sediment Carbon cycle Reservoir Model v2.0.4: *Geoscientific Model Development*, v. 5, no. 1, p. 149-166.
- Zeebe, R. E., 2013, What caused the long duration of the Paleocene-Eocene Thermal Maximum?: *Paleoceanography*, v. 28, no. 3, p. 440-452.
- Zeebe, R. E., Ridgwell, A., and Zachos, J. C., 2016, Anthropogenic carbon release rate unprecedented during the past 66 million years: *Nature Geoscience*, v. 9, no. 4, p. 325-329.
- Zeebe, R. E., Westerhold, T., Littler, K., and Zachos, J. C., 2017, Orbital forcing of the Paleocene and Eocene carbon cycle: *Paleoceanography*, v. 32, no. 5, p. 440-465.
- Zeebe, R. E., and Wolf-Gladrow, D., 2001, CO₂ in seawater: Equilibrium, Kinetics, Isotopes, Elsevier Science B.V., Elsevier Oceanography Series, 65.

Zeebe, R. E., and Zachos, J. C., 2013, Long-term legacy of massive carbon input to the Earth system: Anthropocene versus Eocene: *Philos Trans A Math Phys Eng Sci*, v. 371, no. 2001, p. 20120006.

Zeebe, R. E., Zachos, J. C., and Dickens, G. R., 2009, Carbon dioxide forcing alone insufficient to explain Palaeocene–Eocene Thermal Maximum warming: *Nature Geoscience*, v. 2, no. 8, p. 576-580.